PHYSICAL AND OPTOELECTRONIC PROPERTIES OF COPPER SILVER INDIUM DISELENIDE THIN FILMS

BY

ANGEL ROBERTO AQUINO GONZALEZ

DISSERTATION

Submitted in partial fulfillment of the requirements
for the degree of Doctor of Philosophy in Materials Science and Engineering
in the Graduate College of the
University of Illinois at Urbana-Champaign, 2012

Urbana, Illinois

Doctoral Committee:

Professor Angus A. Rockett, Chair and Director of Research
Professor John R. Abelson
Professor Emeritus Stephen G. Bishop
Assistant Professor Lane W. Martin

ABSTRACT

Increasing global energy consumption together with environmental concerns has led to much interest in alternative, cleaner sources of energy such as solar photovoltaic. Researchers in the solar cell community have been looking for ways to reduce costs while maintaining or increasing already high efficiencies. A fundamental understanding of the materials under consideration is essential to rapid development of new technologies. The I-III-VI_2 thin film alloys offer promising systems for achieving high efficiency solar cells at lower costs. In fact, by tailoring the chemistry of the compounds it is possible to change the bandgap of the material in order to collect sunlight more efficiently.

A promising alloy for tunable bandgap solar cells is the (Cu,Ag)(In,Ga)Se_2 system. The focus of my dissertation is to perform a comprehensive characterization of the structural and optoelectronic properties of $Cu_xAg_{1-x}InSe_2$ alloy thin films in order to gain a better understanding of the material. Detailed physical characterization was carried out in order to reveal differences in the structural properties of the alloy as a function of the Cu/(Cu+Ag) ratio. The identification and behavior of defect levels in the alloy was studied as a function of composition. From this, a band diagram schematic of the defect levels in the films is proposed, which could serve as a blueprint for improvements of the films properties through defect engineering.

The effects of alloying Ag with $CuInSe_2$ on the physical properties were shown. The addition of Ag appears to improve the structural quality of the films. This was seen by a reduction in the full-width-at-half-maximum of the luminescence peaks, a reduction in the number of optical transitions, and the appearance of free-to-bound transitions for

Ag-dominant films. An increase in the minority carrier lifetime of films with the addition of Ag also supports this conclusion. Furthermore, $AgInSe_2$ films showed less spatial and spectral variations than Cu-containing films in cathodoluminescence measurements, indicating less heterogeneity in the material. The results presented in this dissertation suggest that the $Cu_xAg_{1-x}InSe_2$ alloy is a suitable candidate for narrow bandgap solar cells. In spite of the observed beneficial effects of Ag, various challenges have been identified through this work. These include the existence of an ordered defect compound near the films surface for compositions of $x \leq 0.2$, the predilection of obtaining n-type films for $AgInSe_2$, and the presence of a continuum of defects into the bandgap of Ag-dominant films.

To my parents, wife, and kids…

A mis padres, esposa e hijos…

ACKNOWLEDGMENTS

This work has been possible due to the contributions of many colleagues, friends, and family members. I would like to begin by acknowledging my research advisor, Dr. Angus Rockett, whom I am deeply indebted to. His patience, understanding, and advice throughout my graduate studies have made of this journey a pleasant one. Dr. Rockett, thank you for taking an unpolished engineer and molding him into a scientist. In doing this you have achieved something close to miraculous!

My committee members have also been key to the development of this work. Professor Bishop, thank you for the long hours of Skype and phone conversations! I learned so much from you about luminescence techniques both from a scientific and historical point of view, something very few other people could have provided. Professor Abelson, thank you for meeting with me regularly to discuss my project and for helping me think about challenging questions. Your suggestions really helped present my data in much clearer ways. Professor Martin, your revisions to the manuscript as well as the questions posed were extremely valuable. I look forward to future collaborations with your respective groups.

Had I been given the choice of selecting individual group members, I could not have picked better people. Allen, Damon, Pam, Antonio, Dan, Zhen, Yiming, Zhengfeng, Tom, Andrew, and the rest of the gang: you have all been instrumental in my work. Allen Hall: thanks for your numerous suggestions…these were the seed that got this project started! Damon Hebert: thank you for teaching me about the various experimental techniques used throughout my work. Pamela Martin: your kindness and patience as an officemate are unmatched! I will cherish every memory I have shared

with the group. From the countless “I don’t belong here” and “It’s hopeless” conversations to the moments when we would goof around for 5 minutes during a busy day only to have Angus sneak up during that precise moment! Ahhh… nothing quite like the office of a graduate student.

The experimental part of this dissertation and subsequent data analysis would have been much more challenging had it not been for the excellent assistance received from the Materials Research Laboratory scientists. Vania Petrova, James Mabon, Scott MacLaren, Mauro Sardela, Changhui Lei, Doug Jeffers, Rick Haasch, Timothy Spila, Julio Soares, and Bharat Sankara: I was extremely fortunate to have worked by your side and am grateful for your many contributions to this work as well as my professional development.

Finally I would like to thank family. I cannot express in words how thankful I am to have such an incredible family: from hardworking grandparents, to the coolest aunts, uncles, and cousins, and an excellent brother! My parents, Angel and Norma, have molded me into the person I am today and there is no way I could ever thank them enough for their support and encouragement throughout the pursue of this degree. My wife, Jaskayahaira, has been here for me since the beginning of this journey and has both enjoyed and suffered the ups and downs of the process. Thank you my love for your daily support and for the wonderful blessing of children! My daughter Liliana and my son Yair, whom I refer to as "editors-in-chief" of this document, have provided a constant source of joy and happiness and put life’s struggles into perspective.

TABLE OF CONTENTS

CHAPTER 1: INTRODUCTION 1
1.1 Motivation 1
1.2 Thesis Statement 3
1.3 Thesis Summary 4
1.4 References 9
1.5 Figures 11

CHAPTER 2: BACKGROUND 13
2.1 $Cu_xAg_{1-x}InSe_2$ Alloy 13
2.2 Structural and Chemical Properties of $Cu_xAg_{1-x}InSe_2$ 14
2.3 Optical Properties, Shallow Defects, and Electronic Structure of $AgInSe_2$ 16
2.4 Electrical Properties and Deep Defects in $AgInSe_2$ 18
2.5 Deposition of $Cu_xAg_{1-x}InSe_2$ Thin Films 20
2.6 Devices 21
2.7 References 22
2.8 Figures 29

CHAPTER 3: EXPERIMENTAL METHODS 34
3.1 Introduction 34
3.2 Deposition of $Cu_xAg_{1-x}InSe_2$ Thin Films 34
3.3 In Situ Growth Monitoring 35
3.4 Structural Characterization Methods 36
3.5 Chemical Characterization Methods 38
3.6 Optical Characterization Methods 39
3.7 Electrical Characterization Methods 42
3.8 Additional Sample Preparation 42
3.9 References 43
3.10 Tables 44
3.11 Figures 45

CHAPTER 4: GROWTH AND PHYSICAL PROPERTIES OF $Cu_xAg_{1-x}InSe_2$ THIN FILMS 47
4.1 Introduction 47
4.2 Growth Modes 48
4.3 Composition 49
4.4 Structural Properties 49
4.5 Optical Band Gaps 53
4.6 Conclusions 55
4.7 References 56
4.8 Tables 59
4.9 Figures 60

CHAPTER 5: IDENTIFICATION OF RADIATIVE DEFECTS IN $Cu_xAg_{1-x}InSe_2$ THIN FILMS 72
5.1 Introduction 72
5.2 Results 72
5.3 Discussion 79
5.4 Conclusions 82
5.5 References 83
5.6 Tables 85
5.7 Figures 87

CHAPTER 6: MINORITY CARRIER LIFETIMES OF $Cu_xAg_{1-x}InSe_2$ THIN FILMS 92
6.1 Introduction 92
6.2 Results and Discussion 93
6.3 Conclusions 96
6.4 References 96
6.5 Tables 98
6.6 Figures 99

CHAPTER 7: SPATIAL DISTRIBUTION OF DEFECTS IN $Cu_xAg_{1-x}InSe_2$ THIN FILMS 103
7.1 Introduction 103
7.2 Results and Discussion 104
7.3 Conclusions 109
7.4 References 110
7.5 Figures 111

CHAPTER 8: $CuInSe_2$/CdS HETEROJUNCTION STABILITY 121
8.1 Introduction 121
8.2 Experimental 123
8.3 Results 124
8.4 Discussion 128
8.5 Conclusions 130
8.6 References 130
8.7 Figures 133

CHAPTER 9: CONCLUSIONS 138
9.1 Conclusions and Outlook 138
9.2 Future Research 141

APPENDIX A: SUPPLEMENTAL FIGURES 143
A.1 Scanning Electron Microscopy Images 143
A.2 Photoluminescence Spectra 145
A.3 Cathodoluminescence Spectra 151

CHAPTER 1

INTRODUCTION

1.1 Motivation

Thin films of a-Si, $Cu(In,Ga)Se_2$ and related I-III-VI_2 compounds, and CdTe have been of great interest to both the research and commercial solar cell communities because of their many advantageous properties over bulk crystalline technologies. Due to their high absorption coefficients (> 10^4 cm^{-1}) [1], only 1-2 μm of the material are needed to absorb the incoming radiation, as opposed to crystalline silicon where tens of microns are required to obtain similar results. This leads to a decrease in the amount of material needed for the thin film devices, which translates to lower costs due to lower materials utilization and processing time. The materials are ideal for deposition on flexible, lightweight substrates. Relatively good device efficiencies (> 14% [2-3]) have been achieved in complete modules by using polycrystalline material, and a group at Zentrum für Sonnenenergie- und Wasserstoff-Forschung in Germany has shown laboratory scale solar cell devices with efficiencies above 20% [4].

Historically, thin films have been fabricated into solar cell devices using only a single junction, just like crystalline silicon. There are several factors that limit the efficiency of a single junction device, as seen in Figure 1.1 [5]. Of particular significance are the losses due to incoming radiation with energy below or above the bandgap. The material will appear transparent to radiation with energy below the bandgap. Transparency accounts for approximately 20% losses for a 1.0 eV band gap [5]. Radiation with energy above the bandgap will be absorbed by the material, but all the energy in excess of the bandgap is lost due to thermalization of the carriers to the band

edges, accounting for over 29% in losses. In order to overcome these losses, devices with multiple junctions have been fabricated using III-V semiconductor alloys. This group of alloys (AlGaAs, InGaP, etc.) can be engineered to be lattice matched to currently available substrates (Ge) while still obtaining near-ideal bandgaps. Currently the highest efficiency solar cells (> 40% under concentration [6]) are fabricated using III-V multijunctions. However they are very expensive to produce due to complex growth methods needed to ensure lattice matching of all the layers. Furthermore, epitaxial layers are needed in order to maintain good device properties.

Ideally one would like to have the low cost and flexibility of thin film solar cells together with the high efficiency of III-V multijunction cells. One way of achieving this is by engineering thin film, multijunction devices. Instead of using III-V materials for the different junctions, alloys of I-III-VI_2 ($CuInSe_2$, $CuGaSe_2$, etc.) composition could be used instead. Figure 1.2 shows the AM1.5 solar spectrum with the bandgaps of different I-III-VI_2 compounds overlaid. From this figure it is evident that by tailoring the chemistry of the compounds one could change the bandgap of the material. The advantages that I-III-VI_2 compounds have over III-V compounds are that they do not need to be lattice matched because they are typically grown as polycrystals and they require much less material. This idea has the potential of yielding high efficiency devices at relatively lower costs.

One of the problems with this concept is that to date, the efficiency of the high bandgap partner for a I-III-VI_2 multijunction device has remained relatively low. The Ag, Ga, and S species yield the largest bandgaps, but devices with these atomic species have very low efficiencies for reasons that are not fully understood. This is due in part to

the complexity of the system and the lack of studies on these higher band gap I-III-VI_2 compounds as compared to other crystalline technologies. One of these interesting alloy systems is $Cu_xAg_{1-x}InSe_2$, which has a maximum bandgap of around 1.24 eV [7-8]. Adding Ag to $CuInSe_2$ increases the bandgap closer to the ideal value for single junction cells and therefore increases the open circuit voltage (V_{oc}), which should lead to higher efficiencies. The Ag compound also has a lower melting temperature than $CuInSe_2$ [9], which means that you could deposit these layers at lower temperatures and still achieve optimal structural/electrical properties. However, due to the lack of work on the $Cu_xAg_{1-x}InSe_2$ compound, very little is known about the behavior of defects as a function of composition. Furthermore, no studies have looked into the effects of grain boundaries on the films electrical and optical properties.

1.2 Thesis Statement

I have chosen to study the $Cu_xAg_{1-x}InSe_2$ alloy and the effects that compositional changes have on its optical and electrical properties. The goal of this body of work is to provide a clear picture of the defects present in $Cu_xAg_{1-x}InSe_2$ polycrystalline thin films as a function of composition. The key questions that are answered by this work are the following: What types of defects are present in the films, what are the energy levels of the electrically active defects, what is their spatial distribution, and how do these change with alloy composition? The effects of sodium and substrate on grain size and film texture are also discussed. A detailed understanding of these alloys and their properties can potentially contribute a new and important alloy to the materials usable in polycrystalline thin-film solar cells. It will provide engineers and device manufacturers with a basis for controlling defects in their films by controlling growth parameters.

Furthermore, it will advance our knowledge of wider bandgap materials for use in top junctions, bringing thin film multijunction devices closer to reality.

Another goal of this work is to study the behavior of grain boundaries in $Cu_xAg_{1-x}InSe_2$ thin films as a function of composition. A puzzling phenomenon in I-III-VI_2 thin film solar cells is that grain boundaries do not appear to adversely affect device performance. This has been a topic of much debate among the scientific community, leading to various theories as to why grain boundaries are not detrimental to thin films [10–15]. By studying this specific alloy, I will be able to tell if the group I cation plays a role in the behavior of grain boundaries, which will give the scientific community insight into the behavior of similar I-III-VI_2 compounds.

1.3 Thesis Summary

Background information and a current literature review on the $Cu_xAg_{1-x}InSe_2$ system is provided for the reader in **Chapter 2**. Structural, electrical, and optical properties of the system are discussed as well as film growth and device fabrication. The experimental methods used in this work are described in detail in **Chapter 3**. The deposition methods and equipment used to deposit the films of this study are described in detail in the first section of this chapter. This is followed by a discussion of the analysis techniques used to characterize the films, including structural, chemical, electrical, and optical properties. Detailed descriptions of the equipment and analysis conditions are given for each set of experiments.

In **Chapter 4**, the $Cu_xAg_{1-x}InSe_2$ thin films used in this work are described in detail. Films with thicknesses of 700 nm and at intervals of x = 0.2, where x =

Cu/(Cu+Ag), were deposited on various substrates, including bare soda-lime glass substrates (SLG) and Mo-coated SLG substrates. Determination of the composition of the films is discussed in section 4.3. All films were group-I deficient with Se concentrations close to 50 at.%. Structural properties such as crystallinity, phase identification, lattice parameters, faceting, and grain size are presented in section 4.4. All films showed preferred (112) orientation with the exception of films with $x \geq 0.8$, which showed preferred (220)/(204) orientation. The lattice parameters also deviated from Vegard's law. An ordered defect compound consistent with $AgIn_5Se_8$ was identified near the surface of films with $x \leq 0.2$. The effects of sodium on grain size are also studied as a function of film composition. This involved the deposition of $Cu_xAg_{1-x}InSe_2$ films on substrates with Na (bare SLG) and without Na (25 nm thermal oxide on Si). No beneficial effects to grain size were observed from the presence of Na in films with $x \leq 0.6$. However, for $x \geq 0.8$, films with Na showed a doubling of grain size relative to those without Na.

Chapter 5 describes the defect levels in polycrystalline thin films of $Cu_xAg_{1-x}InSe_2$ studied via photoluminescence spectroscopy. Optical transitions were identified for the films and their behavior was studied as a function of power, temperature, and composition. Donor-acceptor pair transitions were observed as well as free-to-bound transitions. Two donor levels (20-30 meV and 60 meV) and three acceptor levels (20-35 meV, 70-110 meV, and 170-190 meV) were identified in the films. Significant subgap emission was observed between the near band edge and ~750 meV photon energies in all samples. Exponentially decaying tails were observed to extend deep into the band gap (beyond the detectors sensitivity) for Ag-dominant compounds ($x \leq 0.4$). A continuum of

defects this deep into the gap could hinder carrier collection, significantly reducing the efficiency of a solar cell fabricated from $AgInSe_2$ or Ag-rich $Cu_xAg_{1-x}InSe_2$ absorber layers.

Minority carrier lifetimes in $Cu_xAg_{1-x}InSe_2$ thin films were studied via time-resolved photoluminescence measurements in **Chapter 6**. Samples on bare glass exhibited the lowest lifetimes (~ 200 ps), indicating a lack of order in the films and smaller grain sizes. Lifetimes for films on Mo-coated glass showed significant improvement, with some films showing increases of up to 1 order of magnitude. These films also exhibited lifetimes comparable or higher to $CuInSe_2$ for compositions up to $x \geq 0.2$. This offers a remarkable range in the alloy space to work with, enabling the use of Ag-based alloys for both single junction and tandem junction photovoltaic devices.

The spatial distribution of these defects is described in **Chapter 7**. Cryogenic cathodoluminescence experiments were carried out in both spectral CL mode and imaging mode in order to map the position of the defects at the micro/nano-scale. These emissions were studied as a function of sample composition and relative position to grain boundaries. The $AgInSe_2$ sample showed more uniform luminescence both spatially and spectrally than Cu-containing samples. $AgInSe_2$ is also less affected by reduced emission from surface features, presumably due to less surface recombination. Cu-containing samples exhibit enhanced luminescence from grain boundaries or inter-grain areas, indicative of compositional or electrically-active defect fluctuations. This was more apparent from grain to grain in the $Cu_{0.6}Ag_{0.4}InSe_2$, as it showed the most variation among the samples in emission from one grain to another. The $CuInSe_2$ sample showed

the most variation in emission from grain to grain boundary, indicating possible chemical fluctuations at the grain boundaries.

In **Chapter 8**, the stability of the $CuInSe_2$/CdS heterojunction is studied. The stability of this junction is important when considering it for use in multijunction devices, due to the thermal conditions during deposition of subsequent layers. In this chapter annealing experiments are performed on both polycrystalline and epitaxial $CuInSe_2$/CdS layers. The resulting films were then studied using SIMS depth profiling in order to study the movement of atomic species across interfaces. Results show that the heterojunction is stable for temperatures under 400 °C. Past this point, significant diffusion of Cu, Cd, and In were observed. However, no time dependence was observed in the 400 and 500°C anneals indicating that a reaction had occurred forming a compound that was in thermodynamic equilibrium with the remaining CIS. This compound was identified via x-ray diffraction as $Cu_{0.75}Cd_{0.5}In_{0.75}Se_2$.

Finally, a summary of the work presented in this thesis and concluding remarks are presented in **Chapter 9**. This body of work has shown that the $Cu_xAg_{1-x}InSe_2$ alloy is a suitable candidate for higher bandgap solar cells. Alloying the I-III-VI_2 family with Ag increases the structural order of the material, which leads to less electrically active defects in the material, as seen by the PL and CL work. Future work is also outlined in order to continue improving the absorber layer quality of Ag-dominant films.

The results of my research are also presented in the following publications:

Chapter 4: **A. Aquino**, S. Little, V. Ranjan, R.W. Collins, S. Marsillac, and A. Rockett, "Physical Characterization of $Cu_xAg_{1-x}InSe_2$ Thin Films", in preparation, and in T.

Begou, S. Little, **A. Aquino**, V. Ranjan, A. Rockett, R. Collins, and S. Marsillac, "In Situ and Ex Situ Characterization of (Ag,Cu)$InSe_2$ Thin Films", Conference Record of the 37th IEEE PVSC, 2011.

Chapter 5: **A. Aquino**, S. Little, S. Marsillac, R. Collins, and A. Rockett, "Photoluminescence of $Cu_xAg_{1-x}InSe_2$ Thin Films", in preparation, and in **A. Aquino**, S. Little, S. Marsillac, R. Collins, and A. Rockett, "Identification of Defect Levels in $Cu_xAg_{1-x}InSe_2$ Thin Films via Photoluminescence", Conference Record of the 37th IEEE PVSC, 2011.

Chapter 6: **A. Aquino**, D. Kuciauskas, S. Little, S. Marsillac, R. Collins, P. Peña Martin, and A. Rockett, "Minority Carrier Lifetimes in $Cu_xAg_{1-x}InSe_2$ Thin Films", in preparation.

Chapter 7: **A. Aquino**, A. Rockett, S. Little, and S. Marsillac, "Cryogenic Cathodoluminescence from $Cu_xAg_{1-x}InSe_2$ Thin Films", Conference Record of the 35th IEEE PVSC, p. 3386-90, 2010.

Chapter 8: **A. Aquino** and A. Rockett, "Chemical Reactions at CdS heterojunctions with $CuInSe_2$", in press.

In addition, a number of publications not included in this dissertation were published as a result of other projects I have worked on throughout my degree. These are listed below:

1. Hepp, J. McNatt, J. Dickman, M. Jin, K. Banger, C. Kelley, **A. Aquino**, and A. Rockett, "Aerosol-Assisted Chemical Vapor Deposited Thin Films for Space

Photovoltaics", Fourth International Energy Conversion Engineering Conference (IECEC), 2006.

2. B. Johnson, B. Riley, S. Sundaram, J. Crum, C. Henager, Y. Zhang, V. Shutthanandan, C. Seifert, R. van Ginhoven, C. Chamberlin, A. Rockett, D. Hebert, and **A. Aquino**, "Synthesis and Characterization of Bulk, Vitreous Cadmium Germanium Arsenide", J Am Ceram Soc, 2009, 92, 6, 1236-1243.
3. D. Hebert, A. Hall, **A. Aquino**, A. Rockett, R. Haasch, B. Johnson, and B. Riley, "Kelvin Probe Force Microscopy of Metal Contacts on Amorphous Cadmium Germanium Arsenide", in preparation.
4. J. Chen, J. Li, C. Thornberry, M. Sestak, R. Collins, J. Walker, S. Marsillac, **A. Aquino**, and A. Rockett, "Through-The-Glass Spectroscopic Ellipsometry of CdTe Solar Cells", Conference Record of the 34th IEEE PVSC, p. 1748-53, 2009.
5. S. Leblebici, **A. Aquino**, A. Rockett, "Fabrication of a thin film transistor on epitaxial $CuInSe_2$", Intel Undergraduate Research Exposition, University of Illinois, 2008.

1.4 References

[1] N. Kavcar, "Study of the sub-bandgap absorption and the optical transitions in CuInSe2 polycrystalline thin films," *Solar Energy Materials and Solar Cells*, vol. 52, no. 1-2, pp. 183-195, Mar. 1998.

[2] C. Ferekides and J. Britt, "CdTe solar cells with efficiencies over 15%," *Solar Energy Materials and Solar Cells*, vol. 35, pp. 255-262, Sep. 1994.

[3] K. Ramanathan, G. Teeter, J. Keane, and R. Noufi, "Properties of high-efficiency CuInGaSe thin film solar cells," *Thin Solid Films*, vol. 480-481, pp. 499-502, Jun. 2005.

[4] P. Jackson, D. Hariskos, and E. Lotter, "New world record efficiency for Cu (In, Ga) Se2 thin-film solar cells beyond 20%," *Progress in Photovoltaics: Research and Applications*, pp. 3-6, 2011.

[5] A. L. Fahrenbruch and R. H. Bube, *Fundamentals of solar cells: photovoltaic solar energy conversion*. New York: Academic Press, 1983, p. 559.

[6] M. A. Green, K. Emery, Y. Hishikawa, and W. Warta, "Solar cell efficiency tables (version 37)," *Progress in Photovoltaics: Research and Applications*, vol. 19, no. 1, pp. 84-92, Jan. 2011.

[7] S. Ozaki and S. Adachi, "Optical properties and electronic band structure of AgInSe2," *Physica Status Solidi (a)*, vol. 203, no. 11, pp. 2919-2923, Sep. 2006.

[8] J. Shay, B. Tell, H. Kasper, and L. Schiavone, "Electronic Structure of AgInSe2 and CuInSe2," *Physical Review B*, vol. 7, no. 10, pp. 4485–4490, 1973.

[9] J. L. Shay and J. H. Wernick, *Ternary chalcopyrite semiconductors: growth, electronic properties, and applications*. Pergamon Press Oxford, 1975.

[10] C. Persson and A. Zunger, "Anomalous Grain Boundary Physics in Polycrystalline CuInSe2: The Existence of a Hole Barrier," *Physical Review Letters*, vol. 91, no. 26, pp. 1-4, Dec. 2003.

[11] M. J. Hetzer, Y. M. Strzhemechny, M. Gao, M. a. Contreras, a. Zunger, and L. J. Brillson, "Direct observation of copper depletion and potential changes at copper indium gallium diselenide grain boundaries," *Applied Physics Letters*, vol. 86, no. 16, p. 162105, 2005.

[12] Y. Yan, C. S. Jiang, X. Z. Wu, R. Noufi, S.-H. Wei, and M. M. Al-Jassim, "Grain-boundary physics in polycrystalline photovoltaic materials," *2008 33rd IEEE Photovolatic Specialists Conference*, no. May, pp. 1-4, May 2008.

[13] D. Azulay, O. Millo, I. Balberg, H. Schock, I. Visolyfisher, and D. Cahen, "Current routes in polycrystalline CuInSe2 and Cu(In,Ga)Se2 films," *Solar Energy Materials and Solar Cells*, vol. 91, no. 1, pp. 85-90, Jan. 2007.

[14] I. Visoly-Fisher, S. R. Cohen, K. Gartsman, a. Ruzin, and D. Cahen, "Understanding the Beneficial Role of Grain Boundaries in Polycrystalline Solar Cells from Single-Grain-Boundary Scanning Probe Microscopy," *Advanced Functional Materials*, vol. 16, no. 5, pp. 649-660, Mar. 2006.

[15] L. L. Kazmerski, "The effects of grain boundary and interface recombination on the performance of thin-film solar cells," *Solid-State Electronics*, vol. 21, no. 11-12, pp. 1545–1550, 1978.

1.5 Figures

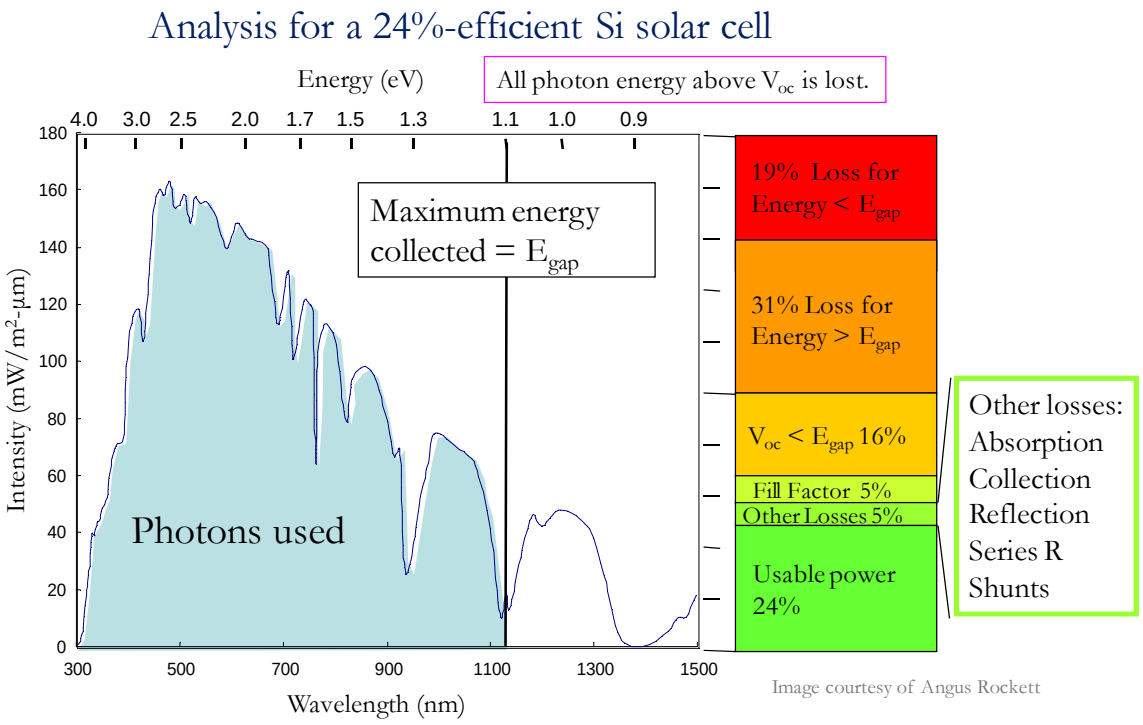

Figure 1.1. Analysis of losses for a 24% efficient silicon solar cell.

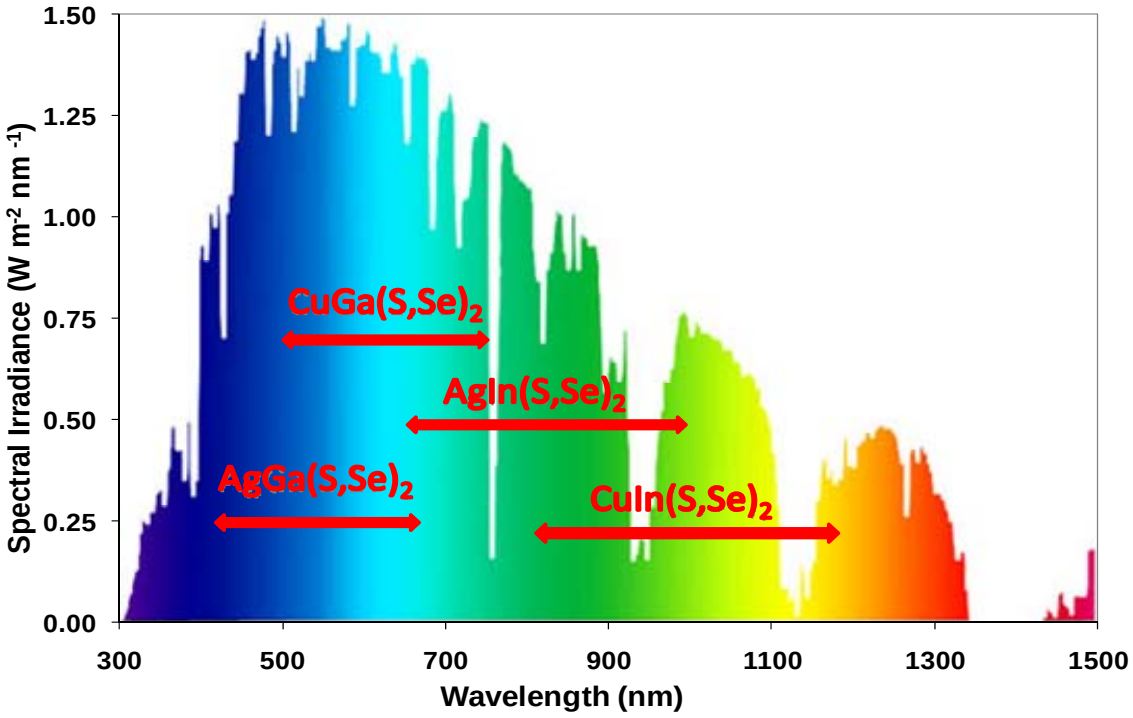

Figure 1.2. AM 1.5 solar spectrum with band gaps of I-III-VI_2 semiconductors overlaid. Notice how the band gaps of these materials cover almost the entire solar spectrum received on the surface of the earth, making them ideal candidates for thin-film multijunction solar cells.

CHAPTER 2

BACKGROUND

2.1 $Cu_xAg_{1-x}InSe_2$ Alloy

The highest efficiency achieved by any polycrystalline thin film solar cell was a $CuIn_xGa_{1-x}Se_2$ (CIGS) device produced by Zentrum fuer Sonnenenergie- und Wasserstoff-Forschung, Baden-Wuerttemberg (ZSW) in Germany (20.3% [1]) in 2010. By optimizing the ratio of the group III atomic species (In and Ga) they were able to obtain higher efficiencies than previously achieved using only the ternary constituents $CuInSe_2$ (CIS) or $CuGaSe_2$ (CGS). By taking a similar approach, it seems possible that by optimizing the group I constituents (Cu and Ag) we could further improve the device performance of these chalcopyrite thin film structures. The $Cu_xAg_{1-x}InSe_2$ (CAIS) alloy appears to be an attractive system to study because the $AgInSe_2$ (AIS) component has a higher optical bandgap and a lower melting temperature than the CIS compound. This could lead to high quality material at lower growth temperatures and therefore could be possible on flexible polymer substrates.

Of the two compounds that make up the $Cu_xAg_{1-x}InSe_2$ alloy, CIS has been the most studied one [2–4]. In fact, it has been one of the most studied thin film materials of the last decade together with a-Si and CdTe. Its bandgap is around 1 eV [2], which is very close to that of crystalline Si. However, unlike Si, CIS has a direct bandgap and consequently a very high absorption coefficient [2]. The material can be grown either n-type or p-type, depending on the stoichiometry, growth, and subsequent annealing conditions [4]. In general, there is a good understanding of the structural, optical, and electrical properties of the material [4]. However to this day there is an ongoing debate

about many aspects of CIS and how they affect device operation. For example, the impact of grain boundaries on thin film device performance is widely debated [5–11]. The $AgInSe_2$ component of the alloy has been studied far less that its counterpart. It was first examined by Hahn *et al.* [12] in 1954. Since his preparation of $AgInSe_2$, there have been over 60 publications that deal with the compound and its properties. The following sections give a summary of these properties.

2.2 Structural and Chemical Properties of $Cu_xAg_{1-x}InSe_2$

$Cu_xAg_{1-x}InSe_2$ crystallizes in the chalcopyrite structure belonging to the tetragonal crystal system [2]. This structure is illustrated in Figure 2.1. One of the main differences between the zinc-blende structure and the chalcopyrite structure is in the arrangement of the cations, which alternate along the [001] direction so that a cation superlattice is obtained. This leads to the near doubling of the unit cell ($c \sim 2a$) in $AgInSe_2$ [13]. The different cation electronegativities lead to the tetragonal distortion, with c typically smaller than $2a$ and a slight displacement of the anion (Se) towards one of the cations. This structural difference is what leads to a lot of the interesting electronic properties of the I-III-VI_2 compounds [14].

The structural parameters of both $CuInSe_2$ and $AgInSe_2$ have been extensively studied by many groups [13, 15–19]. $CuInSe_2$ has a lattice constant of 5.876 Å. As Ag is added, the lattice constant increases linearly (following Vegard's Law) until reaching a value of 6.106 Å for $AgInSe_2$ [20]. $CuInSe_2$ has a c/a ratio slightly larger than 2 [2, 21-22], however as the Ag content increases, the tetragonal distortion changes, leading to smaller c/a values [23]. The crystal field splitting, due to the tetragonal distortion along

c, has also been studied. Values of -0.13 eV and 6 meV have been obtained by Ramesh [24] and Madelung [25], respectively for $AgInSe_2$ and $CuInSe_2$. From these, negative deformation potentials of -0.753 eV and -0.96 eV were obtained [15, 24].

The texturing or preferred orientation of the films is also an important parameter. Since the junction in these devices is a heterojunction with CdS, the surface faceting plays an important role in determining the nature of the junction, and hence device performance. High efficiency CIGS device layers are typically grown to achieve a (220)/(204) preferred orientation [26]. However, work by Liao and Rockett [27-28] has shown that growth of $CuInSe_2$ usually leads to films with preferred (112) faceting. The same has been found true for $AgInSe_2$ films [24, 29–33]. In $CuInSe_2$ films, a Cu deficiency was observed at the surface [34]. Upon subsequent CdS deposition, Cd was seen incorporated into the top surface, suggesting Cd-doping due to the replacement of the Cu vacancies by Cd [35]. Similar work has not been carried out on $AgInSe_2$ films, so the surface effects for this system are not well understood.

Phase relations of the Ag – In – Se system have been studied before [16, 36]. $AgInSe_2$ forms at the 50 mol. % in the Ag_2Se – In_2Se_3 pseudobinary system, as seen in area 12 of Figure 2.2 [36]. It undergoes a polymorphous transition (chalcopyrite to sphalerite) at 968K and has a melting temperature of 1060 K. This lower melting temperature, as compared to $CuInSe_2$ and $CuGaSe_2$, is part of what makes it an attractive system from a growth and defect perspective. Films have typically been grown group I deficient (Ag poor), similar to $CuInSe_2$ growth. However, upon significant deviation from stoichiometry, secondary phase formation (Ag_2Se and In_2Se_3) occurs. It is

important to avoid secondary phase formation in our films in order to properly characterize the chalcopyrite $AgInSe_2$ phase, which is the subject of study in this work.

2.3 Optical Properties, Shallow Defects, and Electronic Structure of $AgInSe_2$

There are less than two dozen publications that look into the optical properties of $AgInSe_2$. Koitabashi *et al*. [37] provide a good review of optical property studies of $AgInSe_2$. Techniques applied have included optical absorption [33, 38–41], photoluminescence (PL) [20, 37-38, 40, 42–45], photoconductivity [24, 46], and spectroscopic ellipsometry [41, 47]. These studies have shown that the compound has a direct optical bandgap that ranges from 1.21 eV to 1.25 eV at room-temperature. Work by Shay *et al*. [44] has also shown an anomalous behavior of the bandgap as a function of temperature. Shay did not find a change in the bandgap of the compound in the range of 77 K – 300 K. Ozaki and Adachi [48] reported a positive temperature coefficient dE_g/dT for $T < 125$ K, and a negative coefficient dE_g/dT for $T > 125$ K. Just like $CuInSe_2$, $AgInSe_2$ has a very high optical absorption coefficient above the band edge region ($> 10^4$, [33, 49]).

The study of the optical properties has also led to the determination of the electronic band structure of the material. Electro-reflectance experiments [44] have revealed a three-fold optical structure near the band edge. This has been attributed [33, 44] to the crystal-field and spin-orbit splitting of the valence band, yielding values at 1.25 eV (fundamental absorption edge), 1.35 eV, and 1.60 eV (spin-orbit split bands). In compound semiconductors the conduction band minimum is mostly made up of the cation *s*-orbitals while the valence band maximum is composed of mostly anion *p*-orbitals

[50]. In I-III-VI_2 compounds it is usually the In or Ga *s*-orbitals that contribute the most to the conduction band minimum while the Se 4*p*-orbitals contribute the most towards the valence band maximum. However, the noble metals (Cu and Ag) introduce *d*-orbitals which have an effect on the position of the valence band maximum. These *d*-levels affect not only the optical bandgap but also the separation of the spin-orbit split valence bands. It is very important to understand the contributions of the Cu and Ag *d*-levels to the electronic structure of the material when trying to make sense of the optical and electrical properties of $Cu_xAg_{1-x}InSe_2$ alloy thin films, as is the case in this work.

Optical transitions have also been studied in these materials. Shay *et al.* [44] were able to grow high quality $AgInSe_2$ single crystals and observe excitonic emissions from them. Al-Kotb *et al.* [42] were able to identify two donor levels 27 meV and 80 meV from the conduction band which they attributed to V_{Se} and In_{Ag} defects, respectively. They also identified two acceptor levels at 50 meV and 24 meV away from the top of the valence band, which they assigned to V_{In} and V_{Ag} respectively. They observed PL peaks at 1.118 eV and 1.178 eV for n-type samples, and at 1.178 eV and 1.213 eV for p-type samples. Ozaki *et al.* [38] identified two peaks via PL at 1.18 eV and 1.20 eV which they assigned to donor-acceptor pair (DAP) transitions caused by acceptor states 10 meV and 27 meV from the top of the valence band. Yoshino *et al.* [40] found DAP transitions at 0.9 eV and attributed them to Ag_i and V_{In} defects. Kishigui *et al.* [45] found peaks at 1.19 eV and 1.16 eV which they also attributed to DAP transitions due to donors at 25 meV and 50 meV from the conduction band edge. Most authors concur on the 1.18 eV and 1.20 eV peak positions and on the 27 meV energy level for one of the defects. The position of the other energy level varies widely (50-80 meV) from experiment to

experiment and so does the assignment of point defects. A summary of these shallow defect levels is illustrated in Figure 2.3.

The works mentioned above have only studied AIS. The study of $Cu_xAg_{1-x}InSe_2$ alloys has been much more limited. Bacewicz [51] and Ciszek [20, 52] have looked at some optical and electrical properties of these crystals. Their work is the only study on the optoelectronic properties of *bulk* $Cu_xAg_{1-x}InSe_2$ alloy crystals. They were able to identify peaks and their associated defect levels by using PL and photoconductivity measurements. However, to this day there is no detailed systematic study on the optical properties of $Cu_xAg_{1-x}InSe_2$ *thin-films* as a function of composition. One of the objectives of this work is to perform a comprehensive and ordered study of the optical properties of $Cu_xAg_{1-x}InSe_2$ *thin-films*, which are better suited for fabrication into low-cost solar cell devices.

2.4 Electrical Properties and Deep Defects in $AgInSe_2$

Electrical characterization techniques have been applied to $AgInSe_2$ samples in order to determine the electrical properties of the films such as carrier concentration, mobility, resistivity, and carrier type. Abdel-Hady and Salem [53] give a summary of some of the electrical properties of the compounds. Temperature-dependent Hall Effect has been the preferred technique, because of the vast amount of information it offers. However, other methods such as photo-capacitance/conductivity measurements, capacitance-voltage profiling, and deep-level transient spectroscopy (DLTS) have also been carried out. Some of these techniques can offer additional information, such as the

activation energy for conduction (temperature dependent Hall Effect), information on the junction characteristics (C-V profiling), and the position of deep levels (DLTS).

$AgInSe_2$ has been grown with both p-type and n-type conductivity [53] by varying growth conditions. However, n-type films have been much easier to obtain. Current high efficiency $CuIn_xGa_{1-x}Se_2$ devices use an n-type CdS heterojunction partner, so obtaining p-type layers is desired. One method used to obtain p-type films was to perform a post-deposition anneal under Se pressure [40]. Ge-doping has also been used in order to increase the carrier concentration of the films [54]. In general, carrier concentrations have ranged from 10^{12} cm^{-3} to 10^{18} cm^{-3} [53]. Mobilities have varied from 5 to 300 $cm^2V^{-1}s^{-1}$ [53]. Defect levels have also been determined from these techniques. Joseph and Menon [49] observed activation energies from 76 meV to 330 meV for levels they attributed to Se interstitials (80-100 meV) and In interstitials (200 meV). They also observed an intrinsic level at 700 meV. Abdel-Hady and Salem measured activation energies for conduction around 200 meV [53]. Shafarman et al. [55] also measured levels between 150 meV and 200 meV using transient photocapacitance techniques in $Cu_xAg_{1-x}In_yGa_{1-y}Se_2$. They observed an additional defect level at 0.8 eV in all their films.

This short review of electrical properties of $(Cu,Ag)InSe_2$ films demonstrates the wide range of properties and defects that can be attained in the I-III-VI_2 system. Growth conditions and post-processing parameters have a profound effect on these properties. Some of these growth methods are discussed in the next section.

2.5 Deposition of $Cu_xAg_{1-x}InSe_2$ Thin Films

(Cu,Ag)$InSe_2$ can be made by a variety of processing methods including growth from the liquid phase, screen printing, electrodeposition, spray pyrolysis, sputtering, multi-source evaporation, and chemical vapor deposition, among others [2]. However, for solar power generation applications, the most promising use of I-III-VI_2 compounds is as thin films. The most popular techniques for thin film deposition of these materials have been multi-source evaporation and non-vacuum techniques such as printing. Co-evaporation offers the highest efficiency devices of any of the technologies (> 18% [56]). Non-vacuum techniques offer low cost when compared to vacuum deposition systems, however their efficiencies are still lagging behind (~ 10% [57–60]).

During multi-source evaporation a Mo-coated soda-lime glass substrate is typically held at 550 °C. High purity (5N) elements (Cu, Ag, In, Ga, Se) are placed in effusion cells and evaporated. The flux of the group I and III elements determine the growth rate and composition of the films, while an excess of Se is supplied. Se in excess of the required amount for stoichiometry will desorb from the film surface. High-efficiency films grown by NREL are deposited using a three-stage process where In and Se are deposited during the first stage. This is followed by Cu and Se deposition during the second stage and finally In and Se deposition for the third stage. A temperature and flux profile of NREL's process is seen in Figure 2.4 [61]. One disadvantage of this process is the difficulty to implement it in continuous manufacturing settings, which is desirable for low cost production of devices.

The films analyzed in this work were deposited using a hybrid technique that includes sputtering and evaporation. Sputtering is particularly scalable and is suitable for high-volume manufacturing. The specifics of this process are described in more detail in Chapter 3. Thin film samples are grown under different conditions than bulk samples. The impinging species is usually in the form of a vapor phase arriving at a substrate material, as opposed to a liquid phase for bulk samples. These differences can lead to changes in the types of electrically-active defects present in the samples, so it is important to keep in mind the type of deposition method used when analyzing and interpreting data.

2.6 Devices

$Cu_xAg_{1-x}InSe_2$ devices are typically deposited on Mo-coated soda-lime glass substrates. P-type conductivity is desired for the absorber layer because of the heterojunction partner availability and the longer minority carrier diffusion length of electrons. Once the absorber layer is deposited, device fabrication is typically followed by chemical bath deposition of the heterojunction partner. N-type CdS has been the most widely used partner, but Cd-free alternatives such as ZnS have also been considered. A thin ZnO window layer is deposited (~ 50 nm undoped and 200 nm Al-doped) on top of the CdS, followed by the transparent conducting oxide (Indium Tin Oxide), metallization (Al), and anti-reflective coatings. This device structure is illustrated in Figure 2.5. Studies on $CuInSe_2$ have shown that the device is limited by recombination in the space-charge region rather than interface recombination [62], meaning that the properties of the absorber layer are critically important. However, the limiting mechanism in $AgInSe_2$ solar cells has not been studied.

$AgInSe_2$-based solar cell devices have been fabricated by only a handful of groups [63–68]. P.Paul Ramesh was the first to fabricate a AgInSe2-$Cd_xZn_{1-x}S$ based device, achieving conversion efficiencies of over 7.5% [65]. To this date, this is the only report of a pure $AgInSe_2$ device. Other groups have fabricated devices that in addition contain either Cu (as a substitute for Ag) or Ga (as a substitute for In). Among these, Nakada's group has produced the highest efficiency (9.3%, [64]) I-III-VI_2 cell that has a bandgap above 1.65 eV. Their cell had a $AgIn_xGa_{1-x}Se_2$ absorber layer with $x = 0.2$. Shafarman and his group have added Cu to this type of cell and have achieved efficiencies as high as 13% with a bandgap of 1.60 eV [69]. Their device has yielded the highest efficiency of any high-bandgap device produced to date. A fundamental understanding of the effects of Ag and Cu on the optoelectronic properties of the films is critical to the continued improvement of efficiencies in wide-bandgap I-III-VI_2 thin film solar cells. I believe that this work will get us closer to that goal.

2.7 References

[1] P. Jackson, D. Hariskos, and E. Lotter, "New world record efficiency for Cu(In, Ga)Se_2 thin-film solar cells beyond 20%," *Progress in Photovoltaics: Research and Applications*, pp. 3-6, 2011.

[2] A. Rockett and R. W. Birkmire, "$CuInSe_2$ for photovoltaic applications," *Journal of Applied Physics*, vol. 70, no. 7, p. R81, 1991.

[3] R. W. Birkmire and E. Eser, "Polycrystalline Thin Film Solar Cells:Present Status and Future Potential," *Annual Review of Materials Science*, vol. 27, no. 1, pp. 625-653, Aug. 1997.

[4] B. Stanbery, "Copper Indium Selenides and Related Materials for Photovoltaic Devices," *Critical Reviews in Solid State and Materials Sciences*, vol. 27, no. 2, pp. 73-117, Apr. 2002.

[5] C. Persson and A. Zunger, "Anomalous Grain Boundary Physics in Polycrystalline $CuInSe_2$: The Existence of a Hole Barrier," *Physical Review Letters*, vol. 91, no. 26, pp. 1-4, Dec. 2003.

[6] M. J. Hetzer, Y. M. Strzhemechny, M. Gao, M. a. Contreras, a. Zunger, and L. J. Brillson, "Direct observation of copper depletion and potential changes at copper indium gallium diselenide grain boundaries," *Applied Physics Letters*, vol. 86, no. 16, p. 162105, 2005.

[7] Y. Yan, C. S. Jiang, X. Z. Wu, R. Noufi, S.-H. Wei, and M. M. Al-Jassim, "Grain-boundary physics in polycrystalline photovoltaic materials," *2008 33rd IEEE Photovolatic Specialists Conference*, no. May, pp. 1-4, May 2008.

[8] Y. Yan, C.-S. Jiang, R. Noufi, S.-H. Wei, H. Moutinho, and M. Al-Jassim, "Electrically Benign Behavior of Grain Boundaries in Polycrystalline $CuInSe_2$ Films," *Physical Review Letters*, vol. 99, no. 23, pp. 2-5, Dec. 2007.

[9] D. Azulay, O. Millo, I. Balberg, H. Schock, I. Visolyfisher, and D. Cahen, "Current routes in polycrystalline $CuInSe_2$ and $Cu(In,Ga)Se_2$ films," *Solar Energy Materials and Solar Cells*, vol. 91, no. 1, pp. 85-90, Jan. 2007.

[10] I. Visoly-Fisher, S. R. Cohen, K. Gartsman, A. Ruzin, and D. Cahen, "Understanding the Beneficial Role of Grain Boundaries in Polycrystalline Solar Cells from Single-Grain-Boundary Scanning Probe Microscopy," *Advanced Functional Materials*, vol. 16, no. 5, pp. 649-660, Mar. 2006.

[11] L. L. Kazmerski, "The effects of grain boundary and interface recombination on the performance of thin-film solar cells," *Solid-State Electronics*, vol. 21, no. 11-12, pp. 1545–1550, 1978.

[12] H. Hahn, G. Frank, W. Klingler, and A. Meyer, "Uber einige ternare Chalkogenide mit Chalkopyritstruktur," *Anorg. Allg. Chem*, vol. 271, pp. 153-170, 1953.

[13] A. Chahed, O. Benhelal, H. Rozale, S. Laksari, and N. Abbouni, "Structural and electronic properties of chalcopyrite semiconductors $AgXY_2$ (X = In, Ga; Y = S, Se, Te) under pressure," *Physica Status Solidi (B)*, vol. 244, no. 2, pp. 629-634, Feb. 2007.

[14] R. Asokamani, R. M. Amirthakumari, R. Rita, and C. Ravi, "Electronic Structure Calculations and Physical Properties of ABX_2(A = Cu, Ag; B = Ga, In; X = S, Se, Te) Ternary Chalcopyrite Systems," *Physica Status Solidi (B)*, vol. 213, no. 2, pp. 349-363, Jun. 1999.

[15] A. H. Ammar, A. M. Farid, and M. A. M. Seyam, "Heat treatment effect on the structural and optical properties of $AgInSe_2$ thin films," *Vacuum*, vol. 66, no. 1, pp. 27-38, Jun. 2002.

[16] D. I. Ismayilov and N. K. Kerimova, "Formation of phases in the films of a Ag-In-Se system," *Semiconductors*, vol. 43, no. 9, pp. 1111-1114, Sep. 2009.

[17] K. Yoshino et al., "Structural and electrical characterization of $AgInSe_2$ crystals grown by hot-press method," *Journal of Physics: Conference Series*, vol. 100, no. 4, p. 042042, Mar. 2008.

[18] K. Yamada, N. Hoshino, and T. Nakada, "Crystallographic and electrical properties of wide gap $Ag(In_{1-x},Ga_x)Se_2$ thin films and solar cells," *Science and Technology of Advanced Materials*, vol. 7, no. 1, pp. 42-45, Jan. 2006.

[19] J. H. Boyle, B. E. McCandless, G. M. Hanket, and W. N. Shafarman, "Structural characterization of the $(AgCu)(InGa)Se_2$ thin film alloy system for solar cells," *Thin Solid Films*, Jan. 2011.

[20] T. F. Ciszek, R. Bacewicz, D. Dunlavy, S. K. Deb, and J. R. Durrant, "Crystal growth and photoelectrical properties of $Cu_xAg_{1-x}InSe_2$ and $CuIn_yGa_{1-y}Se_2$ solid solutions," *19th IEEE Photovoltaic Specialists Conference*, pp. 1448-1453, 1987.

[21] U.-C. Boehnke and G. Kühn, "Phase relations in the ternary system Cu-In-Se," *Journal of Materials Science*, vol. 22, no. 5, pp. 1635-1641, May 1987.

[22] C. J. Kiely, R. C. Pond, G. Kenshole, and a. Rockett, "A TEM study of the crystallography and defect structures of single crystal and polycrystalline copper indium diselenide," *Philosophical Magazine A*, vol. 63, no. 6, pp. 1249-1273, Jun. 1991.

[23] I. Bodnar, I. Viktorov, and S. Sergeev-Nekrasov, "$Cu_{1-x}Ag_xInSe_2$ Solid Solutions," *Crystal Research and Technology*, vol. 33, no. 6, pp. 885–890, 1998.

[24] P. Ramesh, "Photoconductive response of polycrystalline n-$AglnSe_2$ thin films," *Vacuum*, vol. 47, no. 3, pp. 211-213, Mar. 1996.

[25] O. Madelung, *Semiconductors: data handbook*. Springer Verlag, 2004, p. 691.

[26] M. A. Contreras et al., "Progress toward 20% efficiency in $Cu(In,Ga)Se_2$ polycrystalline thin-film solar cells," *Progress in Photovoltaics: Research and Applications*, vol. 7, no. 4, pp. 311-316, Jul. 1999.

[27] Y. M. Strzhemechny et al., "Near-surface electronic defects and morphology of $CuIn_{1-x}Ga_xSe_2$," *Journal of Vacuum Science & Technology B: Microelectronics and Nanometer Structures*, vol. 20, no. 6, p. 2441, 2002.

[28] D. Liao and A. Rockett, "Epitaxial growth of $Cu(In, Ga)Se_2$ on GaAs(110)," *Journal of Applied Physics*, vol. 91, no. 4, p. 1978, 2002.

[29] P. Ramesh, "Photoconductive response of polycrystalline n-$AglnSe_2$ thin films," *Vacuum*, vol. 47, no. 3, pp. 211-213, Mar. 1996.

[30] P. Ramesh, S. Uthanna, B. Naidu, and P. Reddy, "Characteristics of Ni/nAgInSe polycrystalline thin film Schottky barrier diodes," *Thin Solid Films*, vol. 292, no. 1-2, pp. 290-292, Jan. 1997.

[31] H. Mustafa, D. Hunter, A. Pradhan, U. Roy, Y. Cui, and A. Burger, "Synthesis and characterization of $AgInSe_2$ for application in thin film solar cells," *Thin Solid Films*, vol. 515, no. 17, pp. 7001-7004, Jun. 2007.

[32] M. Santhosh Kumar, "Formation and properties of $AgInSe_2$ thin films by co-evaporation," *Vacuum*, vol. 72, no. 4, pp. 369-378, Jan. 2004.

[33] P. Paul Ramesh, S. Uthanna, B. Srinivasulu Naidu, and P. Jayarama Reddy, "Optical absorption studies on single-phase polycrystalline $AglnSe_2$ thin films," *Journal of Materials Science Letters*, vol. 15, no. 2, pp. 116-119, 1996.

[34] D. Liao and A. Rockett, "Cu depletion at the $CuInSe_2$ surface," *Applied Physics Letters*, vol. 82, no. 17, p. 2829, 2003.

[35] D. Liao and A. Rockett, "Cd doping at the $CuInSe_2$/CdS heterojunction," *Journal of Applied Physics*, vol. 93, no. 11, p. 9380, 2003.

[36] I. Olekseyuk and O. Krykhovets, "The Ag_2Se–In_2Se_3–$SnSe_2$ system," *Journal of Alloys and Compounds*, vol. 316, no. 1-2, pp. 193-202, Mar. 2001.

[37] K. Koitabashi, S. Ozaki, and S. Adachi, "Optical properties of single-crystalline chalcopyrite semiconductor $AgInSe_2$," *Journal of Applied Physics*, vol. 107, no. 5, p. 053516, 2010.

[38] S. Ozaki and S. Adachi, "Optical absorption and photoluminescence in the ternary chalcopyrite semiconductor $AgInSe_2$," *Journal of Applied Physics*, vol. 100, no. 11, p. 113526, 2006.

[39] A. El-Korashy, "Optical absorption studies on $AgInSe_2$ and $AgInTe_2$ thin films," *Thin Solid Films*, vol. 338, no. 1-2, pp. 207-212, Jan. 1999.

[40] K. Yoshino, "Optical and electrical properties of $AgIn(SSe)_2$ crystals," *Physica B: Condensed Matter*, vol. 302-303, pp. 349-356, 2001.

[41] S. Ozaki and S. Adachi, "Optical properties and electronic band structure of $AgInSe_2$," *Physica Status Solidi (a)*, vol. 203, no. 11, pp. 2919-2923, Sep. 2006.

[42] M. S. Al-Kotb, W. Puff, S. A. Hassan, and M. Mohsen, "A Study of Vacancy-Like Defects in the Chalcopyrite Semiconductor $AgInSe_2$," *Materials Science Forum*, vol. 363-365, pp. 150-152, 2001.

[43] R. Weir, P. Jessop, and B. Garside, "Growth and annealing of $AgInSe_2$ thin films," *Canadian Journal of Physics*, vol. 65, no. 8, pp. 1033–1036, 1987.

[44] J. Shay, B. Tell, H. Kasper, and L. Schiavone, "Electronic Structure of $AgInSe_2$ and $CuInSe_2$," *Physical Review B*, vol. 7, no. 10, pp. 4485–4490, 1973.

[45] K. Kishigui, K. Abe, G. Murakami, Y. Shim, K. Yoshino, and K. Wakita, "Study of steady-state photoluminescence of $AgInSe_2$ crystals," *Thin Solid Films*, vol. 517, no. 4, pp. 1445-1448, Dec. 2008.

[46] N. Goyal, "Electrical and photo-electrical properties of a chalcopyrite semiconductor $AgInSe_2$," *Pramana*, vol. 40, no. 2, pp. 97-105, Feb. 1993.

[47] J. G. Albornoz, R. Serna, and M. León, "Optical properties and electronic structure of polycrystalline $Ag_{1-x}Cu_xInSe2$ alloys," *Journal of Applied Physics*, vol. 97, no. 10, p. 103515, May 2005.

[48] S. Ozaki and S. Adachi, "Temperature dependence of the lowest-direct-bandgap energy in the ternary chalcopyrite semiconductor $AgInSe_2$," *Journal of Materials Science: Materials in Electronics*, vol. 18, no. 1, pp. 25-28, Mar. 2007.

[49] C. M. Joseph and C. S. Menon, "Electrical conductivity , optical absorption and structural studies in $AgInSe_2$ thin films," *Semiconductor Science and Technology*, vol. 11, pp. 1668-1671, 1996.

[50] A. Rockett, *The materials science of semiconductors*, vol. 11, no. 5, Springer Verlag, 2007.

[51] R. Bacewicz, J. R. Durrant, T. F. Ciszek, and S. K. Deb, "Optical and electrical properties of $Cu_xAg_{1-x}InSe_2$ and $CuIn_yGa_{1-y}Se_2$ alloys," *Ternary and Multinary Compounds. Proceedings of the 7th International Conference*, pp. 155-160, 1987.

[52] T. Ciszek, "Melt growth and some properties of $Cu_xAg_{1-x}InSe_2$ and $CuIn_yGa_{1-y}Se_2$ chalcopyrite solid solution crystals," *Journal of Crystal Growth*, vol. 79, no. 1-3. pp. 689-694, Dec-1986.

[53] D. Abdel-hady and A. M. Salem, "Electrical resistivity of $AgInSe_2$ films," *Physica A: Statistical and Theoretical Physics*, vol. 242, no. 1-2, pp. 141-149, Aug. 1997.

[54] Y. Ema, H. Kato, and T. Takahashi, "Ge Doping Effect on Properties of $AgInSe_2$ Thin Films," *Japanese Journal of Applied Physics*, vol. 41, no. Part 1, No. 3A, pp. 1527-1531, Mar. 2002.

[55] P. T. Erslev, G. M. Hanket, W. N. Shafarman, and J. D. Cohen, "Characterizing the effects of silver alloying in chalcopyrite CIGS solar cells with junction capacitance methods," *Materials Research Society Symposium Proceedings*, vol. 1165, pp. 1165-M01-07, 2009.

[56] K. Ramanathan, G. Teeter, J. Keane, and R. Noufi, "Properties of high-efficiency CuInGaSe thin film solar cells," *Thin Solid Films*, vol. 480-481, pp. 499-502, Jun. 2005.

[57] T. K. Todorov, K. B. Reuter, and D. B. Mitzi, "High-Efficiency Solar Cell with Earth-Abundant Liquid-Processed Absorber," *Advanced Materials*, vol. 22, no. 20, p. E156-E159, May 2010.

[58] V. K. Kapur, A. Bansal, O. I. Asensio, P. Le, and N. K. Shigeoka, "Fabrication of CIGS Solar Cells via Printing of Nanoparticle Precursor Inks," *DOE Solar Program Review Meeting*, pp. 135-136, 2004.

[59] Q. Guo, G. M. Ford, H. W. Hillhouse, and R. Agrawal, "Sulfide nanocrystal inks for dense $Cu(In_{1-x}Ga_x)(S_{1-y}Se_y)_2$ absorber films and their photovoltaic performance.," *Nano letters*, vol. 9, no. 8, pp. 3060-5, Aug. 2009.

[60] C. Eberspacher, K. Pauls, and J. Serra, "Non-vacuum processing of CIGS solar cells," in *Conference Record of the Twenty-Ninth IEEE Photovoltaic Specialists Conference, 2002.*, pp. 684-687.

[61] R. Noufi et al., "Investigation of the microstructure of $Cu(In,Ga)Se_2$ thin films used in high-efficiency devices," *Conference Record of the Twenty-Ninth IEEE Photovoltaic Specialists Conference*, May, pp. 508-510, 2002.

[62] U. Rau, M. Schmidt, A. Jasenek, G. Hanna, and H. Schock, "Electrical characterization of $Cu(In,Ga)Se_2$ thin-film solar cells and the role of defects for the device performance," *Solar energy materials and solar cells*, vol. 67, no. 1-4, pp. 137–143, 2001.

[63] W. Shafarman, C. Thompson, J. Boyle, G. Hanket, P. Erslev, and J. D. Cohen, "Device characterization of $(AgCu)(InGa)Se_2$ solar cells," *35th IEEE Photovoltaic Specialists Conference (PVSC), 2010*, pp. 000325–000329.

[64] T. Nakada, K. Yamada, R. Arai, H. Ishizaki, and N. Yamada, "Novel Wide-Band-Gap $Ag(In_{1-x}Ga_x)Se_2$ thin film solar cells," *Materials Research Society Symposium Proceedings*, vol. 865, pp. F11.1.1-8, 2005.

[65] P. P. Ramesh, O. M. Hussain, S. Uthanna, B. S. Naidu, and P. J. Reddy, "Characterization of p-$AgInSe_2$/n-$Zn_{0.35}Cd_{0.65}S$ polycrystalline thin film heterojunctions," *Materials Science and Engineering B*, vol. 49, no. 1, pp. 27–30, 1997.

[66] P. Paul Ramesh, O. M. Hussain, S. Uthanna, B. Srinivasulu Naidu, and P. Jayarama Reddy, "Photovoltaic performance of p-$AgInSe_2$/n-CdS thin film heterojunctions," *Materials Letters*, vol. 34, no. 3-6. pp. 217-221, Mar-1998.

[67] D. Raviendra and J. K. Sharma, "n-CdS/p-$AgInSe_2$ solar cells by electrodeposition," *Physica Status Solidi (a)*, vol. 88, no. 1, pp. 365-368, Mar. 1985.

[68] B. Tell, P. M. Bridenbaugh, and H. Kasper, "Photovoltaic properties of Cu_2Se-$AgInSe_2$ heterojunctions," *Journal of Applied Physics*, vol. 47, no. 2, pp. 619-620, 1976.

[69] G. Hanket, J. H. Boyle, and W. N. Shafarman, "Characterization and device performance of (AgCu)(InGa)Se_2 absorber layers," *34th IEEE Photovoltaic Specialists Conference (PVSC)*, pp. 001240-001245, Jun. 2009.

[70] K. Hjelt and J. Krustok, "Photoluminescence of $AgInSe_2$," *Ternary and Multinary Compounds. Proceedings of the 11th International Conference*, pp. 441-444, 1998.

2.8 Figures

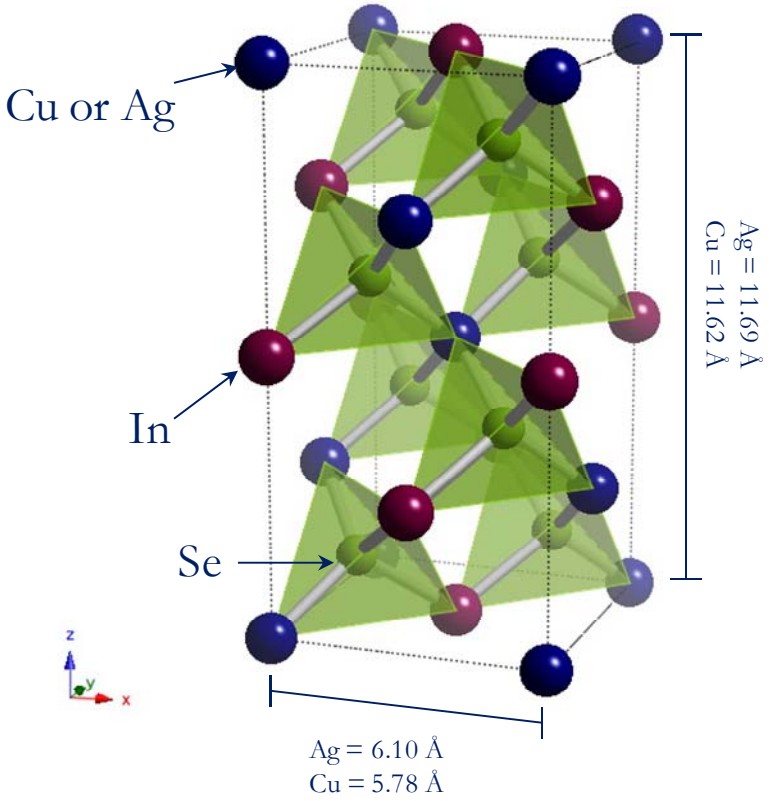

Figure 2.1. Atomic Structure of $Cu_xAg_{1-x}InSe_2$. Image courtesy of A. Hall.

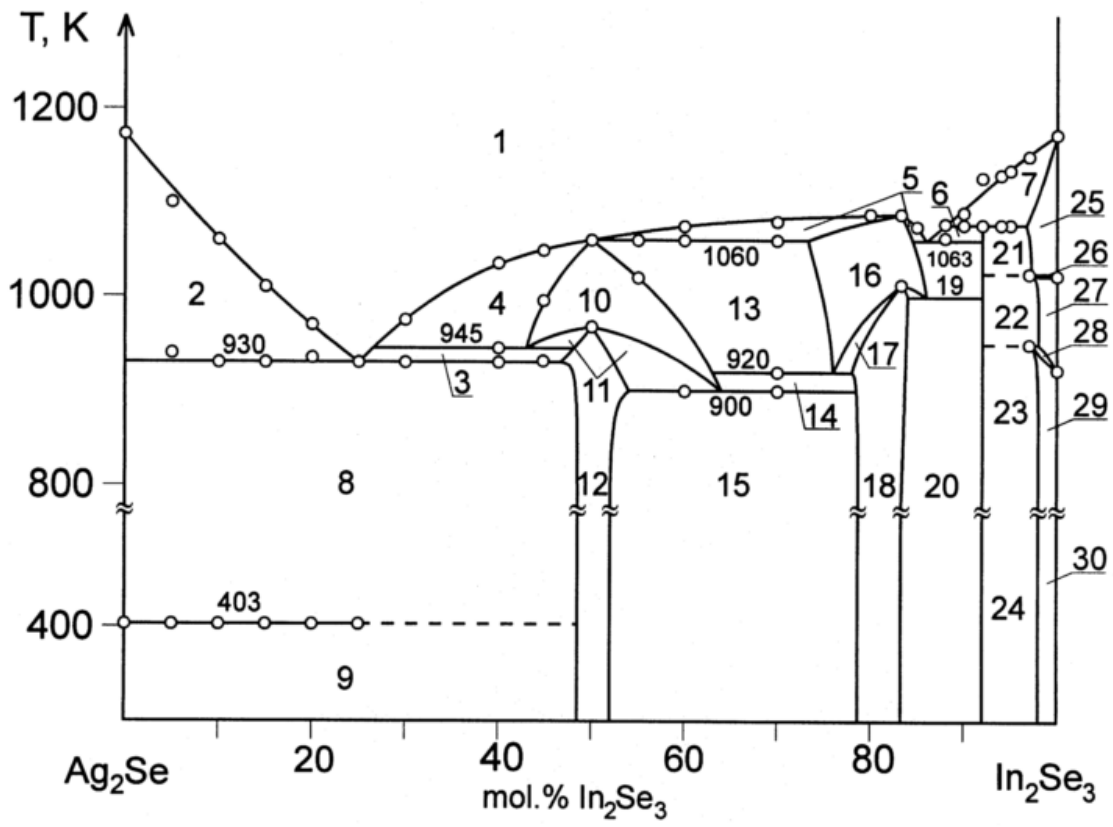

Figure 2.2. Ag_2Se - In_2Se_3 binary phase diagram after Reference [36]. Reprinted from Journal of Alloys and Compounds, 316 /1-2, I.D Olekseyuk,O.V Krykhovets, The Ag_2Se–In_2Se_3–$SnSe_2$system, 10, Copyright 2001, with permission from Elsevier.

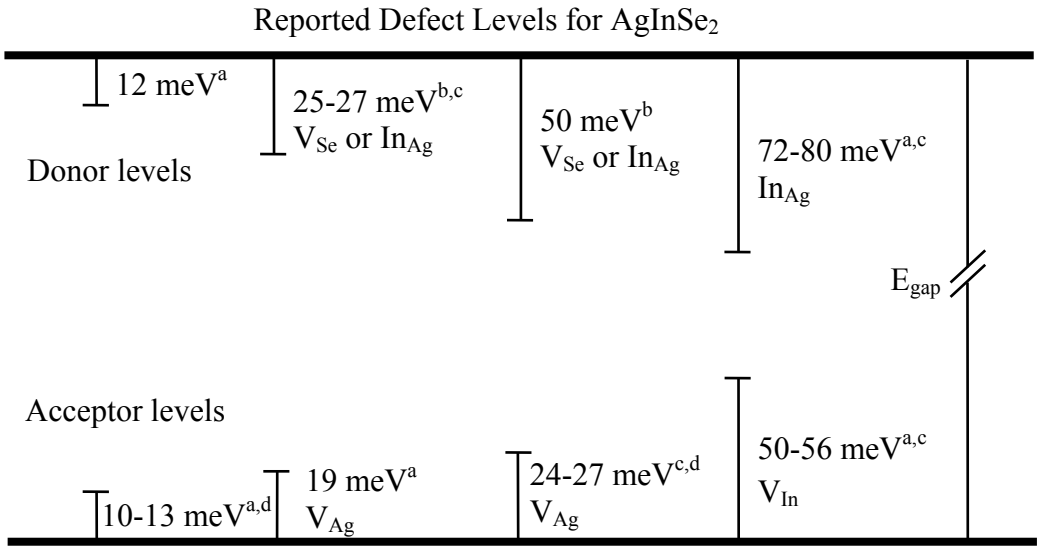

a) Hjelt [70]
b) Kishigui [45]
c) Al Kotb [42]
d) Ozaki [38][38]
e) Yoshino [40] Ag_i and V_{in} for DAP peak at 0.90 eV

Figure 2.3. Reported defect levels in the literature for $AgInSe_2$ with assigned point defects.

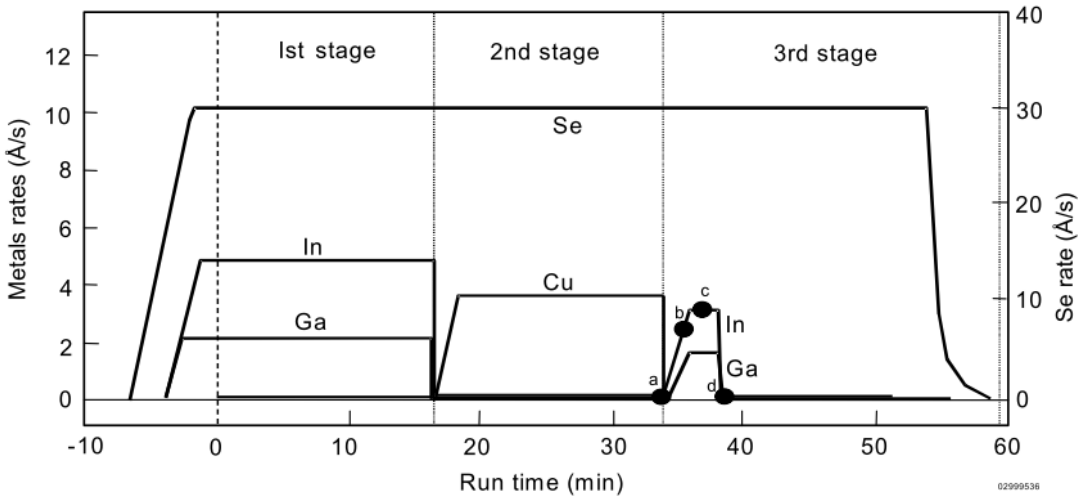

Figure 2.4. Schematic of three-stage deposition method for I-III-VI_2 solar cell absorber layers. There are several variants of this process. After Reference [61]. Reprinted from 29th IEEE PVSC-Conference Paper, R. Noufi, Y. Yan, J. Abu-Shama, KI. Jones, M. Al-Jassim, B. Keyes, J. Alleman, and K. Ramanathan, Investigation of the microstructure of Cu(In,Ga)Se_2 thin films used in high-efficiency devices, Copyright 2002.

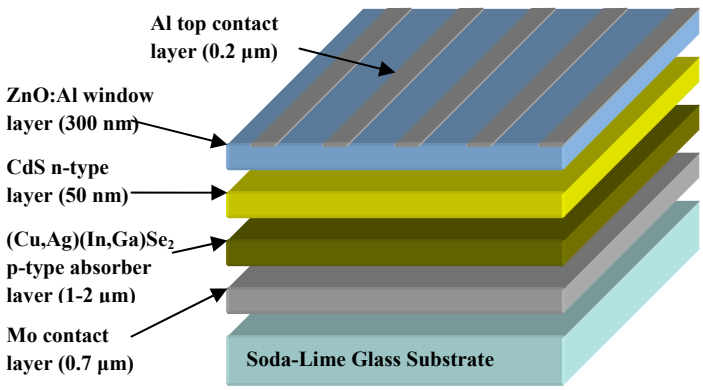

Figure 2.5. Device structure of a (Cu,Ag)(In,Ga)Se_2 thin-film solar cell.

CHAPTER 3

EXPERIMENTAL METHODS

3.1 Introduction

The growth methods and equipment used to deposit the films used in this study are described in detail in the first section of this chapter. This is followed by discussion of the analysis techniques used to characterize the films, including structural, chemical, electrical, and optical properties. Detailed descriptions of the equipment and analysis conditions are given for each set of experiments.

3.2 Deposition of $Cu_xAg_{1-x}InSe_2$ Thin Films

The $Cu_xAg_{1-x}InSe_2$ thin films used in this work were deposited by direct current (dc) magnetron sputtering by our collaborators at the University of Toledo, Scott A. Little and Professor Sylvain Marsillac [1]. Polycrystalline thin films were deposited using an ultra-high vacuum chamber with a base pressure of 10^{-8} Torr. An illustration of this chamber can be seen in Figure 3.1 together with a photograph of the actual system. A hybrid deposition scheme was used in which Ag, Cu, and In were sputtered and elemental Se was thermally evaporated from an effusion cell. Soda-lime glass substrates were placed on a rotating substrate holder at a temperature of 550 °C, unless otherwise noted. This ensures spatial uniformity during deposition. Ar (99.998%) was used as the sputtering gas and its pressure was kept at 2.5 mTorr during film deposition.

Unlike high-efficiency three-stage processes, all the films used in this work were deposited using a single-stage growth process (all parameters were held constant during

film deposition). Six $Cu_xAg_{1-x}InSe_2$ thin films were deposited at composition intervals of x = 0.2, where x = Cu/(Cu+Ag). The In target sputtering power was left constant throughout deposition of the compositional series at 37 W, except where otherwise noted. The Cu and Ag sputtering powers were varied according to the desired film composition, with values ranging from 0-23 W for the Cu target and 0-36 W for the Ag target (see Table 3.1). The Se evaporation source was held at 340 °C during deposition or at a rate of ~ 8 Å/s. The substrate and target shutters remained open for film deposition for a total of 25 minutes. The substrates were allowed to cool after deposition for 2 hrs with no additional heating.

Polycrystalline films with thicknesses of 700 nm were obtained, except where otherwise noted. Films for optical experiments were deposited on bare soda-lime glass substrates (or sometimes on 25 nm of thermally grown oxide (SiO_2) on Si (100) substrates) while films for electrical experiments were deposited on Mo-coated soda-lime glass substrates. Films on bare glass make optical experiments like transmission and reflection easier to perform. Films on molybdenum provide a back contact for electrical characterization work and device fabrication.

3.3 In Situ Growth Monitoring

Film growth was monitored during deposition using an in situ ellipsometry system such as the one seen in the photograph of Figure 3.1. Real-time spectroscopic ellipsometry (RTSE) data was acquired by our collaborators [1] using a rotating-compensator multichannel ellipsometer with a photon energy range of 0.75-6.5 eV at an angle of incidence of 65°. An optical model based on a 4-layer structure consisting of

surface roughness, the $Cu_xAg_{1-x}InSe_2$ film, a 25 nm SiO_2 film, and the Si substrate. The surface roughness was simulated with a Bruggeman effective medium approximation (EMA) composed of a 50/50 mixture of void and $Cu_xAg_{1-x}InSe_2$. The experimental data were fit assuming this model and then numerically inverted to extract the dielectric functions, thickness, and roughness using least-squares regression algorithms [1].

3.4 Structural Characterization Methods

The structure and texturing of all the films was studied using the X-ray diffraction technique (XRD). Films were placed in a Phillips X'Pert diffractometer system for ω-2θ scans. This system uses a Cu source with $K_{\alpha 1}$ radiation (λ=0.1540598 nm) and thin film parallel plate collimator secondary optics. A 2θ range from 20° to 55° was examined using a step size of 0.01 and counting time of 2 seconds per step. This analysis range was selected based on areas of interest from lower resolution overview scans which covered a much wider 2θ range (10°-90°). The data was then compared to powder diffraction files and analyzed using standard fitting techniques. Crystallite size, preferred crystal orientation, and secondary phase formation can be determined from this data.

Film structure and mapping of the grains were also studied via Electron Backscatter Diffraction (EBSD). Electrons have an advantage over x-rays because they offer better lateral resolution and ease of manipulation. This allows us to probe the micro/nano-structure of the films. The shallow escape depth of electrons also means that the technique is very surface sensitive.

EBSD experiments were carried out inside a JEOL 7000F Analytical Scanning Electron Microscope (SEM with a Schottky field emission gun). This SEM is equipped

with an HKL EBSD system that includes a phosphor screen in which the diffraction pattern is formed and a charge-coupled device camera for recording the diffraction pattern that forms on the screen. The sample was tilted at 70° relative to horizontal in order to improve collection. A schematic of the system is shown in Figure 3.2. An accelerating voltage of 30 kV and beam currents of up to 16 nA were used for all EBSD experiments. The crystal orientation mapping technique was used in order to generate maps of grain orientation in the films. In this technique the beam was scanned over the sample from point-to-point, collecting diffraction patterns at each point. These patterns were then analyzed in order to map the different crystal properties of interest.

Other grain properties such as grain size and shape were studied using an Atomic Force Microscope (AFM) and a SEM. An Asylum Research MFP-3D AFM was used for all the scans. Scanning was carried out using tips from BudgetSensors (TAP300AL) with a tip radius < 10 nm. Scan speeds were kept below 1 Hz (typically 0.5 Hz) in order to ensure proper tracking of surface features. SEM studies were carried out in a JEOL 7000F SEM, the same instrument used for EBSD studies. Low voltages (< 5 kV) and currents (< 1 nA) were used to enhance surface features on our samples during high resolution imaging.

Further structural characterization was carried out using electron diffraction in a Transmission Electron Microscope (TEM). A standard JEOL 2010F LaB_6 TEM was used at 200 kV together with a double-tilt holder. Diffraction patterns were then compared with computer simulations for structure verification. Plan-view and cross-sectional samples were thinned by manual grinding on three different Buehler silicon carbide papers (P1200, P2400, P4000) and polished on a Vel-Cloth polishing cloth (1/4

μm) with three different colloidal alumina suspensions (3 μm, 1 μm, 0.3 μm). After thinning down to a thickness of 40 μm, the films were then ion milled until a hole emerged in the center of the sample (~ 2-8 hours). All ion milling was performed in a Fischione ion miller using a cooling stage to prevent diffusion of Cu or Ag during the process.

3.5 Chemical Characterization Methods

Film composition was studied using a combination of techniques. Energy dispersive x-ray spectroscopy (EDS) was used inside an SEM in order to determine film composition after growth. Since the films are fairly thin (~ 700 nm), accelerating voltages of 15 kV and 10 kV were used looking only at the Cu, Ag, In, and Se L peaks. Accelerating voltages were selected based on computer simulations using CASINO. Voltages were chosen such that at least 95% of the signal was within the thin-film region. A Thermo Electron EDS system was used for all measurements using a Proza (Phi-Rho-Z) correction method. These compositions were confirmed by analyzing the peak shifts in XRD data. In addition to standard EDS, Nano-EDS was also carried out inside a JEOL 2010F TEM.

Compositional uniformity as a function of depth was also studied in all films. This was done using the secondary ion mass spectrometry (SIMS) technique. A Physical Electronics PHI Trift III SIMS system was used for depth profiling. This is a Time of Flight system that uses Au ions as the analysis beam and Cs or O for the sputtering beam. Positive secondaries were analyzed during profiling using a Cs beam. The Cs beam was set at 2 kV and 50-120 nA. An area of 400 μm x 400 μm was sputtered for 10 seconds.

A bunched Au beam at 22 kV and 2 nA was used for analysis. The analysis beam was set to raster an area of 50 μm x 50 μm and signal was collected for 20 seconds from a range of 0-300 atomic mass units (amu). Profiling was carried out throughout the entire film until reaching the film/glass interface.

The Rutherford backscattering spectrometry (RBS) technique was used to obtain film thickness and confirm compositional measurements obtained from EDS. The probe beam consisted of He^{4+} ions accelerated at 2 MeV towards the target or sample. The incoming beam was at a 22.5° angle from the sample surface normal while the detector was set at a 150° scattering angle. The data was then fit using the SIMNRA simulation package [2] by adjusting the substrate part of the profile first and then adjusting thickness and composition of the layer of interest. Dual-scattering was enabled in the simulation in order to obtain accurate fits.

X-ray photoelectron spectroscopy measurements (XPS) were carried out in a Kratos Axis ULTRA high-performance x-ray photoelectron spectrometer with a monochromatic Al K_α (1486.7 eV) excitation source. These measurements were used to measure the positions of the orbitals that make up the valence band maximum.

3.6 Optical Characterization Methods

Thin films were optically characterized using transmission, reflection, and luminescence techniques. Room-temperature optical band gaps were extracted from transmission/reflection measurements. These were carried out in a Varian Cary 5G spectrophotometer using a range from 200 nm - 1500 nm. Optical absorption coefficients

were calculated from the measured transmission and reflection profiles using the following equation:

$$T \approx (1 - R)^2 e^{-\alpha t} \tag{3.1}$$

where T is the measured transmission, R is the measured reflection, α the absorption coefficient, and t the film thickness. Band gaps were extracted graphically using a Tauc plot [3-4] by plotting $(\alpha * h\nu)^n$ vs hν and using the x-axis intercept of a linear fit to the Tauc plot. The value of the exponent, n, indicates the type of transition involved: $n = ½$ indicates an indirect band transition, and $n = 2$ indicates a direct band transition [4].

Optical transition energies and shallow defect levels were calculated from measurements of the films' photoluminescence (PL). Samples were loaded into a Janis Research liquid He-bath cryostat (see Figure 3.3), and cooled to 4 K. The films were excited using a frequency-doubled Lightwave Nd:YAG laser (λ = 532 nm) for power- and temperature-dependent studies. A lock-in amplifier was used while chopping the excitation source at a frequency of 25 Hz. All power-dependent spectra were acquired at a constant temperature of 4 K while all temperature-dependent spectra were acquired at constant excitation power of 10 mW. Emissions were analyzed using an Acton Spectra Pro-300i 0.3 m single grating monochromator and detected by a liquid N_2-cooled Ge detector (range: 900-1800 nm). A complete instrument response function (IRF) (gratings, filters, lenses, and detector response) was used to correct the data for system sensitivity. A calibrated white light source (Labsphere, SPH-4) was used during acquisition of the IRF.

PL measurements were confirmed by studying the cathodoluminescence (CL) of the films. Cryogenic CL was performed on as-deposited films. The experiments were carried out in a JEOL (JSM-7000F) analytical scanning electron microscope fitted with a Gatan MonoCL3 cathodoluminescence spectrometer, a liquid helium cooled sample stage, and a liquid nitrogen cooled Ge detector. The electron beam accelerating voltage was set at 15 kV and the current at 200 pA, except where otherwise noted. Power-dependent CL spectra were collected in order to study the behavior of the peaks. Accelerating voltages remained constant (15 kV) while excitation currents were varied from 22 pA up to 138,000 pA (aperture limits), following a geometric series in between. The sample temperature was 10 K when the spectra were collected. CL imaging was also carried out on the films. Mono-chromatic and pan-chromatic images were acquired from areas of interest in order to study the spatial distribution of defects in the films.

A measure of material quality was determined from time-resolved photoluminescence (TRPL) spectroscopy. All measurements were carried out by Darius Kuciauskas from the National Renewable Energy Laboratory (NREL). TRPL decays were measured using the time correlated single photon counting technique. The excitation source was an optical parametric amplifier (OPA) and a regeneratively amplified Ti:Sapphire laser system (λ = 630 nm). The repetition rate was set at 250 kHz and the pulse length at around 200 fs. Luminescence was measured using a near-infrared sensitive PMT detector (R5509 from Hamamatsu) with sensitivity < 1370 nm. The instrument response was obtained by measuring light scattering from a sample holder at 630 nm. A monochromator was used to select the wavelength for the measurement.

3.7 Electrical Characterization Methods

Electrical properties were measured using the Hall Effect technique. A custom-made Hall Effect system was used for all measurements. Samples were prepared by cutting into squares of 10 mm x 10 mm and depositing Au contact pads (1 mm diameter, 500 nm thick) in the Van der Pauw configuration, as seen in Figure 3.4. The samples were loaded into a cryogenic head (CTI-Cryogenics) and In leads were soldered to the Au pads. The cryogenic head was pumped down into the mTorr range and was followed by cooling from a closed-cycle refrigerator system (CTI-Cryogenics 8200 Compressor) that was controlled with a LakeShore 330 auto-tuning temperature controller. The head was then placed between the pieces of a 1 Tesla electromagnet (Varian Associates) for Hall Effect measurements. Voltages and currents were applied and read using an MMR Technologies H-50 Hall controller box. All the hardware was controlled using a home-built LabVIEW code, which performs the Hall Effect measurements following the ASTM Designation F76 standard [5]. Measurements were performed at different temperatures by using a heater that sits under the sample stage. The system was also calibrated using a GaAs standard.

3.8 Additional Sample Preparation

In order to obtain high quality indexing of electron backscatter patterns (EBSPs) and reduce topographical effects in CL imaging, flat samples are preferred. Our films, being polycrystalline, have a large roughness (~ 300 nm RMS) compared to the overall film thickness (~ 700 nm). This leads to lower quality EBSPs and a higher chance of errors in the indexing of the patterns. Polishing the films would lead to better quality

EBSPs. This was accomplished by using a cross-sectional ion polisher. Each sample was attached to a brass or molybdenum block with Crystalbond™ 509-3 wax (Ted Pella, Inc., flow point 121°C). They were planarized in an argon-beam cross section polisher (IB-09010CP, JEOL USA) for one to 20 minutes at an accelerating voltage of 5 kV with the ion beam perpendicular to the sample surface and the sample rotated +/- 30° during the milling cycle. EBSD and additional CL measurements were then performed on these planarized films after a thin carbon film was deposited in order to reduce charging of the samples and subsequent drifting.

3.9 References

[1] T. Begou et al., "In situ and ex situ Characterization of (Ag,Cu)$InSe_2$ Thin Films," *Conference Record 37th IEEE Photovoltaic Specialists Conference*, 2011.

[2] M. Mayer, "SIMNRA Home Page." [Online]. Available: http://home.rzg.mpg.de/~mam/. [Accessed: 10-Mar-2012].

[3] J. Tauc, R. Grigorovici, and A. Vancu, "Optical properties and electronic structure of amorphous germanium," *physica status solidi (b)*, vol. 15, no. 2, pp. 627–637, 1966.

[4] J. I. Pankove, *Optical Processes in Semiconductors*, Second Edition Dover Publications, 2010, p. 448.

[5] ASTM, "Standard Test Methods for Measuring Resistivity and Hall Coefficient and Determining Hall Mobility in Single-Crystal Semiconductors," *Annual Book of ASTM Standards*, vol. F-76-08, pp. 1-14, 2009.

[6] A. Day and P. Trimby, *Channel 5 User Manual*. HKL Technologies, 2004.

3.10 Tables

Composition	Target Sputtering Powers (Watts)			Film thickness (nm)
x	In	Ag	Cu	
0	12	15	0	300
0.2	37	36	5	700
0.4	37	25	9	700
0.6	37	16	14	700
0.8	37	6	19	700
1	37	0	23	700

Table 3.1. Deposition parameters for $Cu_xAg_{1-x}InSe_2$ thin-films.

3.11 Figures

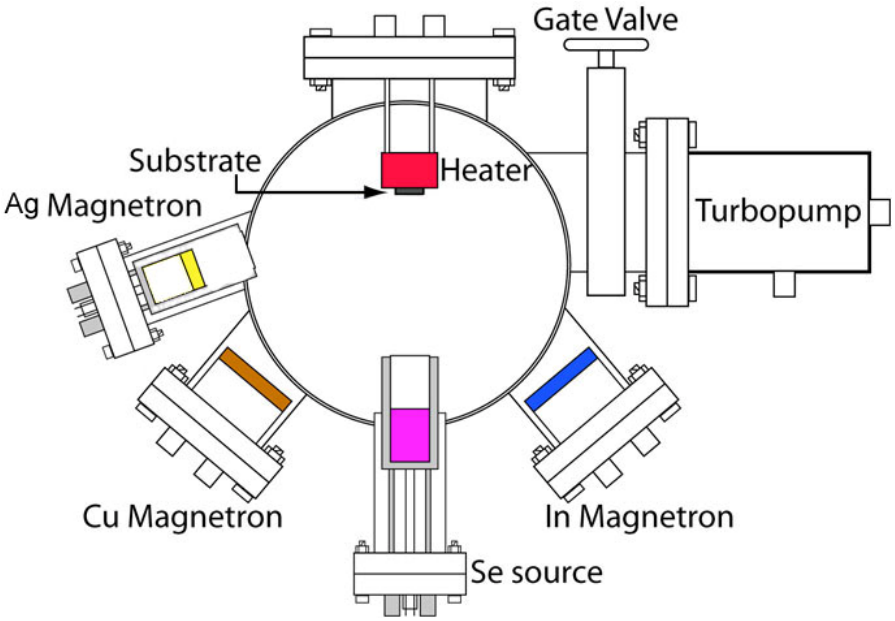

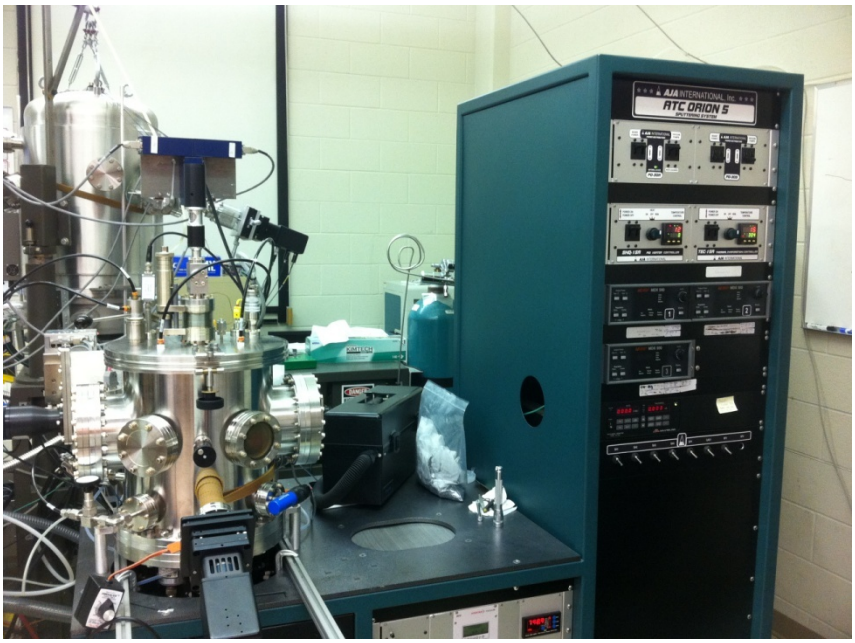

Figure 3.1. Schematic (upper) and photograph (lower) of hybrid deposition system used to deposit thin films of $Cu_xAg_{1-x}InSe_2$. Cu, In, and Ag were sputtered while elemental Se was thermally evaporated. The actual system is a customized AJA ATC Orion 5. It has three target holders, a selenium effusion cell, a rotating substrate holder, two infra-red lamp heaters, a crystal quartz monitor, and an ellipsometry port.

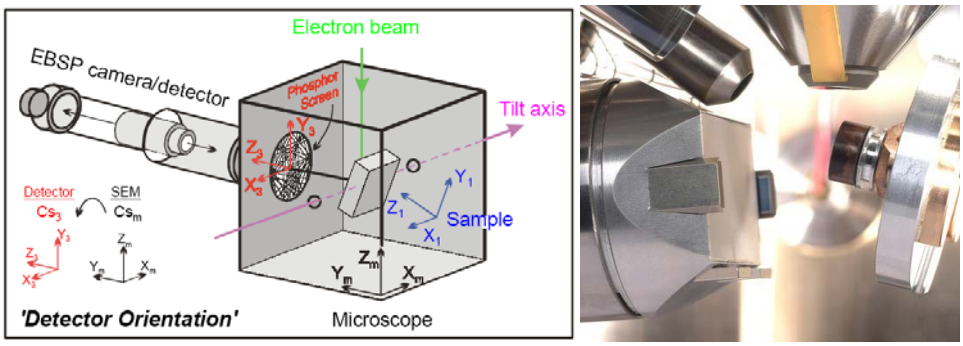

Figure 3.2. Electron back-scattered diffraction (EBSD) setup (6].

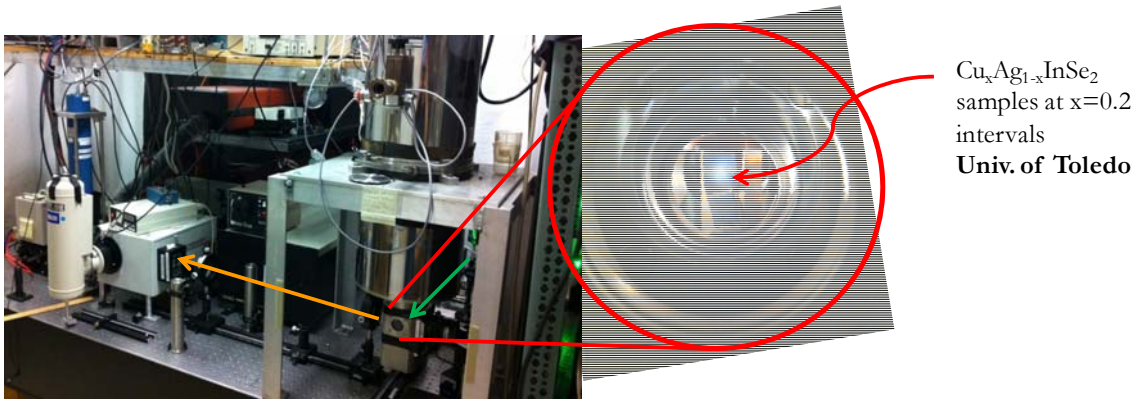

Figure 3.3. Power- and temperature-dependent photoluminescence setup. Samples are loaded into a cryostat which is cooled using liquid helium. A frequency-doubled Nd:YAG laser at 532 nm is used to excite electron-hole-pairs in the material, which eventually recombine giving off light. This luminescence is then focused (orange line) on the spectrometer and reaches the Ge detector.

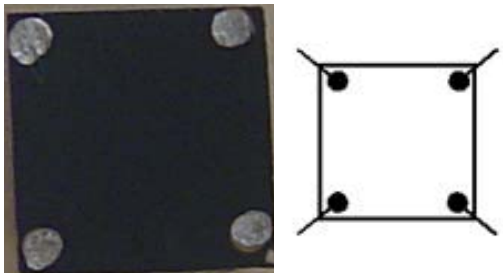

Figure 3.4. Van der Pauw contact configuration for Hall Effect measurements. Au pads were first thermally evaporated and In contacts were then placed on top of the Au pads. This allows for better ohmic contacts to the $Cu_xAg_{1-x}InSe_2$ films at low temperatures.

CHAPTER 4

GROWTH AND PHYSICAL PROPERTIES OF $Cu_xAg_{1-x}InSe_2$ THIN FILMS

In this chapter the $Cu_xAg_{1-x}InSe_2$ (CAIS) thin films used in this work are described in detail. Film growth mode and compositions are discussed in sections 4.2 and 4.3, respectively. Structural properties such as crystallinity, lattice parameters, texturing, and grain size are presented in section 4.4. The optical band gaps, bowing coefficient, and valence band maximum were also studied and are discussed in section 4.5. The $Cu_xAg_{1-x}InSe_2$ thin films were deposited as previously described in Chapter 3.2. Films with thicknesses of 700 nm and at intervals of x = 0.2, where x = Cu/(Cu+Ag), were deposited on bare soda-lime glass substrates and on Mo-coated glass substrates. All films were then characterized in their as-deposited state (no subsequent heat treatments).

4.1 Introduction

Film growth mechanisms have an important influence over the type of defects that form during growth. Different growth mechanisms will yield different structural features in the films that might influence the optoelectronic properties. In this section I present the study of structural differences in the films as a function of composition x = [Cu/(Cu+Ag)] for the CAIS alloy. Identifying these differences facilitates the interpretation of optoelectronic data, which is the focus of this work. The crystallography, morphology, and grain size as a function of composition were studied.

The chemical makeup of a film can also have an influence over the type of electrical and optical properties the film exhibits. Work by other groups in $CuInSe_2$ has

shown that group-I poor films can lead to p-type conductivity, while group-I rich films can lead to n-type conductivity [1–4]. The amount of selenium in the film can also have a similar effect; therefore proper compositional measurements are important when studying a films electrical and optical properties. Optoelectronic properties in I-III-VI_2 thin-films are dominated by the formation of intrinsic point defects (V_{Cu}, In_{Ag}, In_i, etc.) during film growth [4]. The films studied in this work have an additional chemical species (Ag) that will add to the number of point defects possible (V_{Ag}, Ag_i, In_{Ag}, etc.) in the system. Identifying these defects and being able to selectively modify them is crucial in the engineering of high efficiency solar cell devices.

4.2 Growth Modes

Growth parameters were monitored during film deposition on a 25 nm thermal oxide on Si (100) substrates by using in situ ellipsometry as described in Chapter 3.3. Our collaborators identified slightly different types of growth depending on the copper to silver ratio [5]. For all the films, the surface roughness layer appears before the first dense monolayer (ML) (~0.5 nm), which is typical of an islanding or Volmer-Weber (V-W) nucleation mode. However, as *x* decreases, the growth of the first dense monolayer appears earlier, which would ultimately lead to layer followed by islanding or Stranski-Krastanov (S-K) growth mode. A reduction in the free energy density of the interface in the alloys containing silver probably allows for this modification of the growth mode.

4.3 Composition

Compositional studies were carried out as described in Chapter 3.5 by EDS and revealed that all films are slightly off-stoichiometric (see Tables 4.1 and 4.2). All films were group-I deficient, meaning that the existence of group-I vacancies (V_{Cu}, V_{Ag}) and III_I substitutional defects (In_{Cu}, In_{Ag}) is likely in our films. Indium content was slightly above 25 at. % for all the films, further increasing the possibility of forming III_I defects. Selenium content was around 49-51 at.% for most films. The Cu/Ag ratios were confirmed via XRD peak shifts and are in excellent agreement with values of *x* obtained via EDS. Further confirmation was obtained via RBS experiments as seen in Figure 4.1.

The films appear to have uniform composition throughout their thickness, as confirmed via SIMS depth profiling (see Figure 4.2). SIMS also revealed the presence of sodium in all films. This is typical of films deposited on soda-lime glass substrates, as the sodium in the glass diffuses throughout the layer during the deposition process [6-7]. Sodium is known to have beneficial effects on the performance of I-III-VI_2 devices [6–8], so its presence is typically desired. The sodium in the films however has a graded profile, with a higher concentration towards the back of the film.

4.4 Structural Properties

XRD analysis was performed to study phase formation, film texturing, lattice constants, and crystallite size, following the procedures described in Chapter 3.4. ω-2θ scans were acquired for samples on both bare and Mo-coated SLG (Figure 4.3 and 4.4). Single phase materials were found throughout most of the composition space for both substrates, with the exception of the $x = 0.2$ films on both substrates and the $x = 0$ film on

Mo-coated glass. Evidence of an additional phase was observed to the right of the primary AIS peaks [(112), (204), and (215)] at 2θ positions of 26.46°, 43.96°, and 51.99°. These additional peaks match well with powder diffraction data for both the $Ag_3In_5Se_9$ and $AgIn_5Se_8$ phases. Similar phases have been identified before near the surface of $CuInSe_2$ films and are referred to as ordered defect compounds (ODC) [9–11].

Glancing incidence XRD measurements were performed at the (112) peak of AIS and its ODC satellite (Figure 4.5) in order to confirm the location of the ODC. As the probing angle decreased (increased surface sensitivity), the ODC peak increased relative to the main (112) AIS peak, until it became the dominant peak (Figure 4.5). This indicates the presence of the ODC near the surface of the film. This result has been further confirmed via cathodoluminescence imaging, as shown in Figure 7.8b, where higher energy emissions were observed from surface protruding grains, consistent with an ODC near the surface. A similar ODC was observed by Simchi *et al.* [12]. They reported the presence of $AgIn_5Se_8$ in AIS films using XPS and glancing incidence XRD.

All films on Mo-coated SLG showed a preference for $(112)_{tet}$ orientation, consistent with the typical growth of CIGS on Mo-glass [4]. Here we use the "tet" subscript to distinguish the tetragonal from the cubic indices. This result is consistent with observations of the growth of CIS by Liao and Rockett [13] and the theoretical work of Jaffe and Zunger [14], who have shown that $(112)_{tet}$ surfaces in I-III-VI_2 chalcopyrites are lower in energy than the typical zinc-blende (110) nonpolar surface. Films on bare SLG also showed $(112)_{tet}$ preferred orientation, with the exception of films with $x \geq 0.8$, which showed slight (220) preferred orientations as seen in Figure 4.6. The films with (220) preferred orientation also exhibited larger grains. A preference for (220) preferred

orientation has been observed under some processing conditions for CIGS alloys as well [4].

The XRD ω-2θ profiles for each sample were fit using a pseudo-Voigt profile and the peak center positions and lattice parameters calculated (see Tables 4.1 and 4.2). The lattice parameters showed a slight deviation from Vegard's Law in both sets of films in {100} directions, *a*, (Figures 4.7 and 4.8) with two linear regions as a function of film composition (one for $1 \leq x \leq 0.6$ and the other for $0.6 \leq x \leq 0$). The (001) lattice parameter, *c*, deviated severely from Vegard's Law, with a maximum value at $x = 0.4$. A similar behavior was observed by Csizek *et al.* [15] in bulk crystals of this alloy. Variation in *c*/*a* ratio is known to occur in CIGS alloys as well and indicates a change in the position of the Se atoms relative to the center of the cation tetrahedra. Replacing Cu with Ag results in a displacement of the Se toward the In atoms, increasing the tetrahedral distortion in the solid and hence decreasing *c*/*a* (see Figure 4.8).

Trends for the evolution of crystallite size as a function of *x* were studied with XRD, SEM, and TEM for the films on bare SLG. Fitting the $(112)_{tet}$ XRD peak for each of the compositions, the crystallite size can be found using the Scherrer formula [16],

$$X_S = \frac{K\lambda_l}{\beta\cos\theta} \tag{4.1}$$

where *K* is the dimensionless shape factor, λ_l is the x-ray wavelength, β is the diffraction peak full-width-at-half-maximum (FWHM), and θ is the angle of the peak center. This formula does not take into consideration strain or composition variations within the

crystallites as a source of peak broadening; therefore crystallite size will be underestimated. Crystallite sizes were found to vary from 70 nm to 150 nm and did not exhibit any trends with composition, suggesting that composition-driven peak broadening was not a factor. Grain sizes were also calculated from images of the samples (SEM and TEM) using the planimetric method described in ASTM E112 (see Figures 4.9-4.11). All samples, regardless of x, showed significant twinning as seen in Figure 4.10. These twin boundaries were disregarded for purposes of grain size estimates. The results showed an increase in grain size for CIS versus AIS when deposited on bare SLG substrates. TEM images showed grains ranging in size (width and length) from 80 nm to 250 nm for AIS and from 170 nm to 500 nm for CIS. This suggests that grain size increases as x increases for films deposited on bare SLG substrates, which was not an expected outcome, due to the lower melting temperature of AIS.

However, it was found that the substrate plays an important role in determining grain size. Films deposited on Mo-coated SLG exhibited grain sizes up to three times larger than those deposited on bare SLG substrates for compositions of $x \leq 0.6$ (Figure 4.11). The data suggests that Mo has a larger effect on the grains of Ag-dominant films ($x \leq 0.6$) than it does on Cu-dominant films ($x \geq 0.8$). Films in this series also showed an increase in grain size with larger values of the (112)/[(220)/(204)] peak ratios. This was opposite to the behavior observed for films deposited on bare SLG, which showed larger grains for smaller (112)/[(220/204)] peak ratios.

Grain size was also compared for films deposited on bare SLG substrates (with Na) with those deposited on oxidized Si(100) (without Na) in order to study the effects of Na (Figure 4.11). Grain sizes for films with $x \leq 0.6$ did not change much regardless of

the presence of Na. However, for $x \geq 0.8$, films deposited on SLG (i.e.: with Na) showed a doubling of grain size relative to those on oxidized Si. These results suggest that Na does not have the same beneficial effects on AIS as it does on CIS.

4.5 Optical Band Gaps

Optical band gaps and absorption coefficients of the films on bare glass were determined by transmission and reflection measurements. The absorption coefficients were calculated from:

$$T \approx (1 - \mathrm{R})^2 \mathrm{e}^{-\alpha t} \tag{4.2}$$

where T is the measured transmission, R is the measured reflection, α is the absorption coefficient, and t is the film thickness. Band gaps were extracted graphically using an $(\alpha * h\nu)^n$ vs hν or "Tauc" plot [17-18], and using the x-axis intercept of a linear fit to the data on these axes (see Figure 4.12). The value of the exponent, n, indicates the type of transition involved: n = ½ for an indirect band transition, and n = 2 for a direct band transition [18]. Our data fit best with n = 2 indicating direct band gaps for all films.

AIS showed a band gap of 1.24 eV, in line with that measured by Albornoz [19] and others [20–22], while CIS had a band gap of around 1.01 eV. The absorption curves exhibit four distinct regimes (Figure 4.12). For AIS, above 1.38 eV the absorption coefficient decreases linearly with photon energy, corresponding to absorption by states well into the bands. Between 1.33 and 1.37 eV there is a sudden drop in absorption, returning to a slowly changing behavior below 1.33 eV. The absorption drops again below 1.28 eV, showing a quadratic behavior consistent with a free-electron band edge. Finally, below 1.24 eV, α decays exponentially with photon energy, as would be expected

for absorption dominated by a band tail. All films followed this general behavior, however the films with $x = 0.2$ and $x = 0.6$ did not show a pronounced "double knee" in the absorption, likely due to the interaction between the Cu 3*d* and Ag 4*d* orbitals or a distribution of compositions and hence absorption edges.

The CIS ($x = 1$), and $x = 0.8$ alloy samples are nearly identical to within a scale factor (the $x = 0.8$ sample had a higher absorption coefficient). AIS ($x = 0$) shows a similar behavior to CIS, but with a higher bandgap and smaller absorption coefficient. The optical bandgap of the alloy changed with composition (Figure 4.13), exhibiting the general behavior:

$$E_{\Gamma}(x) = 1.24\ eV + (1.01\ eV - 1.24eV)x - 0.224\ eV\ x(1-x) \qquad (4.5)$$

where 0.224 eV is the bowing parameter. J. Boyle, *et al.* [23], reported bowing values of 0.26 eV and 0.20 eV for CIGS and $(Cu,Ag)(In_{0.69}Ga_{0.31})Se_2$, respectively, which are close to the values obtained in this work for CAIS. A striking feature is that the band gap changes very little (~ 50 meV) from $x = 1$ to $x = 0.6$. The same behavior was observed in spectroscopic ellipsometry data reported by Begou *et al.* [5].

The increase in band gap for AIS relative to CIS is due to changes in the valence band structure caused by the substitution of Cu with Ag. The conduction band minimum in I-III-VI_2 semiconductors is derived mostly from group III *s*-orbitals (In 5*s* and Ga 4*s*), while the valence band maximum is mostly derived from the group VI orbitals (Se 4*p*) influenced by the shallow *d*-states from the Ag or Cu [24-25]. The Cu 3*d* orbital lies closer to the valence band maximum than does the Ag 4*d*, increasing the *p*-*d* repulsion in the high Cu alloys and therefore to a smaller energy gap in the high Cu materials [26].

In order to confirm the position and behavior of the Cu and Ag *d*-orbitals, XPS measurements were performed. Photoelectron spectra of the valence band as a function of film composition with the binding energy corrected based on the C 1*s* peak at 285 eV can be seen in Figure 4.14. The dominant contributions of the atomic orbitals are marked in the figure. A significant peak was found in the AIS valence band spectrum at ~ -6 eV which was absent in the CIS data. The latter showed a peak at -4.3 eV which was missing in the AIS results. These presumably correspond to the Ag 4*d* and Cu 3*d* orbitals. The shift in the energy of the valence band maximum, which is a combination of the Se 4*p*-orbital and the group-I *d*-orbitals, in films with $x = 0$ and $x = 1$ was calculated using the base width method of a Gaussian peak. This showed a shift of 0.636 eV, which is the amount by which the valence band maximum moved away from the Fermi energy (BE = 0 eV) in CIS relative to AIS. In general the CIS is moderately p-type so this puts the AIS Fermi energy of a clean surface near the middle of the energy gap, consistent with a bulk-terminated material, and consistent with Hall effect measurements showing a low measured n-type carrier concentration ($\sim 10^{13\text{-}14} cm^{-3}$) in the AIS.

4.6 Conclusions

$Cu_xAg_{1-x}InSe_2$ thin films were deposited by dc magnetron sputtering and their physical properties studied as a function of *x*. Single phase films were obtained for most compositions, with the exception of films with $x \leq 0.2$, where a $Ag_3In_5Se_9$ or $AgIn_5Se_8$ ODC phase was found near the film surface. Most films showed (112) preferred orientation with crystallite sizes ranging from 80 nm to 500 nm for AIS and CIS, respectively. Substrate selection played an important role in determining grain size in the

films, with the series deposited on Mo-coated SLG showing larger grains than those deposited on bare SLG. We also showed that Na does not influence the grain size of films deposited on bare SLG for compositions of $x \leq 0.6$, when compared to films deposited on oxidized Si (100). A large deviation from Vegard's Law was also observed along the (001) crystal direction for this alloy. Direct optical band gaps were measured at 1.01 eV and 1.24 eV for CIS and AIS, respectively, with a bowing parameter of 0.224 eV. These results suggest that more attention should be placed on surface studies of $AgInSe_2$ if they are to be considered for use in heterojunction solar cell devices.

4.7 References

[1] A. Zunger, "New insights on chalcopyrites from solid-state theory," *Thin Solid Films*, vol. 515, no. 15, pp. 6160-6162, May 2007.

[2] C. Persson, Y.-J. Zhao, S. Lany, and A. Zunger, "n-type doping of $CuInSe_2$ and $CuGaSe_2$," *Physical Review B*, vol. 72, no. 3, pp. 1-14, Jul. 2005.

[3] A. Zunger, "Practical doping principles," *Applied Physics Letters*, vol. 83, no. 1, p. 57, 2003.

[4] B. Stanbery, "Copper Indium Selenides and Related Materials for Photovoltaic Devices," *Critical Reviews in Solid State and Materials Sciences*, vol. 27, no. 2, pp. 73-117, Apr. 2002.

[5] T. Begou et al., "In situ and ex situ Characterization of $(Ag,Cu)InSe_2$ Thin Films," *Conference Record 37th IEEE Photovoltaic Specialists Conference*, 2011.

[6] M. Ruckh, D. Schmid, M. Kaiser, R. Schaffler, T. Walter, and H. Schock, "Influence of substrates on the electrical properties of $Cu(In,Ga)Se_2$ thin films," *Solar Energy Materials and Solar Cells*, vol. 41-42, pp. 335-343, Jun. 1996.

[7] J. Hedstrom et al., "ZnO/CdS/Cu $(In,Ga)Se_2$ thin film solar cells with improved performance," *Proceedings of the 23rd IEEE Photovoltaic Specialists Conference*, pp. 364-371, 1993.

[8] T. Nakada, Y. Honishi, Y. Yatsushiro, and H. Nakakoba, "Impact of Sb and Bi incorporation on CIGS thin films and solar cells," *Proceedings of the 37th IEEE Photovoltaic Specialists Conference*, 2011.

[9] H. Z. Xiao, L.-C. Yang, and A. Rockett, "Structural, optical, and electrical properties of epitaxial chalcopyrite $CuIn_3Se_5$ films," *Journal of Applied Physics*, vol. 76, no. 3, p. 1503, 1994.

[10] D. Schmid and M. Ruckh, "Photoemission studies on $Cu(In,Ga)Se_2$ thin films and related binary selenides," *Applied surface science*, vol. 1337, no. 96, 1996.

[11] S. B. Zhang, S.-H. Wei, and A. Zunger, "Defect physics of the $CuInSe_2$ chalcopyrite semiconductor," *Physical Review B*, vol. 57, no. 16, pp. 9642-9656, 1998.

[12] H. Simchi, B. McCandless, W. Shafarman, K. Kim, J. Boyle, and R. Birkmire, "Surface Characterization of $(AgCu)(InGa)Se_2$ Thin Films For Solar Cells," in *37th IEEE Photovoltaics Specialist Conference*, 2011.

[13] D. Liao and A. Rockett, "Epitaxial growth of $Cu(In,Ga)Se_2$ on GaAs(110)," *Journal of Applied Physics*, vol. 91, no. 4, p. 1978, 2002.

[14] J. E. Jaffe and A. Zunger, "Defect-induced nonpolar-to-polar transition at the surface of $CuInSe_2$," *Journal of Physics and Chemistry of Solids*, vol. 64, no. 9-10, pp. 1547–1552, Sep. 2003.

[15] R. Bacewicz, J. R. Durrant, T. F. Ciszek, and S. K. Deb, "Optical and electrical properties of $Cu_xAg_{1-x}InSe_2$ and $CuIn_yGa_{1-y}Se_2$ alloys," *Ternary and Multinary Compounds. Proceedings of the 7th International Conference*, pp. 155-160, 1987.

[16] P. Scherrer, "Göttinger Nachrichten Gesell," vol. 2, no. 98, 1918.

[17] J. Tauc, R. Grigorovici, and A. Vancu, "Optical properties and electronic structure of amorphous germanium," *physica status solidi (b)*, vol. 15, no. 2, pp. 627–637, 1966.

[18] J. I. Pankove, *Optical Processes in Semiconductors*, Second Edition, Dover Publications, 2010, p. 448.

[19] J. G. Albornoz, R. Serna, and M. León, "Optical properties and electronic structure of polycrystalline $Ag_{1-x}Cu_xInSe_2$ alloys," *Journal of Applied Physics*, vol. 97, no. 10, p. 103515, May 2005.

[20] S. Ozaki and S. Adachi, "Optical properties and electronic band structure of $AgInSe_2$," *Physica Status Solidi (a)*, vol. 203, no. 11, pp. 2919-2923, Sep. 2006.

[21] P. Paul Ramesh, S. Uthanna, B. Srinivasulu Naidu, and P. Jayarama Reddy, "Optical absorption studies on single-phase polycrystalline $AglnSe_2$ thin films," *Journal of Materials Science Letters*, vol. 15, no. 2, pp. 116-119, 1996.

[22] S. Ozaki and S. Adachi, "Temperature dependence of the lowest-direct-bandgap energy in the ternary chalcopyrite semiconductor $AgInSe_2$," *Journal of Materials Science: Materials in Electronics*, vol. 18, no. 1, pp. 25-28, Mar. 2007.

[23] J. Boyle, G. Hanket, and W. Shafarman, "Optical and quantum efficiency analysis of $(Ag,Cu)(In,Ga)Se_2$ aborber layers," in *Conference Record IEEE Photovoltaic Specialists Conference*, 2009, pp. 1349-1354.

[24] A. Rockett, *The materials science of semiconductors*, vol. 11, no. 5. Springer Verlag, 2007.

[25] W. A. Harrison, *Electronic Structure and the Properties of Solids*. W. H. Freeman and Company, 1980.

[26] T. Maeda, T. Takeichi, and T. Wada, "Systematic studies on electronic structures of $CuInSe_2$ and the other chalcopyrite related compounds by first principles calculations," *Physica Status Solidi (a)*, vol. 203, no. 11, pp. 2634-2638, Sep. 2006.

4.8 Tables

Cu/(Ag+Cu)	Faceting (peak)	a (Å)	c (Å)	Grain Area (μm^2)	Cu+Ag (at.%)	In (at.%)	Se (at.%)
0	112	6.1166	11.7005	0.0714	22.27	23.16	54.56
0.21	112	6.0249	11.7631	0.1176	20.78	29.98	49.25
0.40	112	5.9509	11.7862	0.1132	24.85	25.96	49.19
0.64	112	5.8654	11.7591	0.0789	20.55	28.11	51.35
0.86	220	5.8328	11.6698	0.1667	24.23	25.60	50.17
1.0	220	5.7989	11.6215	0.3157	23.75	26.67	49.57
* at.%. EDS data taken at 15kV and fit using L peaks.							

Table 4.1. Film properties of $Cu_xAg_{1-x}InSe_2$ thin films deposited on bare soda-lime glass substrates.

Cu/(Ag+Cu)	Faceting (peak)	a (Å)	c (Å)	Grain Area (μm^2)	Cu+Ag (at.%)	In (at.%)	Se (at.%)
0	112	6.1353	11.6899	0.3221	18.94	27.59	53.47
0.24	112	6.0455	11.7149	0.4416	21.15	27.82	51.09
0.39	112	5.9475	11.7806	0.6184	**25.64**	**23.46**	50.90
0.58	112	5.8602	11.7121	0.3692	18.57	28.22	52.39
0.79	112	5.8246	11.6319	0.2546	16.49	28.11	55.40
1.0	112	5.7817	11.6372	0.2181	18.86	27.30	53.85
* at.%. EDS data taken at 15kV and fit using L peaks.							

Table 4.2. Film properties of $Cu_xAg_{1-x}InSe_2$ thin films deposited on Mo-coated soda-lime glass.

4.9 Figures

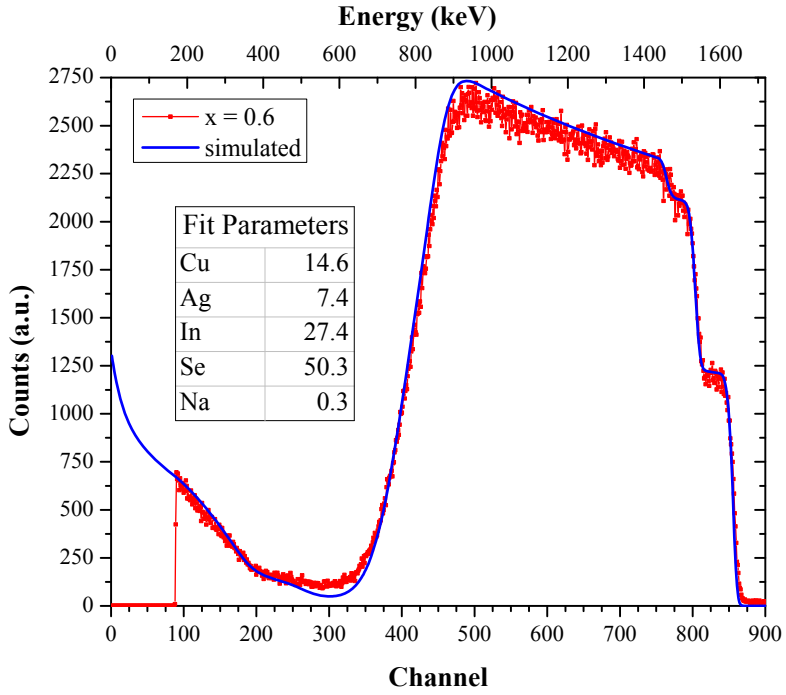

Figure 4.1. RBS spectrum and simulated pattern for film $x = 0.6$ of the bare glass series.

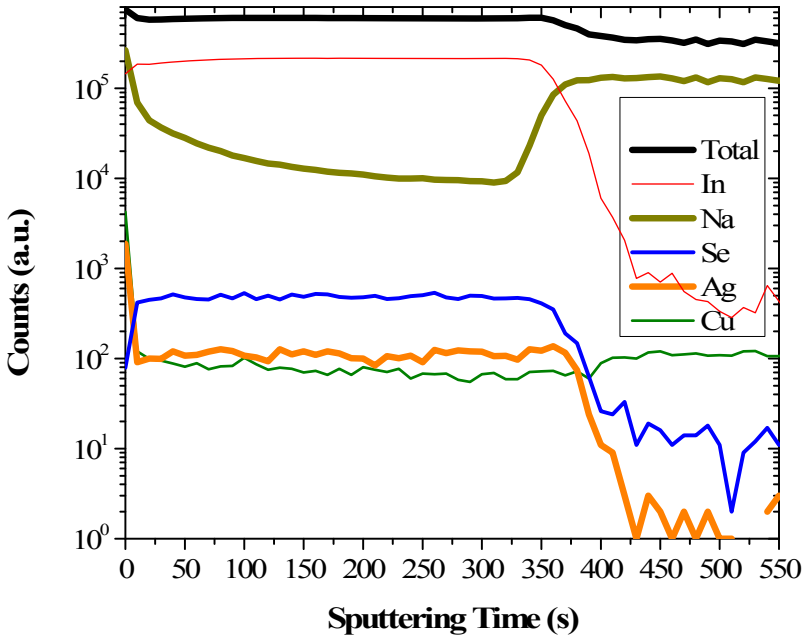

Figure 4.2. TOF-SIMS depth profile of film $x = 0.4$ from bare soda-lime glass series.

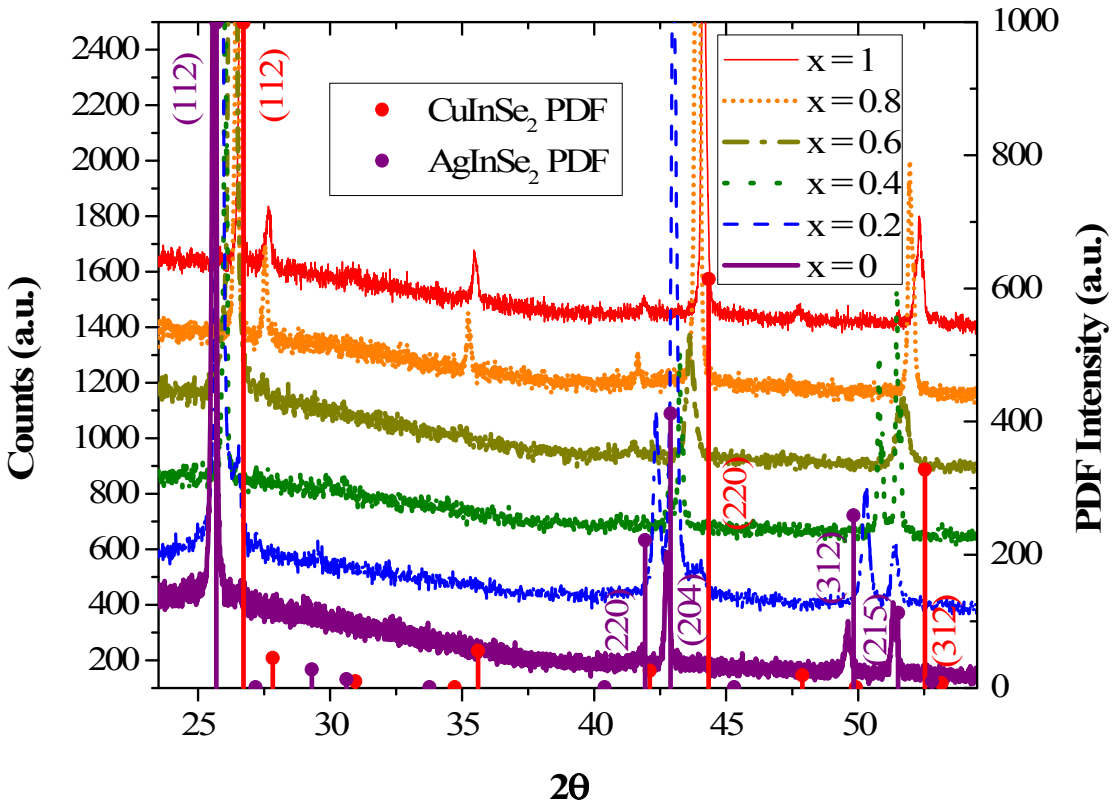

Figure 4.3. XRD ω-2θ scan of $Cu_xAg_{1-x}InSe_2$ films deposited on bare glass substrates. Single phase films were obtained for all compositions. $CuInSe_2$ (04-001-4942) and $AgInSe_2$ (04-001-4947) powder diffraction file peaks are overlaid to identify peaks in the patterns and their respective indices.

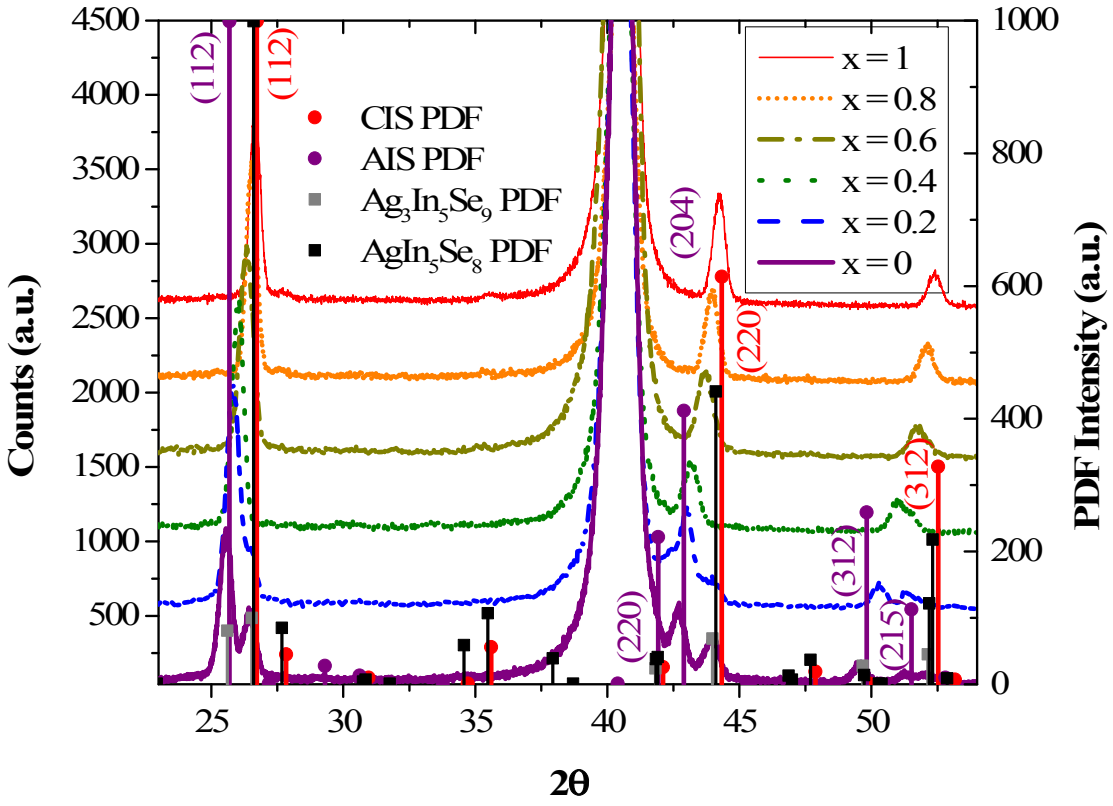

Figure 4.4. XRD ω-2θ scan of $Cu_xAg_{1-x}InSe_2$ films deposited on Mo-coated glass substrates. Single phase films were obtained for most compositions. $CuInSe_2$ (04-001-4942) and $AgInSe_2$ (04-001-4947) powder diffraction file peaks are overlaid to identify peaks in the patterns. Notice the molybdenum (100) peak at around 40.5 degrees. Films with $x \leq 0.2$ also exhibited an ordered defect compound (ODC) near the surface as confirmed via glancing incidence XRD and TOF-SIMS data.

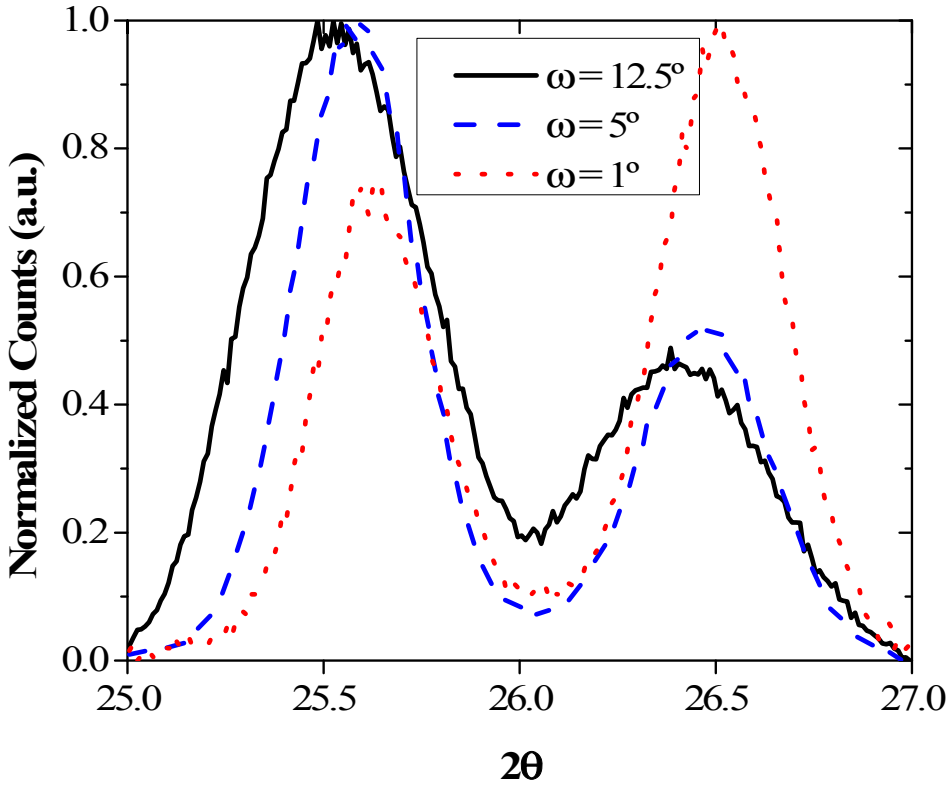

Figure 4.5. Glancing incidence XRD of (112) peak in x = 0 on Mo-coated SLG. As the angle is reduced, the satellite peak attributed to the ODC increases relative to the main (112) AIS peak, indicating the presence of the ODC near the film surface.

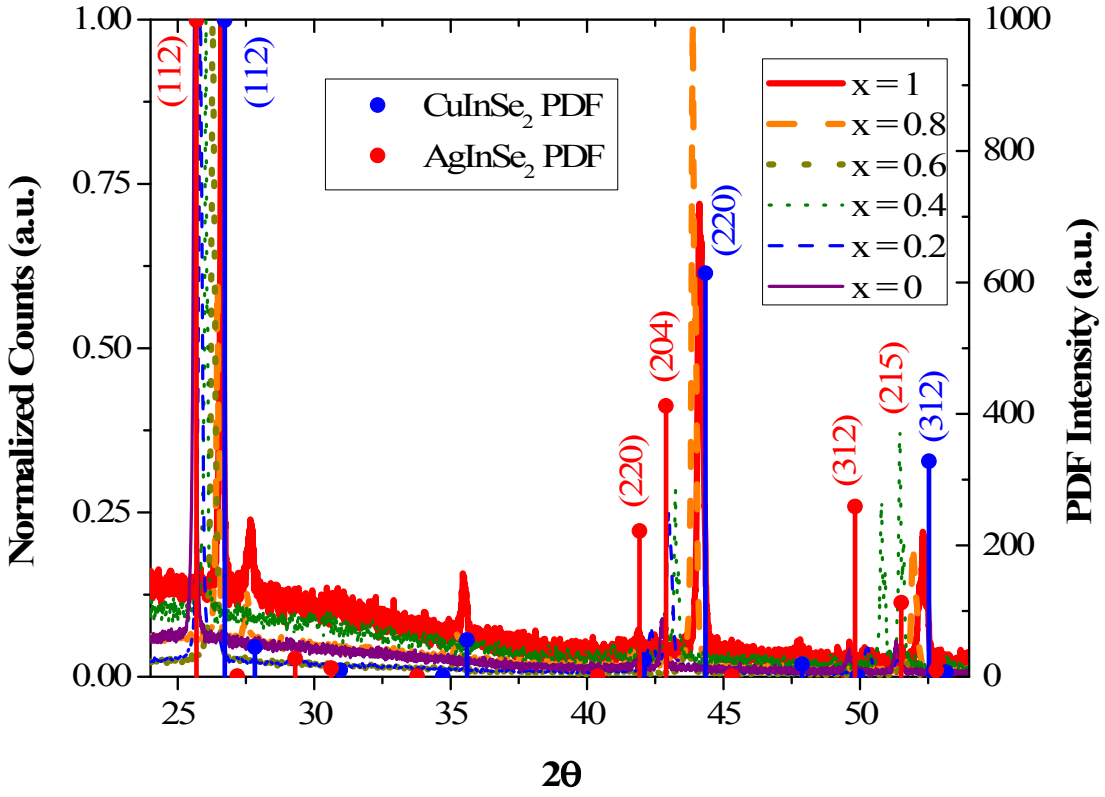

Figure 4.6. Normalized counts of the ω-2θ scan for $Cu_xAg_{1-x}InSe_2$ films on bare glass showing (112) preferred orientation for films with $x \leq 0.6$ and (220) preferred orientation for films with $x \geq 0.8$ with respect to the powder data.

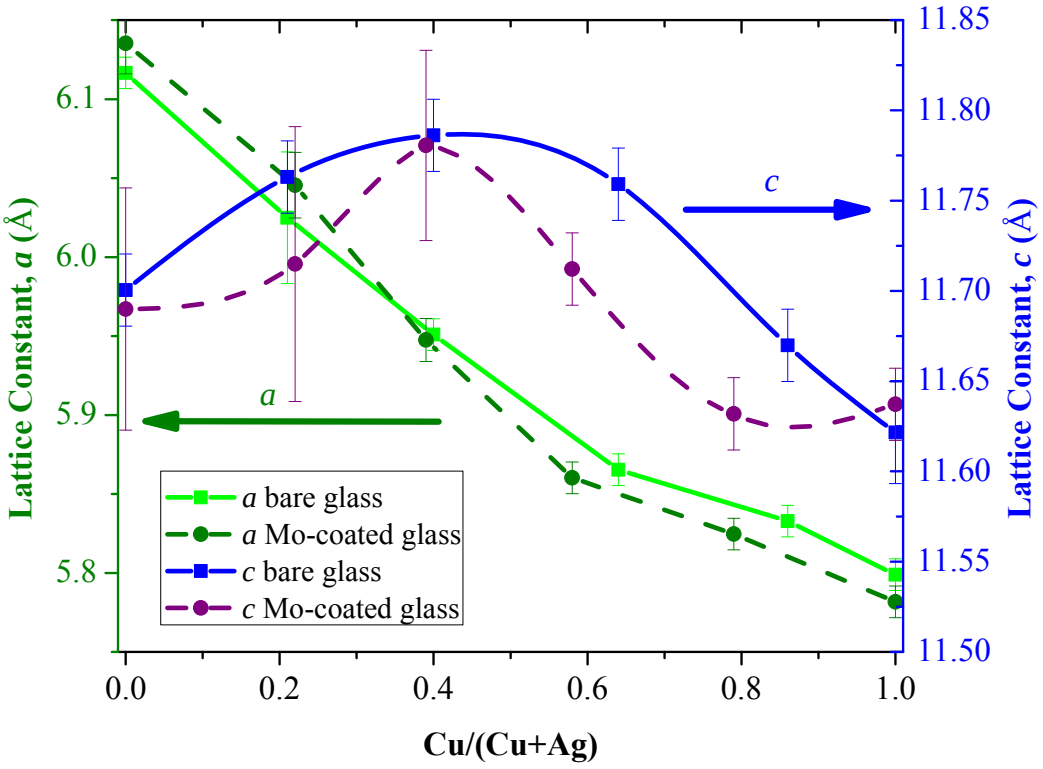

Figure 4.7. Lattice parameters *a* and *c* as a function of film composition for both bare glass and Mo-coated glass series films. Note the anomalous behavior in the lattice parameter along the (001) direction, *c*.

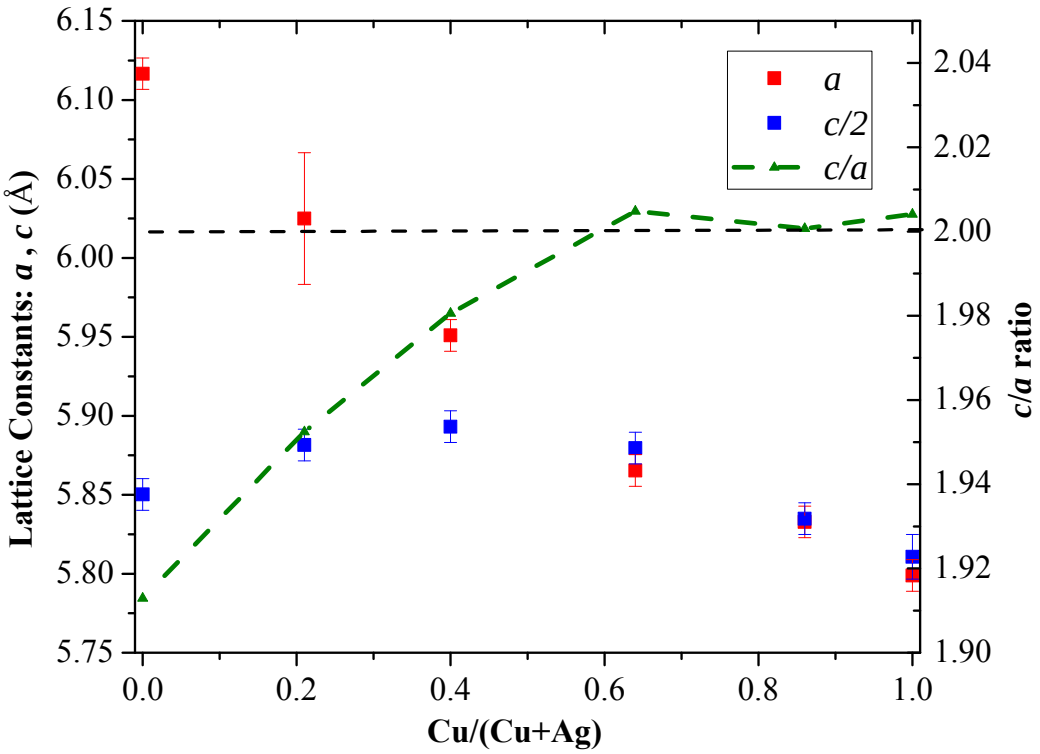

Figure 4.8. Lattice parameters of $Cu_xAg_{1-x}InSe_2$ films deposited on bare glass substrates. Notice how $c/2$ deviates from Vegard's Law severely. This leads to distortion ($c/a < 2$) along the tetragonal direction for films with $x \leq 0.4$. Films with $x \geq 0.6$ exhibit c/a ratios slightly higher than 2.

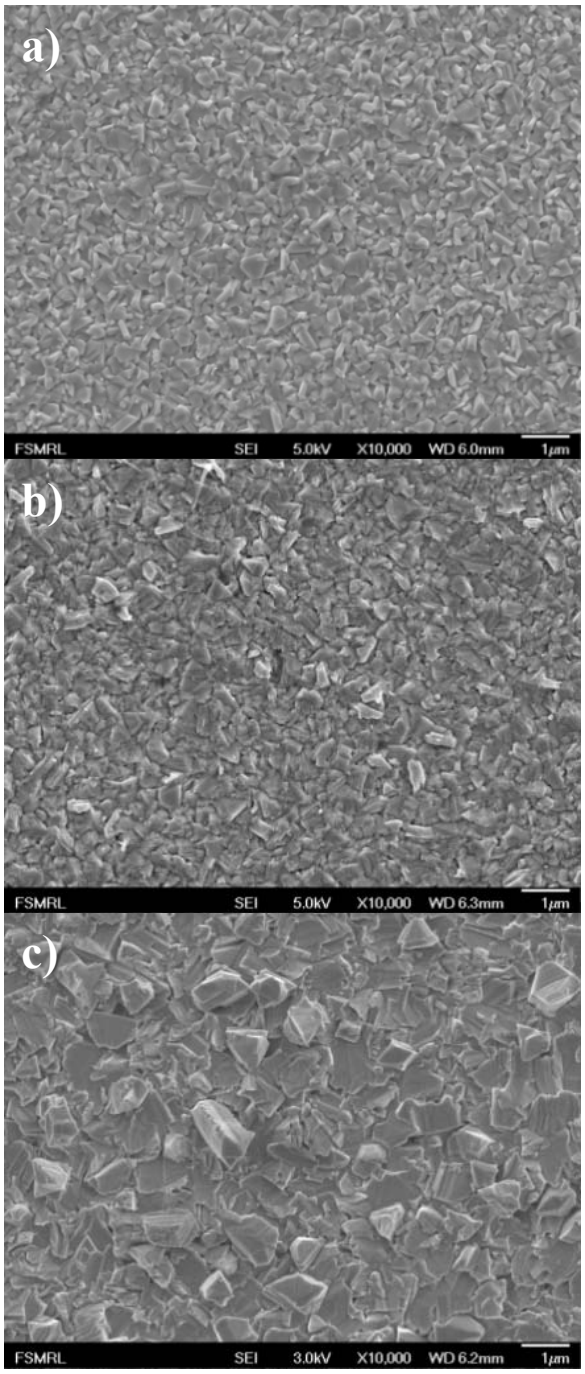

Figure 4.9. Planview SEM images of films a) $x = 0$, b) $x = 0.6$, and c) $x = 1$ for the $Cu_xAg_{1-x}InSe_2$ series on bare glass.

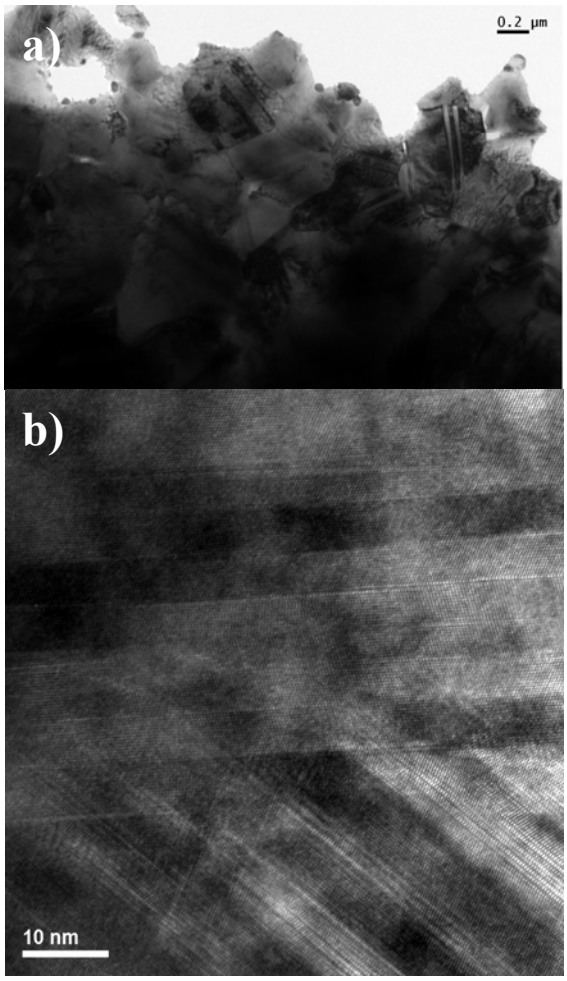

Figure 4.10. a) Low magnification and b) high magnification planview TEM of CAIS film with $x = 0.6$.

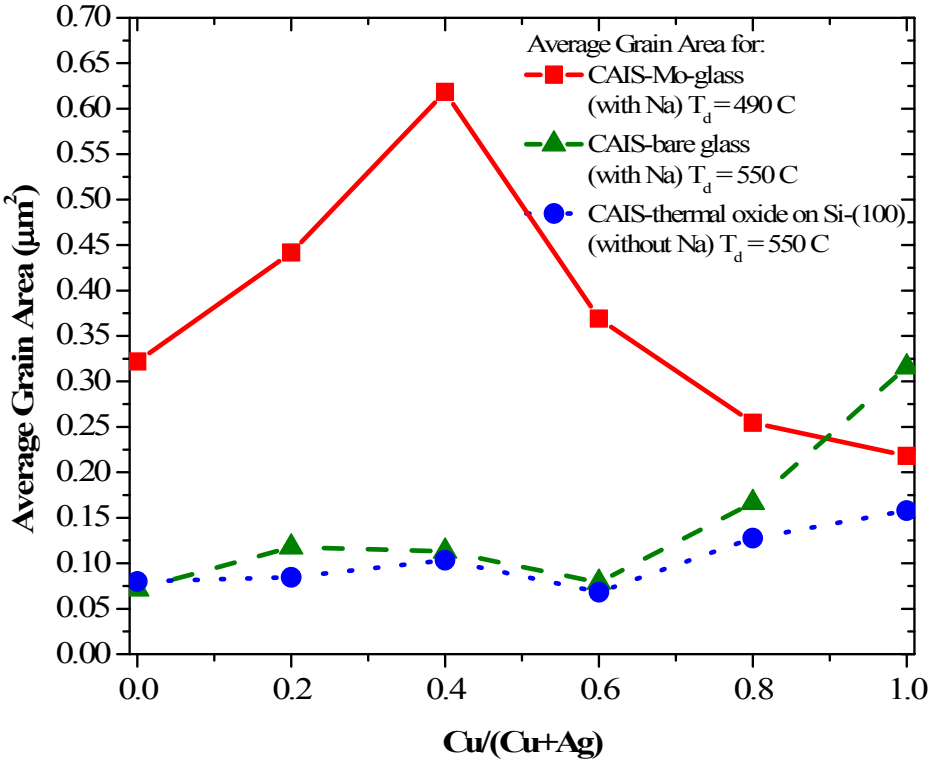

Figure 4.11. Average grain area for films deposited on bare SLG.

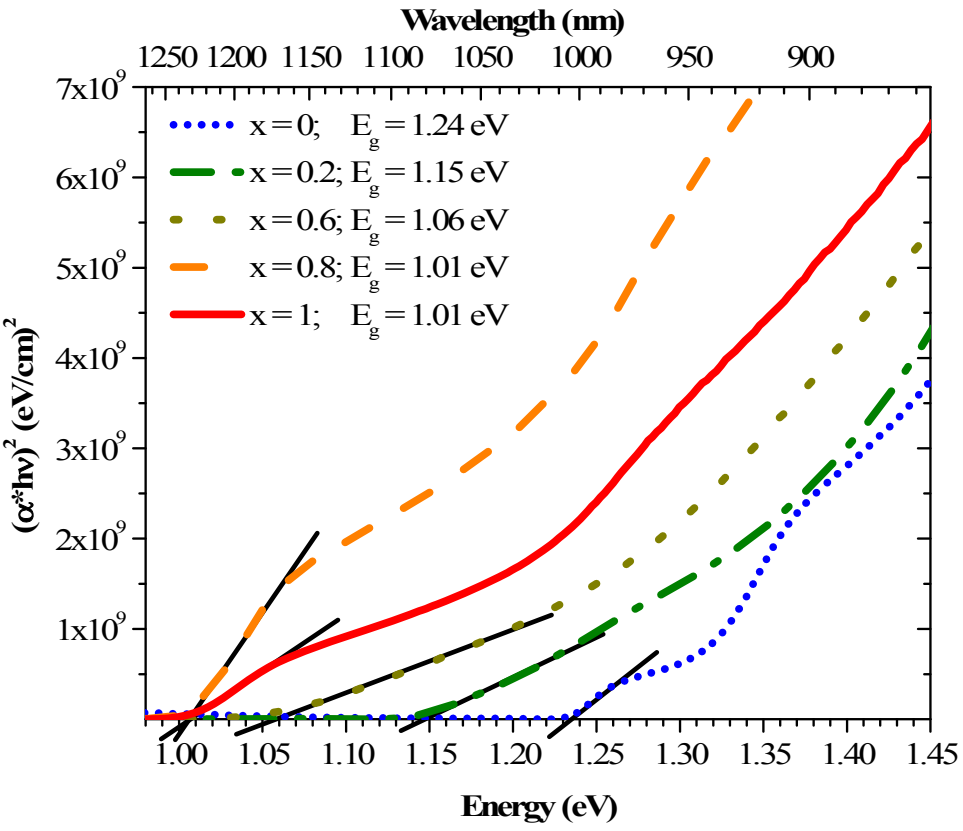

Figure 4.12. Tauc plot used for optical band gap extraction.

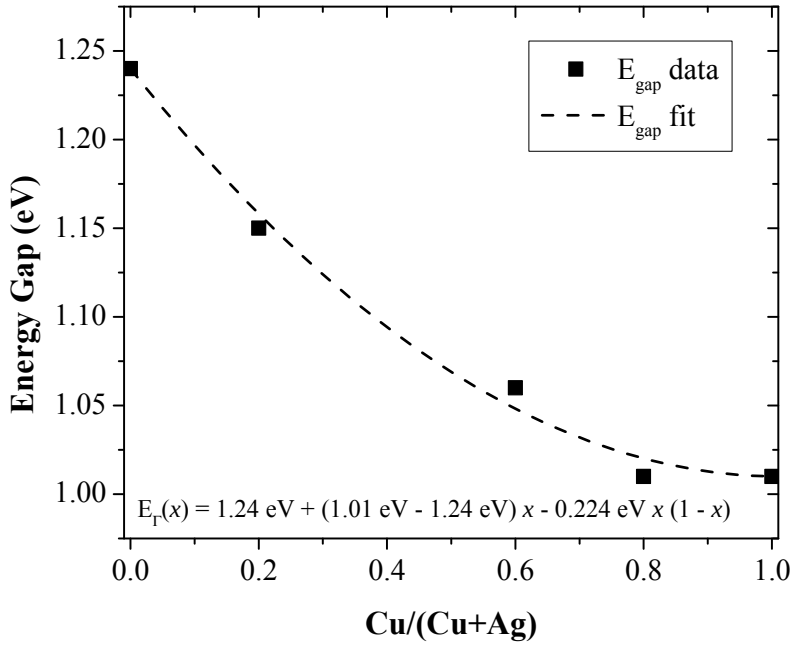

Figure 4.13. Optical band gap as a function of Cu/(Cu+Ag). The band gap fit is plotted with dashed lines.

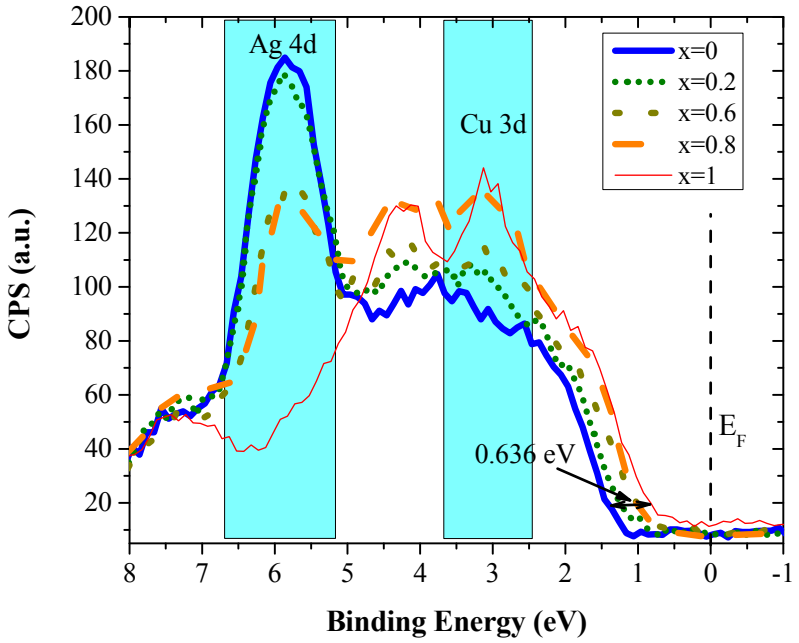

Figure 4.14. Valence levels from XPS data. The contribution of the Se 4*p* orbital will vary based on the Cu/(Cu+Ag) content as described by Maeda *et al.* [26]. This is due to the *p-d* repulsion between Cu/Ag and Se.

CHAPTER 5

IDENTIFICATION OF RADIATIVE DEFECTS IN $Cu_xAg_{1-x}InSe_2$ THIN FILMS

In this chapter radiative defects in polycrystalline $Cu_xAg_{1-x}InSe_2$ thin films are studied via photoluminescence (PL) spectroscopy. Optical transitions were identified for the films and their behaviors were studied as a function of excitation power, sample temperature, and film composition. Results are presented in section 5.2, followed by discussion of the results in section 5.3, and concluding remarks in section 5.4. Additional data of the results discussed in this chapter can be found in Appendix A of this dissertation.

5.1 Introduction

The effect that Ag alloying has on defects and optoelectronic properties of $CuInSe_2$ is still not completely understood. Only two studies [1-2] have looked at the effects that Ag alloying has on the defect levels in $Cu_xAg_{1-x}InSe_2$. However those studies do not go into the details of defect behavior. The identification and behavior of these levels is crucial to engineering high efficiency, thin-film chalcogenide solar cells. Providing a blueprint of the defect levels in the alloy could lead to the improvement of solar cell devices through defect engineering.

5.2 Results

Identification of defects in the films was carried out using photoluminescence (PL) spectroscopy as described in Chapter 3.6. The samples were mounted to a cold stage, loaded into a Janis Research liquid He-bath cryostat, and cooled to 4 K. Films

were excited using a frequency-doubled Lightwave Nd:YAG laser (λ = 532 nm) with a beam size of ~200 μm for power- and temperature-dependent studies. A complete instrument response function (including gratings, filters, lenses, and the detector) was used to correct the data for system sensitivity. Despite these efforts, artifacts were seen around 0.89 eV in all spectra, possibly due to water vapor, whose absorption varies between measurements of the instrument response function and the samples.

All films grown were group-I deficient (slightly In-rich) as seen in Table 5.1. Room-temperature ellipsometry and optical transmission and reflection data were used to determine the optical band gap of the films, as described in Chapter 4.5 [3]. The values for each film are given in Table 5.2 and are in agreement with those reported by Albornoz *et al.* [4].

Representative power- and temperature-dependent PL spectra are shown in Figures 5.1 and 5.2, respectively, for the $AgInSe_2$ ($x = 0$) sample. Best fits for the spectra were obtained with two Gaussian peaks; one at 1.168 eV and another at 1.230 eV (values at 10 K and 10 mW). Two exponential band tails were also observed at low emission energies. The luminescence spectra from the film with $x = 0.2$ were very similar to the $AgInSe_2$ spectra, and were fit with two main peaks at 1.025 eV and 1.084 eV and an exponentially decaying tail at low energies. This trend of two main peaks and an exponentially decaying low energy tail held true for all films with $x \leq 0.6$ (see Figure 5.3). For $x \geq 0.8$, three peaks were required to obtain a best fit. These were located at energies of 0.790 eV, 0.868 eV, and 0.943 eV for the $x = 1$ film. Values of the fit peak positions for all samples can be found in Table 5.2.

The behavior of these peaks as a function of power and temperature can yield enough information about their associated transitions to allow us to estimate the type of transition responsible and the defect levels involved. Specific radiative transitions [band-to-band (BB), donor-acceptor pair (DAP), free-to-bound (FB)] are found at characteristic energies relative to the bandgap and also have different dependences on the excitation power. Schmidt *et al.* [5] conducted a detailed study of the dependence of peak intensity on excitation power and found that it follows a power law behavior:

$$I_{PL} = A * P_{exc}^{\ k} \tag{5.1}$$

They observed that excitonic transitions exhibit $1 < k < 2$, while DAP and FB transitions show $k < 1$. Peak intensity vs. excitation power plots can be seen in Figure 5.4 for peaks of the $x = 0$, $x = 0.6$ and $x = 1$ films. From these plots, the exponent in the power law behavior described by Schmidt can be extracted using Equation 5.1. The k values for all main peaks can be found in Table 5.2.

A peak shift, or lack thereof, with increasing excitation intensity is also an indication of the type of transition. DAP transitions undergo a blue-shift upon increasing excitation intensity due to an increase in the Coulombic binding energy with decreasing separation between the pairs. Therefore a transition due to a DAP will have a characteristic energy:

$$E_{DAP} = E_{gap} - (E_a + E_d) + {}^{q^2}/_{\varepsilon r} \tag{5.2}$$

where E_{DAP} is the energy of the DAP emission, E_{gap} is the optical bandgap, $E_{a(d)}$ is the acceptor (donor) state energy relative to the appropriate band edge, and $q^2/\varepsilon r$ is the Coulombic binding energy between the donor and acceptor. This shift was quantified by fitting the peak position as a function of excitation power with the following equation:

$$E_{DAP}(I_{ex}) = E_{DAP}(I_0) + \beta \log_{10}(I_{ex}/I_0) \quad (5.3)$$

where β is the blueshift measured in meV/decade (see Table 5.2). FB and BB transitions typically do not show a shift with increasing excitation power in a material unless it is heavily compensated, in which case local potential fluctuations in the band edge will be "flattened" as excitation power increases, giving rise to a blueshift in the peak. This phenomenon is explained in detail by Siebentritt *et al.* in various publications [6-7] and book chapters [8], and was observed in film with x = 0.6. Therefore, the value of β reported for this film will include both the DAP shift and the shift due to heavily compensated material.

Temperature-dependent measurements allowed for determination of the position of a defect level involved in a DAP transition with respect to its band edge. Transitions were modeled using a double-activation energy formula in which one characteristic energy and hence process dominates quenching at low temperatures and another dominates at higher temperatures [9-10]:

$$I_{PL}(T) = \frac{I_0}{1+D_1 exp(-E_1/k_B T)+D_2 exp(-E_2/k_B T)} \quad (5.4)$$

where E_1 and E_2 are the activation energies, and D_1 and D_2 are the corresponding pre-exponentials that determine the transition temperature between the two quenching rates.

Figure 5.5 shows quenching plots for the peaks of the $AgInSe_2$ and $CuInSe_2$ samples and Table 5.2 lists the resulting activation energies. Typically, when using the double activation energy quenching model for a DAP transition, one of the energies is the binding energy of the donor level while the other is that of the acceptor level. However, in our case one of the energies appears too small to be a defect level (~5 meV). Such low activation energy could be associated either with a tail in the defect states or with small

changes in the dominant population of charges in a defect band as the temperature changes. However, because no band tail is involved in a DAP transition, the low activation energy is presumably due to population changes within the defect band. This low activation energy was observed in all samples, with values in the range 4-8 meV, and no apparent trend as a function of sample composition.

By knowing (*i*) the value of the optical bandgap, measured by optical absorption; (*ii*) the energy of the transition, observed by PL; and (*iii*) the energy of one defect within the band, calculated from the quenching plots; it was possible to calculate the energy level of the second defect level associated with a DAP transition by using Equation 5.2. The temperature-dependent spectra were acquired at high excitation powers (power at which the DAP peak stopped blue shifting), so the reported peak position is a combination of the actual DAP defect level, E_{DAP}, plus the Coulomb interaction term, $q^2/\varepsilon r$. However, an estimate of the optical band gap at 10 K is needed for this calculation. The temperature dependence of the band gap has been studied in the past for both the $AgInSe_2$ and $CuInSe_2$ compounds [11-18]. The change in the band gap from 300 K to approximately 10 K for $CuInSe_2$ has been reported as ~ +30 meV. A much smaller change of ~ +10 meV has been reported for $AgInSe_2$. The band gap change for the alloyed film compositions was interpolated based on these published results for the compounds. The conclusions of the current work are not strongly affected by errors in the estimated optical gaps, especially if the error is in the same direction for all alloys studied.

Following is an example of the calculation of the second defect level in a DAP transition. In the case of $CuInSe_2$, the optical band gap at 10 K was estimated to be 1.036

eV. Three peaks were determined by fitting and the results indicate that the transitions were DAP type. The larger activation energies were 60 meV for all three peaks from the quenching plot analysis. This means that all three peaks share a common defect level. By plugging these values into Equation 5.2 and solving for E_a (assuming E_d is the extracted defect level from the quenching model) we can calculate the position of the second defect level in a DAP transition. In the case of $CuInSe_2$, acceptor levels were calculated from the DAP transitions at 186 meV, 108 meV, and 33 meV for the 0.790 eV, 0.868 eV, and 0.943 eV transitions, respectively. These defect levels are consistent with typical values observed for multiple acceptor levels in $CuInSe_2$, so the assignment of the 60 meV level to a donor is reasonable. This same approach was followed for all films and their calculated defect levels can be found in Table 5.2.

Several factors contribute to possible errors in the expected defect energies. The fit peaks have significant widths. For the $AgInSe_2$ peaks the typical FWHM is ~50 meV. The $CuInSe_2$ exhibits wider peaks with ~90 meV FWHM values. The expected errors in the fit energies from the quenching curves are accurate to within ~ ±10 meV. The estimated optical energy gap should be correct to within ±10 meV. Taking the various sources of error together, each energy level should be accurate to within ±20 meV for the donor and ±30 meV for the acceptor. We note that the acceptor and donor levels observed by methods such as temperature dependent Hall effect, temperature-dependent device performance, and other techniques typically vary by this amount or more.

The PL at fixed power (10 mW) and temperature (10 K) showed the highest peak for the $x = 0$ film, which decreased with increasing Cu content up to $x = 0.8$, as seen in Figure 5.6. The PL peak intensity for the $CuInSe_2$ film was comparable to that of the $x =$

0.2 film and somewhat below the pure $AgInSe_2$ film. A high PL intensity is typically indicative of higher material quality [19].

Very Ag-dominant samples ($x \leq 0.4$) showed the sharpest peaks with full-width-at-half-maximum (FWHM) values of 47 meV and 38 meV for the main transitions in films $x = 0$ and $x = 0.4$, respectively. Cu-dominant films have much broader peaks than the Ag-dominant films, with FWHM values within the range 60-94 meV. One exception to this behavior was the Ag-dominant film with $x = 0.2$, which showed peak widths similar to those of Cu-dominant films. This film also exhibited an ordered defect compound (ODC) near the films surface, as explained in Chapter 4. The presence of this additional phase could lead to broadening of the peaks. FWHM values for the other peaks are found in Table 5.2. The narrower peaks observed in Ag-dominant films suggest that there is less disorder around the defect states responsible for these transitions.

All samples exhibited exponentially decaying tails at low emission energies. These were fit using the following expression [6]:

$$I_{PL} = A * e^{\left(-\frac{E-E_0}{\gamma}\right)} \tag{5.5}$$

where γ is the characteristic tail energy. The values of γ can be found in Table 5.2 and did not follow any trend with composition. However, the low energy part of the spectrum was more tail-like for $x \leq 0.6$ and more defect-like for $x \geq 0.8$, meaning that films with $x \leq 0.6$ (tail-like) show more of an exponentially decaying behavior like the one in Equation 5.4, while films with $x \geq 0.8$ (defect-like) show a more Gaussian behavior and a very short tail-like component. Films with $x = 0$ and $x = 0.4$ showed a second exponential tail at lower emission energies. In the case of the Ag-dominant films,

these exponentially decaying tails extended deep into the forbidden gap, reaching values as low as 0.74 eV. A continuum of defects this deep into the gap could promote recombination and might be one of the reasons Ag-based devices have not performed as well as CIGS devices.

5.3 Discussion

By taking into consideration the k values of the peaks, their shift with excitation power and temperature, and the calculated energy levels, we can assign a transition type (BB, FB, DAP) to each peak (see Table 5.2). If a peak showed a $k \leq 1$, a blueshift with increasing excitation power, and $E_{PL} + E_d < E_{gap}$, then a DAP assignment was made. Peaks with a position close to the band edge, lack of blue shift, and a single defect level were assigned as FB transitions. All films exhibited DAP transitions. FB transitions were also found for the Ag-dominant films ($x \leq 0.4$). Taking all of the data together, we propose a defect level schematic of $Cu_xAg_{1-x}InSe_2$ thin films as shown in Figure 5.7.

Three consistent transitions were identified in films with $x \geq 0.8$, while only two were identified in films with $x \leq 0.6$. Films with $x \geq 0.6$ also shared nearly identical transitions, as seen by the presence of peaks close to 0.80 eV, 0.88 eV, and 0.95 eV (the 0.80 eV peak is missing in the $x = 0.6$ film).

The energy level of donor defects in $Cu_xAg_{1-x}InSe_2$ films seemed to follow a U-shaped behavior with respect to composition (see Figure 5.8), with the alloyed film $x = 0.6$ having the lowest activation energy (25 meV) and $CuInSe_2$ having the largest one (60 meV). A lower activation energy in an alloy film is expected due to alloy disorder broadening both the defect state energy and the band edges. The data suggest the

presence of two main donor levels at ~20-30 meV shared by the x = 0.8, 0.6, 0.4, and 0 films; and another level at ~60 meV in the x = 1.0, 0.2, and 0 films. However, due to the width of the peaks and the uncertainty in measuring and fitting the spectra, it is very likely that these are the same donor level, broadened or otherwise affected by the alloy disorder. This is consistent with the lower energy being found in the mid range of compositions. Three acceptor levels were identified in the films. The shallowest acceptor level was at 20 meV and only present in the $AgInSe_2$ film. A related shallow level was found at 35 meV and present in the x = 1.0 and 0.8 films. We were not able to identify any acceptors this shallow for films that were severely group-I deficient, as was the case for samples with x = 0.2 and x = 0.6. The second acceptor level was found at 70-80 meV from the valence band for two films (x = 0.4 and 0.2) and at 100-110 meV from the valence band in three films (x = 1.0, 0.8, and 0.6). The third and deepest acceptor level was calculated at approximately 170-190 meV from the valence band and was present in films x = 1.0, 0.8, and 0.6.

Based on previous assignment of defects in $CuInSe_2$ and $AgInSe_2$ we suggest the following assignment of defect levels in $Cu_xAg_{1-x}InSe_2$. Sample composition and estimated formation energies of the point defects [20-22] were taken into consideration. However, these assignments are speculative, since no real effort was made at confirming these defects via techniques such as optically detected magnetic resonance. The 20-60 meV donor is likely due to In atoms on group I site or Se vacancies [23-25]. A factor favoring V_{Se} is that Se is common for all films while Ag and Cu are not.

The shallowest acceptor level (~ 20-40 meV) was assigned to group I vacancies. Hjelt *et al.* [26] identified this level as a V_{Ag} in $AgInSe_2$ and it agrees with the 20-40 meV

acceptor associated with V_{Cu} for $CuInSe_2$ films [20, 25]. The two deeper levels at 70-100 and 170-190 meV are most likely associated with group I on group III antisite defects and probably represent the single and double charge states of this divalent defect. Both of these defects have been observed previously in $CuInSe_2$. The absence of both states in the $AgInSe_2$ suggests that this material is better ordered. Disorder on the cation sublattice is expected due to the relatively low chalcopyrite-to-sphalerite transition temperature in $CuInSe_2$. The absence of the I_{III} antisite in $AgInSe_2$ may be the result of a stronger cation ordering and hence to fewer minority antisites. Generally better order and crystal perfection is also implied by the sharper peak in the $x = 0$ and $x = 0.4$ films. We note that the III-rich stoichiometry does not favor I_{III} defects and so they would only be expected to form due to disorder in the cation sublattice and not as intrinsic results of stoichiometry.

Transitions and estimated defect energies for films $x \geq 0.6$ are very similar, suggesting very little change in the defects in this compositional range. This agrees well with what has been reported before for the $CuInSe_2$ and $AgInSe_2$ compounds [20-26]. Overall, specific defect levels did not change position relative to their respective band edges. This suggests that the defect states are derived from the Bloch states of the solid and therefore from the band edges rather than being highly localized on defects. This would promote formation of defect bands, as observed in $CuInSe_2$, and would favor transport of the relatively delocalized charges trapped in the defect states.

While it appears from all of these considerations that the low x (Ag-dominant) alloys, and $AgInSe_2$ in particular, have fewer point defects and should yield better devices, this is discounted by the presence of exceptionally wide exponential tails in the

Ag-dominant materials. These suggest a continuum of defects ranging far into the gap. We cannot assign these defects to specific causes but it appears the local chemical environments alter the energy of native point defects in the Ag-dominant materials over a wide range of values. This does not occur to the same extent in Cu-dominant compounds. Therefore it seems likely that the relatively lower performance of the Ag-dominant alloys and $AgInSe_2$ may be due to these defects. Cohen *et al.* have proposed previously that band tails are critical determinants of device performance [27]. The results for $AgInSe_2$ alloys suggest that this is even more important in these materials.

5.4 Conclusions

The defect levels of $Cu_xAg_{1-x}InSe_2$ thin films have been studied via photoluminescence spectroscopy experiments. Two donor levels (20-30 meV and 60 meV) and three acceptor levels (20-35 meV, 70-100 meV, and 170-190 meV) were identified in the films. Most transitions were assigned to DAPs based on their power dependence. Donor activation energies followed a U-shape behavior as a function of composition. Specific defect levels did not change position relative to their respective band edges, suggesting that the defect states are derived from the Bloch states of the solid rather than being highly localized on defects. The $AgInSe_2$ film had the highest PL intensity and also exhibited a peculiar PL signal. The primary emission (1.168 eV) exponentially tails off into the bandgap until another exponentially decaying tail takes over at around 1.05 eV. This second tail continues deep into the bandgap, beyond the range of our detector. Most Ag-dominant films ($x = 0$ and $x = 0.4$) showed a similar double exponentially decaying tail into the gap. A continuum of defects this deep into

the gap could hinder carrier collection, significantly reducing the efficiency of a solar cell fabricated from $AgInSe_2$ or Ag-dominant $Cu_xAg_{1-x}InSe_2$ absorber layers.

5.5 References

[1] T. F. Ciszek, R. Bacewicz, D. Dunlavy, S. K. Deb, and J. R. Durrant, "Crystal growth and photoelectrical properties of $Cu_xAg_{1-x}InSe_2$ and $CuIn_yGa_{1-y}Se_2$ solid solutions," *19th IEEE Photovoltaic Specialists Conference*, pp. 1448-1453, 1987.

[2] A. R. Aquino, S. A. Little, S. Marsillac, R. W. Collins, and A. A. Rockett, "Identification of Defect Levels in $Cu_xAg_{1-x}InSe_2$ Thin Films via Photoluminescence," *Proceedings of the 37th IEEE Photovoltaic Specialists Conference*, 2011.

[3] T. Begou et al., "In situ and ex situ Characterization of $(Ag,Cu)InSe_2$ Thin Films," *Conference Record 37th IEEE Photovoltaic Specialists Conference*, 2011.

[4] J. G. Albornoz, R. Serna, and M. León, "Optical properties and electronic structure of polycrystalline $Ag_{1-x}Cu_xInSe_2$ alloys," *Journal of Applied Physics*, vol. 97, no. 10, p. 103515, May 2005.

[5] T. Schmidt, K. Lischka, and W. Zulehner, "Excitation-power dependence of the near-band-edge photoluminescence of semiconductors," *Physical Review B*, vol. 45, no. 16, pp. 8989–8994, Feb. 1992.

[6] S. Siebentritt, N. Papathanasiou, and M. Luxsteiner, "Potential fluctuations in compensated chalcopyrites," *Physica B: Condensed Matter*, vol. 376-377, pp. 831-833, Apr. 2006.

[7] S. Siebentritt, N. Papathanasiou, and M. Lux-Steiner, "Photoluminescence excitation spectroscopy of highly compensated $CuGaSe_2$," *Physica Status Solidi (B)*, vol. 242, no. 13, pp. 2627-2632, Nov. 2005.

[8] S. Siebentritt and U. Rau, *Wide-gap chalcopyrites*, vol. 403. Springer-Verlag, 2006, p. 257.

[9] W. Stadler et al., "Optical investigations of defects in $Cd_{1-x}Zn_xTe$," *Physical review. B, Condensed matter*, vol. 51, no. 16, pp. 10619-10630, Apr. 1995.

[10] D. Grecu, A. D. Compaan, D. Young, U. Jayamaha, and D. H. Rose, "Photoluminescence of Cu-doped CdTe and related stability issues in CdS/CdTe solar cells," *Journal of Applied Physics*, vol. 88, no. 5, p. 2490, 2000.

[11] S. Ozaki and S. Adachi, "Temperature dependence of the lowest-direct-bandgap energy in the ternary chalcopyrite semiconductor $AgInSe_2$," *Journal of Materials Science: Materials in Electronics*, vol. 18, no. 1, pp. 25-28, Mar. 2007.

[12] V. Aliyev, G. Guseinov, F. Mamedov, and L. Chapanova, "Anomalous temperature dependence of the band gap in $AgGaSe_2$ and $AgInSe_2$," *Solid state communications*, vol. 59, no. 11, pp. 745–746, 1986.

[13] C. Rincón, E. Hernández, S. Wasim, and I. Molina, "Temperature dependence of the fundamental absorption edge in p-type $CuInSe_2$," *Journal of Physics and Chemistry of Solids*, vol. 59, no. 6-7, pp. 1015–1019, 1998.

[14] A. Rockett and R. W. Birkmire, "$CuInSe_2$ for photovoltaic applications," *Journal of Applied Physics*, vol. 70, no. 7, p. R81, 1991.

[15] B. Stanbery, "Copper Indium Selenides and Related Materials for Photovoltaic Devices," *Critical Reviews in Solid State and Materials Sciences*, vol. 27, no. 2, pp. 73-117, Apr. 2002.

[16] H. Neumann, "Optical properties and electronic band structure of $CuInSe_2$," *Solar cells*, vol. 16, pp. 317–333, 1986.

[17] G. Chapman, J. Shewchun, B. Garside, J. Loferski, and R. Beaulieu, "$Cu_{1-y}Ag_yInS_{2(1-x)}Se_{2x}$ as a prototype of the pentanary chalcopyrite semiconductor system for solar photovoltaic cells," *Solar Energy Materials*, vol. 1, no. 5-6. pp. 451-469, Jun-1979.

[18] G. Chapman, J. Shewchun, J. Loferski, B. Garside, and R. Beaulieu, "Lattice constants and band-gap variations of the pentenary semiconductor system $Cu_{1-y}Ag_yInS_{2(1-x)}Se_{2x}$," *Applied Physics Letters*, vol. 34, no. 11, pp. 735–737, 1979.

[19] S. Shirakata and T. Nakada, "Photoluminescence and time-resolved photoluminescence in $Cu(In,Ga)Se_2$ thin films and solar cells," *Physica Status Solidi (C)*, vol. 6, no. 5, pp. 1059-1062, May 2009.

[20] A. Rockett and R. W. Birkmire, "$CuInSe_2$ for photovoltaic applications," *Journal of Applied Physics*, vol. 70, no. 7, p. R81, 1991.

[21] S. Wasim, "Transport properties of $CuInSe_2$," *Solar Cells*, vol. 16, pp. 289–316, 1986.

[22] S. B. Zhang, S.-H. Wei, and A. Zunger, "Defect physics of the $CuInSe_2$ chalcopyrite semiconductor," *Physical Review B*, vol. 57, no. 16, pp. 9642-9656, 1998.

[23] K. Kishigui, K. Abe, G. Murakami, Y. Shim, K. Yoshino, and K. Wakita, "Study of steady-state photoluminescence of $AgInSe_2$ crystals," *Thin Solid Films*, vol. 517, no. 4, pp. 1445-1448, Dec. 2008.

[24] M. S. Al-Kotb, W. Puff, S. A. Hassan, and M. Mohsen, "A Study of Vacancy-Like Defects in the Chalcopyrite Semiconductor $AgInSe_2$," *Materials Science Forum*, vol. 363-365, pp. 150-152, 2001.

[25] F. Abouelfotouh, H. Moutinho, A. Bakry, T. Coutts, and L. Kazmerski, "Characterization of the defect levels in copper indium diselenide," *Solar Cells*, vol. 30, no. 1-4, pp. 151-160, May 1991.

[26] K. Hjelt and J. Krustok, "Photoluminescence of $AgInSe_2$," *Ternary and Multinary Compounds. Proceedings of the 11th International Conference*, pp. 441-444, 1998.

[27] J. T. Heath, J. D. Cohen, W. N. Shafarman, D. X. Liao, and A. A. Rockett, "Effect of Ga content on defect states in $CuIn_{1-x}Ga_xSe_2$ photovoltaic devices," *Applied Physics Letters*, vol. 80, no. 24, p. 4540, 2002.

5.6 Tables

Cu/(Ag+Cu)	Cu	Ag	In	Se	Cu/(Cu+Ag)	(Cu+Ag)/In	(I+III)/VI
0	0	22.27	23.16	54.57	0	0.96	0.83
0.2	4.28	16.50	29.98	49.24	0.21	0.69	1.03
0.4	9.88	14.97	25.96	49.19	0.40	0.96	1.03
0.6	13.19	7.36	28.11	51.34	0.64	0.73	0.95
0.8	20.77	3.46	25.60	50.17	0.85	0.95	0.99
1.0	23.75	0.00	26.67	49.58	1	0.89	1.02
* at.%. EDS data taken at 15kV and fit using L peaks. Na values range from 0.01%-0.2%.							

Table 5.1. Film composition.

Cu/(Ag+Cu)	0		0.2		0.4		0.6		0.8		1	
E_{gap} (eV)	1.235		1.148		1.092		1.058		1.003		1.006	
E_{gap} 10K (estimate)	1.245		1.162		1.110		1.080		1.029		1.036	
E_{PL} (eV)	1.168	1.230	1.025	1.084	1.005	1.048	0.887	0.956	0.820	0.886	0.961	0.790	0.868	0.943
E_a (meV)	24/5	20	80/7	80/5	30/4	34/8	25/5	25/5	30/5	30/5	30/4	60/7	60/5	60/4
E_{calc} (meV)	57	--	57	--	73	30	168	99	179	113	38	186	108	33
β (meV/dec.)	8	NA	~ 0	~ 0	4	NA	18	14	NA	7	5	6	8	3
k	0.79	NA	0.89	0.99	0.88	NA	0.87	0.89	NA	0.89	1.03	0.82	0.89	0.98
Transition	DAP	FB	DAP	FB	DAP	FB	DAP	DAP	DAP	DAP	DAP	DAP	DAP	DAP
FWHM (meV)	47	56	73	66	38	68	78	94	89	94	59	73	94	73
γ (meV)	25/260		46		18/150		20		33		28			

Table 5.2. Optical bandgaps and transitions for $Cu_xAg_{1-x}InSe_2$ thin films. E_a is the defect level extracted from the quenching model (Equation 5.4). E_{calc} is the defect level calculated using Equation 2. β represents the amount of blueshift with increasing excitation power. NA indicates that not enough data were collected to obtain the respective values. γ is the characteristic band tail energy. The higher value of γ for films x = 0 and x = 0.4 is the characteristic energy of the second exponentially decaying tail at lower energies.

5.7 Figures

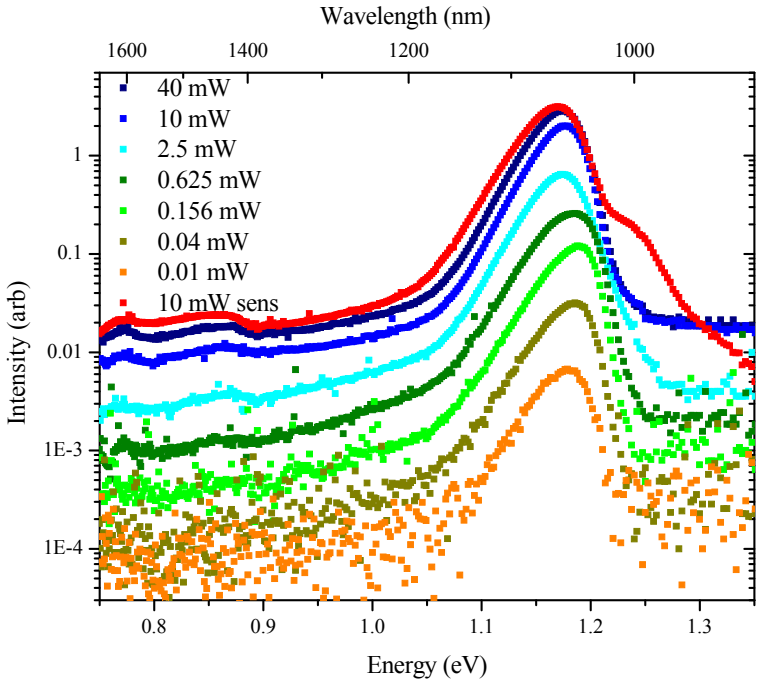

Figure 5.1. Power-dependent PL spectra of $AgInSe_2$ thin film. The data labeled10 mW sens was taken with much higher sensitivity in order to observe low intensity peaks.

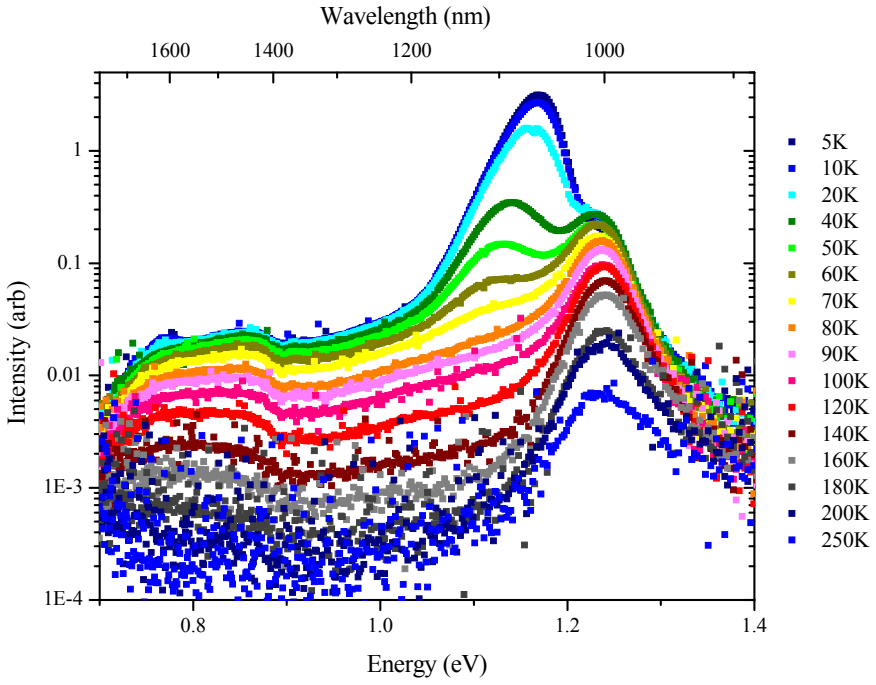

Figure 5.2. Temperature-dependent PL spectra of $AgInSe_2$ thin film.

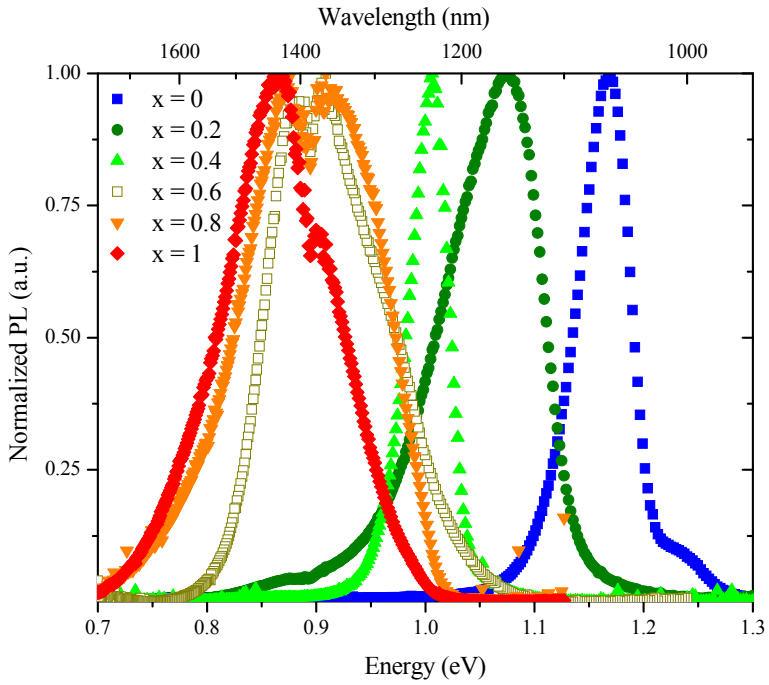

Figure 5.3. Normalized PL emissions from $Cu_xAg_{1-x}InSe_2$ thin films at 10 K and 10 mW excitation power.

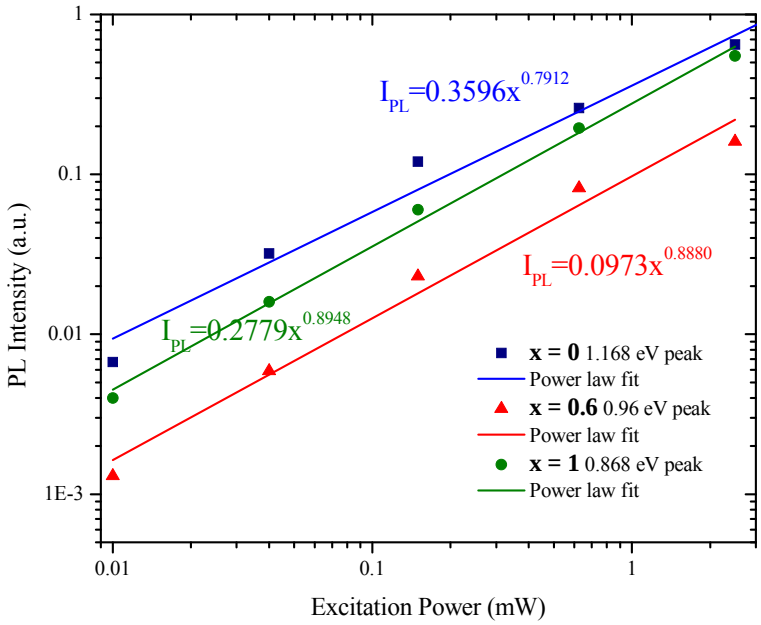

Figure 5.4. PL peak intensity vs. excitation power plots used in extracting *k* values in Schmidt's power law (Equation 1). Data for $x = 0$ are shown with blue squares, $x = 0.6$ with red triangles, and $x = 1$ with green circles.

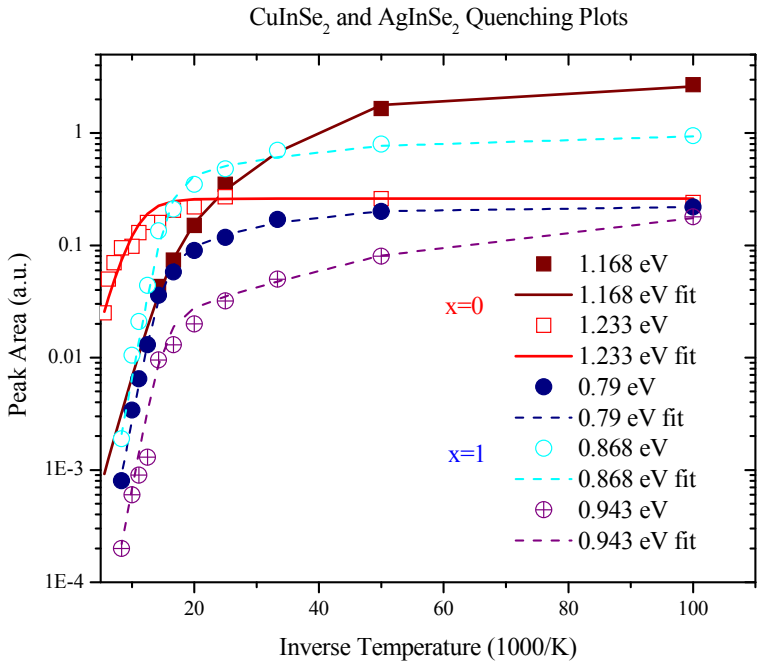

Figure 5.5. Quenching plots of individual peaks for the $CuInSe_2$ and $AgInSe_2$ films. $AgInSe_2$ quenching curves are the red squares with solid red lines as the fits. $CuInSe_2$ quenching curves are the blue circles with the dashed blue lines as the fits. Fits were obtained using Equation 5.4.

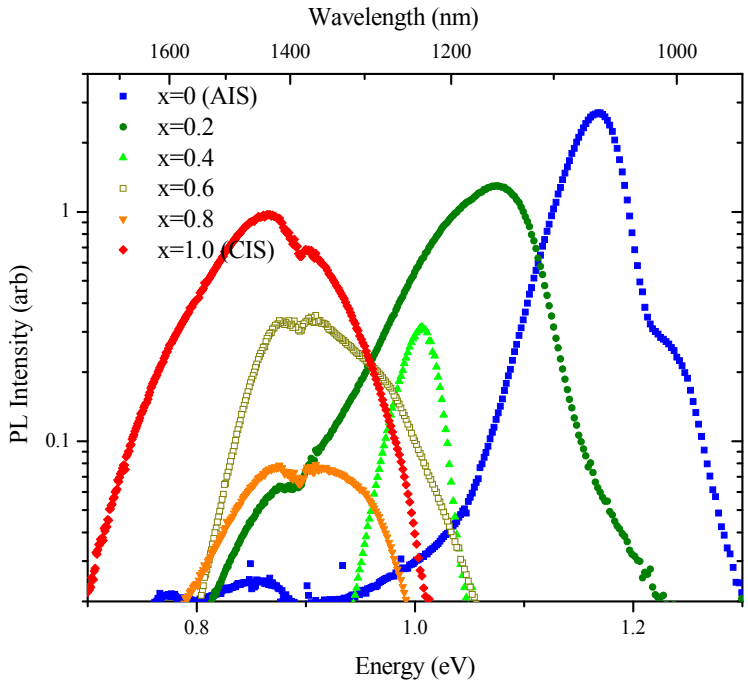

Figure 5.6. PL spectra for $Cu_xAg_{1-x}InSe_2$ thin films.

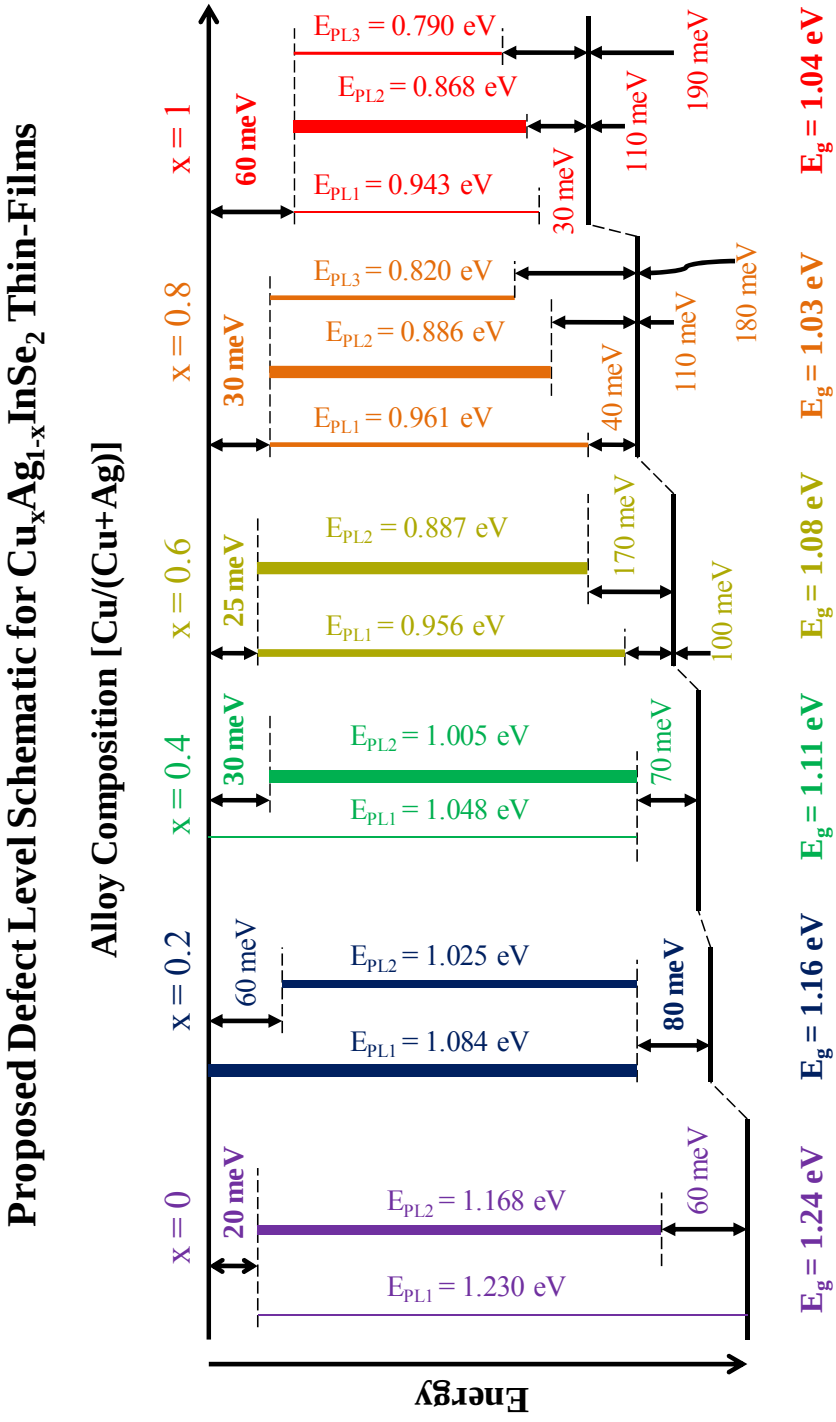

Figure 5.7. Proposed band structure schematic based on optical band gap measurements from transmission/reflection, activation energies from temperature-dependent PL, and calculation of opposite defect based on Equation 2. Some values were rounded off to simplify the diagram. The thickness of the transition line represents the intensity of that transition relative to the other transitions within that sample at 10 K.

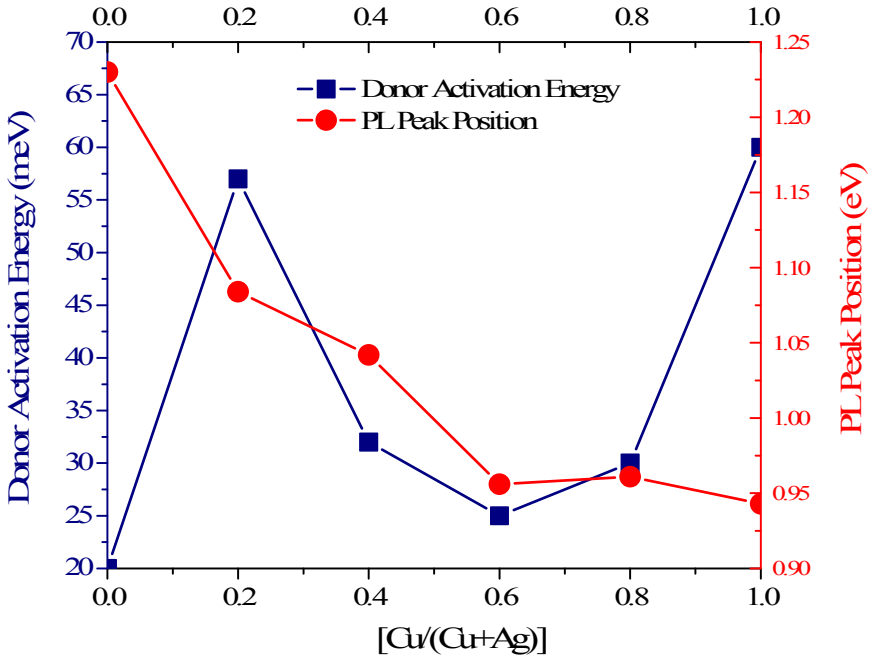

Figure 5.8. Donor activation energy and PL peak position as a function of film composition [Cu/(Cu+Ag)].

CHAPTER 6

MINORITY CARRIER LIFETIMES OF $Cu_xAg_{1-x}InSe_2$ THIN FILMS

Results of minority carrier lifetimes in $Cu_xAg_{1-x}InSe_2$ thin films studied via time-resolved photoluminescence measurements are presented in this chapter. Films were deposited on three different substrates [bare soda-lime glass, Mo-coated soda-lime glass, and (001)-GaAs]. Samples on bare soda-lime glass exhibited the lowest lifetimes (~ 200 ps), consistent with a lack of order in the films and smaller grain sizes. Lifetimes for films on Mo-coated glass showed significantly longer lifetimes, with some films showing increases of up to 1 order of magnitude relative to films on bare soda-lime glass. The lifetimes of the films on Mo-coated glass also increased with increasing grain size and exhibited lifetimes comparable or higher to $CuInSe_2$ for compositions of $x \leq 0.2$.

6.1 Introduction

Alloying Ag with $Cu(InGa)Se_2$ appears to be a promising way of achieving a high band gap semiconductor for use in high-efficiency or tandem junction photovoltaic devices. Nakada *et al.* [1] and Shafarman *et al.* [2–6] have fabricated solar cells using this approach and have achieved efficiencies of 9.3% (Nakada) and 13% (Shafarman) for layers with bandgaps of 1.67eV and 1.6 eV, respectively. The devices fabricated by Shafarman *et al.* showed improved performance in V_{oc}, fill factor, and efficiency when Ag was added up to about Ag/(Ag+Cu) = 0.75. These promising results have spurred interest in the underlying mechanisms responsible for the improvement. Various mechanisms have been suggested, among them better collection of minority carriers

through improved crystalline quality [2]. Photoluminescence studies of $Cu_xAg_{1-x}InSe_2$ presented in Chapter 5 have yielded narrower peaks for the Ag-rich alloys, also suggesting improved crystalline quality [7]. In order to confirm whether the improvement in device performance is due to improved crystalline quality, time-resolved photoluminescence (TRPL) experiments were carried out on a series of $Cu_xAg_{1-x}InSe_2$ thin films, which allow us to calculate the minority carrier lifetime.

Thin-films of $Cu_xAg_{1-x}InSe_2$ were deposited via dc magnetron sputtering and evaporation onto both bare and Mo-coated soda-lime glass (SLG) substrates as described in Chapter 3.2. TRPL decays were measured at room temperature using the time correlated single photon counting technique, as described in Chapter 3.6. Films with $x \leq 0.6$ were measured at their PL peak positions. Films with $x \geq 0.8$ were measured at 1350 nm due to limits in the detector range. Although PL decay measurements for films with $x \geq 0.8$ were not carried out at the PL peak, we still expect the minority carrier lifetimes of these films to be higher than the alloyed films based on previously published data for $CuInSe_2$ layers [9].

6.2 Results and Discussion

PL decay curves of the films deposited on bare and Mo-coated SLG substrates are plotted in Figures 6.1 and 6.2, respectively. These curves were fit with a bi-exponential model:

$$I_{PL}(t) = C_1 e^{-t/\tau_1} + C_2 e^{-t/\tau_2} \quad (6.1)$$

where C_1 and C_2 are pre-exponential coefficients and τ_1 and τ_2 are decay times. The second exponential term is necessary when there is sample heterogeneity or when there is

release of carriers from traps [10]. When discussing "minority carrier lifetime" here, we will refer to the first exponential term (τ_1), as it was the main contribution to the decay as shown by values of $C_1 > 90\%$ for most films. This lifetime (τ_1) was also independent of excitation power from 0.5 – 2 mW, supporting this previous assignment. Minority carrier lifetime values were extracted after deconvolution of the measured signal from the IRF and can be found in Tables 6.1 and 6.2.

For films on bare SLG most data could be fit with a single exponential. $CuInSe_2$ ($x = 1$) and CAIS with $x = 0.8$ showed the highest lifetimes with values close to 300 ps, as seen in Figure 6.3. These two films showed a (220) preferred orientation and larger grains (Figure 6.4), as opposed to the other films which showed (112) preference. The carrier lifetimes for the $x = 1.0$ and 0.8 films are significantly lower than what has been reported for air-exposed absorber layers similar to those used in high-efficiency $CuIn_xGa_{1-x}Se_2$ (CIGS) cells (~300-1000 ps [11][12]). As more Ag was added, the lifetimes decreased significantly, reaching a minimum for the $x = 0.4$ film and then increasing to 120 ps for pure $AgInSe_2$. In principle, one would expect better crystalline quality and hence longer lifetimes for the Ag-based alloys because these were deposited closer to their melting temperature (higher homologous temperature). However, the grain size in the higher Ag alloy films was smaller and may have contributed to the shorter lifetime.

Lifetimes for the series of films deposited on Mo-coated SLG were much higher than on bare SLG (see Figure 6.3). The $CuInSe_2$ ($x = 0$) film had a lifetime of ~ 475 ps. As Ag concentration increased, so did lifetime, peaking at 1068 ps for the $x = 0.6$ film, which is comparable to the lifetimes reported for air-exposed, CIGS layers similar to

those yielding high performance solar cells. Past $x = 0.6$ the lifetime decreased to ~ 234 ps for the $AgInSe_2$ film. [The sample with $x = 0.4$ is not included here because of its abnormal composition (group I/III ratio > 1).] Puech *et al.* reported lower minority carrier lifetimes for Cu-rich CIGS samples compared to In-rich samples, which agrees with the lifetime reported for the $x = 0.4$ sample [9].

The lifetimes of the CAIS films on Mo-coated SLG follow the grain size trend well, as seen in Figure 6.4. However, photoluminescence studies (presented in Chapter 5) of Cu/Ag-poor $Cu_xAg_{1-x}InSe_2$ have shown that the main peaks in films with $x \geq 0.6$ tend to be mostly donor-acceptor pair (DAP) transitions, while peaks in films with $x \leq 0.4$ are typically free-to-bound (FB) transitions [7]. Work by Shimakawa *et al.* [12] has shown that lifetimes related to DAP defects are typically longer than lifetimes related to FB transitions, which could also provide an explanation for the decrease in lifetimes for values of $x < 0.4$. Films on Mo-coated glass also showed a significant second exponential decay time with long values of τ_2 (~ 1-3.8 ns).

An epitaxial $AgInSe_2$ thin-film deposited at 700° C on a (001)-GaAs substrate was also measured in order to compare it to the polycrystalline films. This film contains approximately 5 at. % Ga that diffused from the substrate into the film and contains no Na. The minority carrier lifetime of the epitaxial film was double that of the polycrystalline film on bare glass (~230 ps) and about the same as the film on Mo-coated glass. However, all lifetimes are below the lifetimes achieved for high quality CIGS layers. For example, epitaxial thin films of $CuInSe_2$ with small amounts of Ga typically have lifetimes in the 300-800 ps range [13].

6.3 Conclusions

Minority carrier lifetimes in $Cu_xAg_{1-x}InSe_2$ thin films have been studied. Samples on bare soda-lime glass exhibited the lowest lifetimes (~ 200 ps), consistent with a lack of order in the films and smaller grain sizes. Lifetimes for films on Mo-coated glass showed significantly longer lifetimes, with some films showing increases of up to 1 order of magnitude relative to films on bare soda-lime glass. The lifetimes of the films on Mo-coated glass also increased with increasing grain size and exhibited lifetimes comparable or higher to $CuInSe_2$ for compositions of $x \leq 0.2$.

Correlation between minority carrier lifetimes of CIGS absorber layers measured at room temperature and open circuit voltage and device efficiency has been suggested in previous studies under low-injection conditions [12, 14]. If this correlation were to hold true, we expect that devices fabricated from $Cu_xAg_{1-x}InSe_2$ absorber layers will have efficiencies comparable to CIS for compositions of $x \geq 0.2$. A similar range has been shown by Shafarman *et al.* to yield good devices.

6.4 References

[1] T. Nakada, K. Yamada, R. Arai, H. Ishizaki, and N. Yamada, "Novel Wide-Band-Gap $Ag(In_{1-x}Ga_x)Se_2$ thin film solar cells," *Materials Research Society Symposium Proceedings*, vol. 865, pp. F11.1.1-8, 2005.

[2] W. Shafarman, C. Thompson, J. Boyle, G. Hanket, P. Erslev, and J. D. Cohen, "Device characterization of $(AgCu)(InGa)Se_2$ solar cells," in *35th IEEE Photovoltaic Specialists Conference (PVSC), 2010*, 2010, pp. 000325–000329.

[3] G. Hanket, J. H. Boyle, and W. N. Shafarman, "Characterization and device performance of $(AgCu)(InGa)Se_2$ absorber layers," *34th IEEE Photovoltaic Specialists Conference (PVSC)*, pp. 001240-001245, Jun. 2009.

[4] J. Boyle, G. Hanket, and W. Shafarman, "Optical and quantum efficiency analysis of (Ag,Cu)(In,Ga)Se_2 aborber layers," in *Conference Record IEEE Photovoltaic Specialists Conference*, 2009, pp. 1349-1354.

[5] P. T. Erslev, G. M. Hanket, W. N. Shafarman, and J. D. Cohen, "Characterizing the effects of silver alloying in chalcopyrite CIGS solar cells with junction capacitance methods," *Materials Research Society Symposium Proceedings*, vol. 1165, pp. 1165-M01-07, 2009.

[6] J. H. Boyle, B. E. McCandless, G. M. Hanket, and W. N. Shafarman, "Structural characterization of the (AgCu)(InGa)Se_2 thin film alloy system for solar cells," *Thin Solid Films*, Jan. 2011.

[7] A. R. Aquino, S. A. Little, S. Marsillac, R. W. Collins, and A. A. Rockett, "Identification of Defect Levels in $Cu_xAg_{1-x}InSe_2$ Thin Films via Photoluminescence," *Proceedings of the 37th IEEE Photovoltaic Specialists Conference*, 2011.

[8] T. Begou et al., "In situ and ex situ Characterization of (Ag,Cu)$InSe_2$ Thin Films," *Conference Record 37th IEEE Photovoltaic Specialists Conference*, 2011.

[9] K. Puech, S. Zott, K. Leo, M. Ruckh, and H.-W. Schock, "Determination of minority carrier lifetimes in $CuInSe_2$ thin films," *Applied Physics Letters*, vol. 69, no. 22, p. 3375, 1996.

[10] W. K. Metzger et al., "Time-resolved photoluminescence studies of CdTe solar cells," *Journal of Applied Physics*, vol. 94, no. 5, p. 3549, 2003.

[11] W. K. Metzger, I. L. Repins, and M. a. Contreras, "Long lifetimes in high-efficiency Cu(In,Ga)Se_2 solar cells," *Applied Physics Letters*, vol. 93, no. 2, p. 022110, 2008.

[12] S.-ichi Shimakawa et al., "Characterization of Cu(In,Ga)Se_2 thin films by time-resolved photoluminescence," *Physica Status Solidi (a)*, vol. 203, no. 11, pp. 2630-2633, Sep. 2006.

[13] S. Niki et al., "Molecular beam epitaxial growth and characterization of $CuInSe_2$ and $CuGaSe_2$ for device applications," *Journal of Crystal Growth*, vol. 237-239, pp. 1993-1999, 2002.

[14] B. Ohnesorge, R. Weigand, G. Bacher, a. Forchel, W. Riedl, and F. H. Karg, "Minority-carrier lifetime and efficiency of Cu(In,Ga)Se_2 solar cells," *Applied Physics Letters*, vol. 73, no. 9, p. 1224, 1998.

6.5 Tables

x	PL measurement (nm)	τ_1 (ps)	τ_2 (ps)	Average Grain Area (μm^2)	Cu+Ag (at.%)	In	Se
0 (epi)	940	230	950	NA	20.17	23.74	56.08
0	990	115	0	0.0714	22.27	23.16	54.56
0.2	1130	74	0	0.1176	20.78	29.98	49.25
0.4	1130	19	0	0.1132	24.85	25.96	49.19
0.6	1200	111	0	0.0789	20.55	28.11	51.35
0.8	1350	297	0	0.1667	24.23	25.60	50.17
1.0	1350	279	0	0.3157	23.75	26.67	49.57
* at.%. EDS data taken at 15kV and fit using L peaks. Na values range from 0.01%-0.2%.							

Table 6.1. Values of the $Cu_xAg_{1-x}InSe_2$ series deposited on bare glass substrates.

x	PL measurement (nm)†	τ_1 (ps)	τ_2 (ps)	Average Grain Area (μm^2)	Cu+Ag (at.%)	In	Se
0	990	234	1036	0.3221	18.94	27.59	53.47
0.24	1130	493	1782	0.4416	21.15	27.82	51.09
0.39	1130	199	0	0.6184	**25.64**	**23.46**	50.90
0.58	1200	1068	3873	0.3692	18.57	28.22	52.39
0.79	1350	623	2067	0.2546	16.49	28.11	55.40
1.0	1350	476	0	0.2181	18.86	27.30	53.85
* at.%. EDS data taken at 15kV and fit using L peaks. Na values range from 0.01%-0.2%. †A regeneratively amplified Yb:KGW laser system with a beam diameter of 0.02 mm was used for this series. The repetition rate was 1 MHz, pulse length 0.3 ps, average laser power 0.8 mW. Note that because of higher repetition rate, energy per pulse was 0.8 mW/1E6 s^{-1} = 0.8 nJ, making the total energy per unit area larger for this series.							

Table 6.2. Values of the $Cu_xAg_{1-x}InSe_2$ series deposited on Mo-coated glass.

6.6 Figures

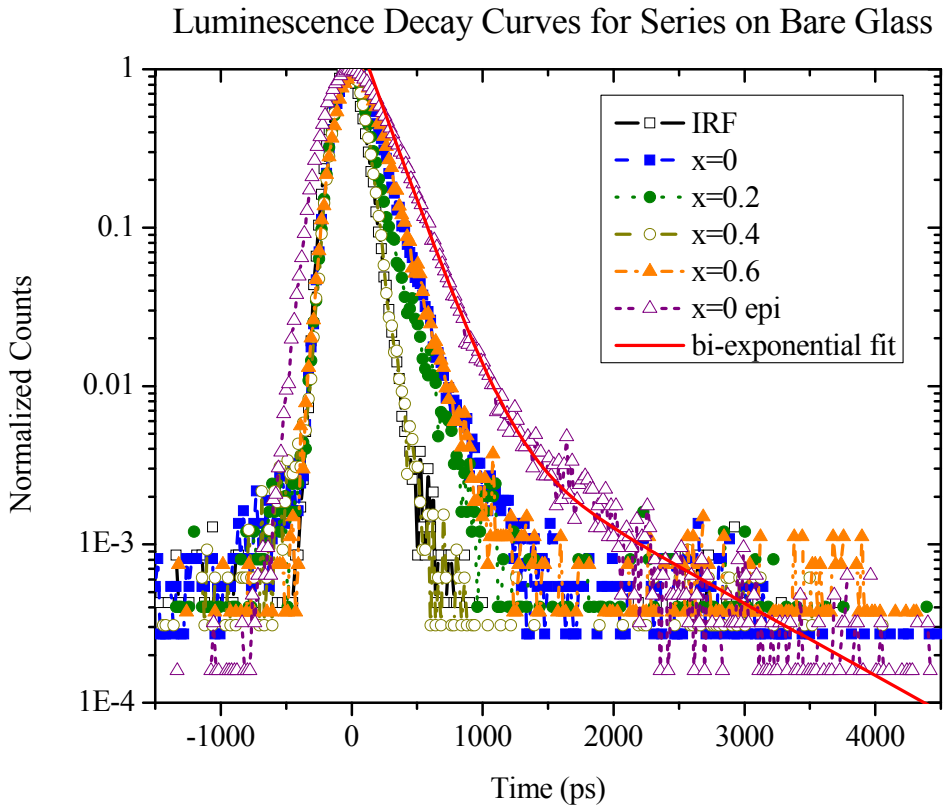

Figure 6.1. Time-resolved photoluminescence of $Cu_xAg_{1-x}InSe_2$ thin-films deposited on bare glass substrates. IRF stands for the instrument response function. The PL decay curve for x = 0.4 is below the IRF curve, meaning that its lifetime is below our time resolution. A decay curve for an epitaxial $AgInSe_2$ sample deposited on 001-GaAs is also included.

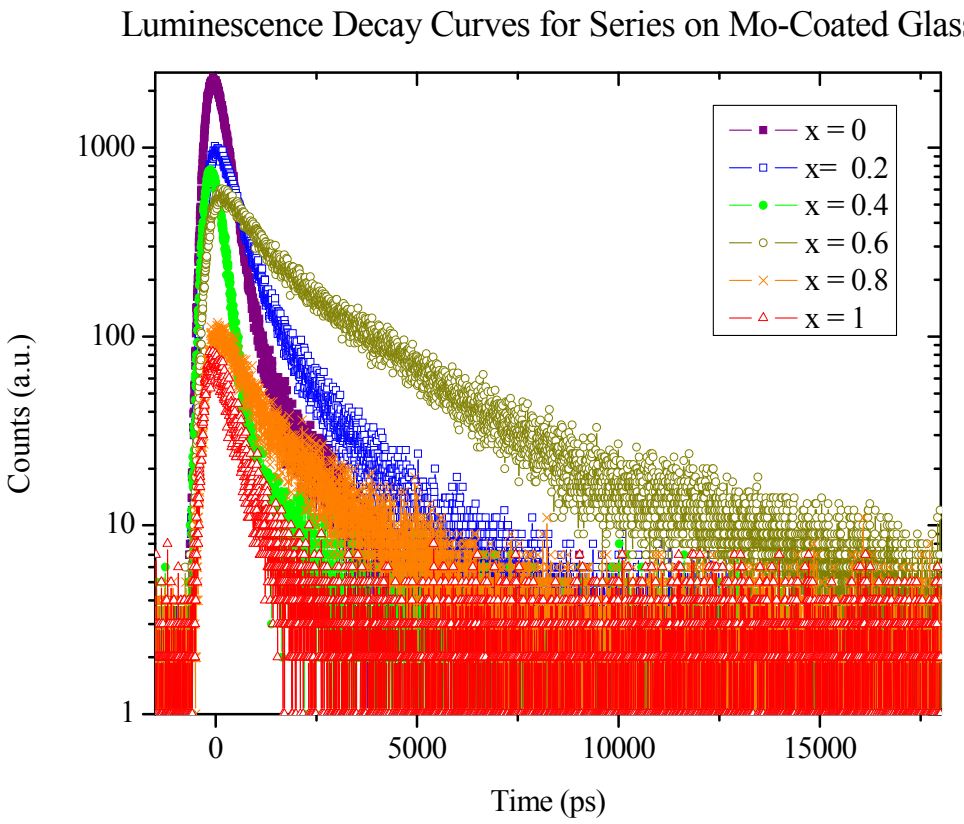

Figure 6.2. Luminescence decay of polycrystalline $Cu_xAg_{1-x}InSe_2$ thin films deposited on Mo-coated soda-lime glass substrates. Laser power was set at 0.8 mW for this series, as opposed to 2 mW.

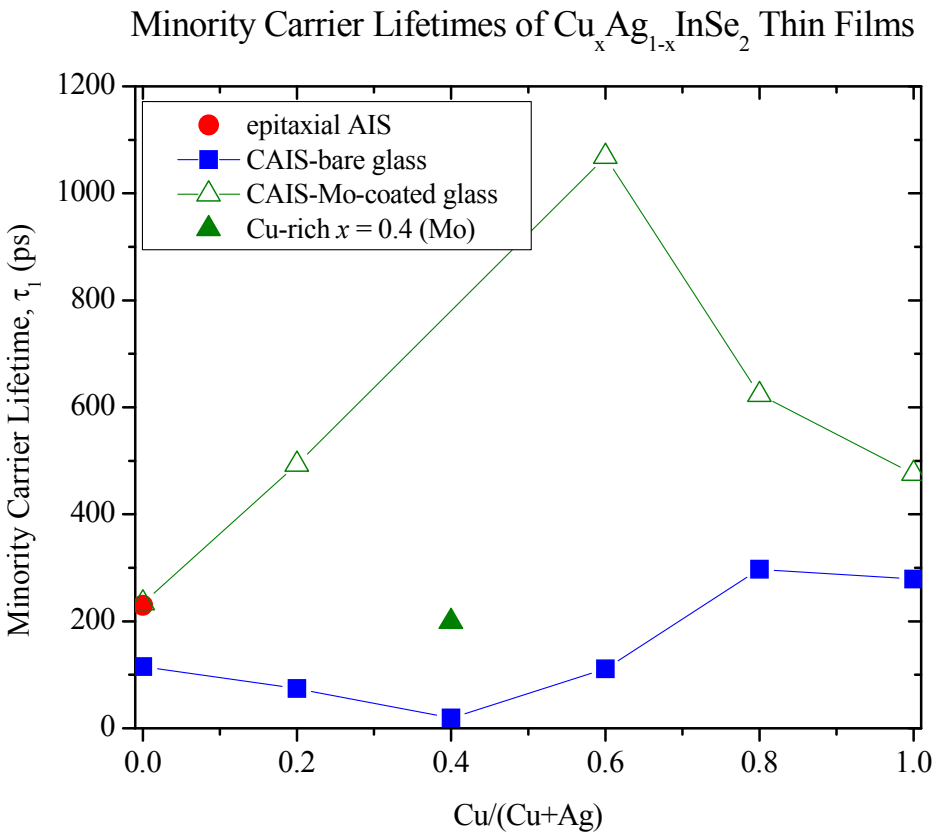

Figure 6.3. Minority carrier lifetime values of $Cu_xAg_{1-x}InSe_2$ thin films measured via TRPL. Notice the deviation in the trend at $x = 0.4$ for the series deposited on Mo-coated glass. This sample was the only film with a group I/III ratio higher than 1, indicating the possibility of secondary phase formation in the film.

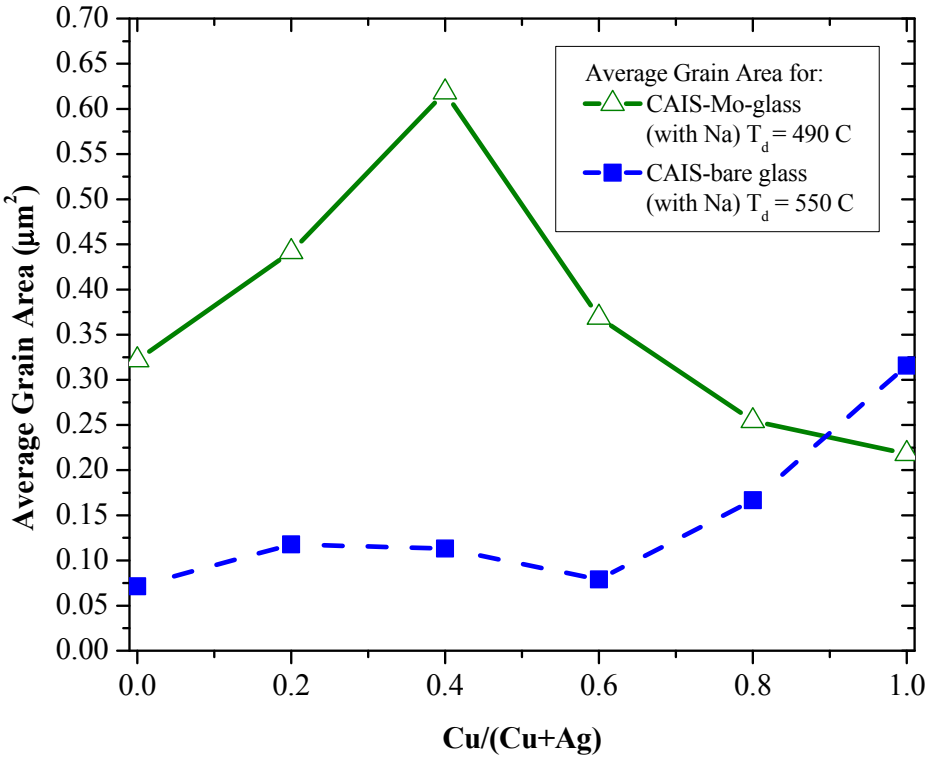

Figure 6.4. Average grain area of CAIS deposited on bare and Mo-coated SLG substrates. Values were obtained by using the planimetric method on SEM images. Notice the similarity between the trends in grain size and the minority carrier lifetimes.

CHAPTER 7

SPATIAL DISTRIBUTION OF DEFECTS IN $Cu_xAg_{1-x}InSe_2$ THIN FILMS

7.1 Introduction

Defect levels in the band gap and the point defects responsible for them were identified in thin-films of $Cu_xAg_{1-x}InSe_2$ in Chapter 5. Now that these defects have been indentified, the next step is to know how they are spatially distributed within the material and, if possible, what defects or structures affect them. Cryogenic cathodoluminescence (CL) experiments, including the spectral and imaging modes, are presented in this chapter. Details of the experiment can be found in Chapter 3.6. The purpose of these experiments was to study the emission spectrum of grains and grain boundaries in $Cu_xAg_{1-x}InSe_2$. A decrease in emission intensity from the grain boundary would indicate a possible increase in non-radiative recombination there, which could be detrimental for solar cells.

Monochromatic CL spectra were collected, analyzed, and fit. Spectrally-resolved CL images were then obtained at the peak center position and along the exponentially decaying band tail, typically observed in these materials. The spectrally resolved images were colorized and overlaid to highlight spatial and spectral variations in luminescence. Panchromatic images (sensitive to all wavelengths of light) were also recorded for each sample.

7.2 Results and Discussion

The surface morphology of a sample of AIS is shown in Figure 7.1a. A monochromatic CL spectrum was taken at 30kx magnification from this area and is shown in Figure 7.2. A best fit to the CL data was obtained for a Gaussian peak at 1.215 eV (FWHM = 34.7 meV) combined with an exponential tail on the lower energy side, which decayed at a rate of 44 meV/decade. Spectral images were acquired at the peak position and along the band tail (1.228 eV, 1.216 eV, and 1.169 eV). The spectral images have been overlaid in Figure 7.1b. The emission at 1.169 eV is colorized as red, while the 1.228 eV and 1.216 eV emissions contribute blue and green to the overlay, respectively.

The spectral images show no significant difference in distribution of emission with respect to position indicating compositional uniformity, unlike the samples with $x > 0$, as discussed below. By comparing the scanning electron image (SEI) to the CL spectral image, we can see that the majority of grains exhibit some type of emission. The AIS sample is affected relatively little by protuberant surface features, meaning moderate non-radiative surface recombination. Another important observation is that grain boundaries in this sample do not appear to luminesce more or less than the surrounding grains. This means that the grain boundaries are not acting as non-radiative recombination centers, nor is surface topography affecting the distribution of light emitted. This was confirmed with the acquisition of a panchromatic CL image as seen in Figure 7.1d. Most dark areas in the panchromatic CL image correspond to dark areas in the SEI.

Power-dependent CL spectra for this sample are plotted on a semi-logarithmic scale in Figure 7.3. The spectra from 22 pA to 640 pA beam current can be modeled using a Gaussian peak with an exponential band tail. The Gaussian peak undergoes a blue-shift from 1.206 eV to 1.226 eV as power increases. When the excitation current is increased past 2,560 pA, second and third exponential tails are observed at the low energy (< 1.062 eV) and high energy ends (> 1.305 eV), respectively. The Gaussian peak continues blue-shifting with increasing excitation current until reaching a maximum shift of 41 meV at 40,960 pA (1.247 eV). This behavior is consistent with a donor-acceptor pair (DAP) transition and agrees with the photoluminescence (PL) data presented in earlier chapters. If we consider the spectral images acquired via CL with the defect levels identified via PL and CL, we can say that the defects involved in the DAP transition (probably V_{Ag}, In_{Ag}) are distributed uniformly in this film.

A similar type of analysis was conducted on the rest of the films in this series. A secondary electron image from the $Cu_{0.6}Ag_{0.4}InSe_2$ (x = 0.6) sample is shown in Figure 7.4a. CL spectral images were acquired at 1.033 eV (blue channel), 1.008 eV (green channel), and 0.969 eV (red channel) and the overlay image is shown in Figure 7.4b. This sample exhibits a lot more spatial and spectral variation than the other samples. There was some enhanced emission seen from the grain boundary areas in the mono CL overlay. The white areas (see Figure 7.4b) indicate the presence of all three emission wavelengths, and these seem to lie across grain boundary or inter-grain areas. This sample has the most variation of emissions from grain to grain. Some grains appear to luminesce only at one wavelength, and others do not luminesce at all, suggesting that there are compositional or electrically-active defect fluctuations among grains.

A panchromatic CL image (see Figure 7.4d) confirms these observations and reveals a severe reduction in emission intensity from protuberant surface features. Enhanced emission intensity from grain boundary areas is also seen. In fact, most of the red areas (more intense emission) in the image correspond to grain boundary areas in the SEM image. The dark areas in the panchromatic CL image correspond to protruding features in the SEM image and reveal the influence of surface recombination in this film.

Power-dependent spectra for the x = 0.6 film (Figure 7.5) are broader than the emissions from the x = 0 sample, as was the case with the PL spectra shown in Chapter 5. Two Gaussian peaks at 1.010 eV and 0.976 eV are required to obtain a best fit for the 22 and 40 pA spectra. As the excitation power is increased, exponential tails appear on both high and low energy sides of the peak, as was seen for the x = 0 sample. Both Gaussian components blue-shift (20 meV and 15 meV) with increasing excitation power, consistent with a DAP transition in PL measurements.

A secondary electron image for the pure $CuInSe_2$ sample is shown in Figure 7.6a. Emission spectra were acquired at 0.984 eV (blue channel), 0.954 eV (green channel), and 0.855 eV (red channel) and the overlay image is shown in Figure 7.6b. This sample also exhibits a lot of spatial and spectral variation. The red emission from this spectrum was fairly uniform throughout the sample, but with higher intensity inside the grains. This was true even close to surface facets and grain boundary edges. The other emission peaks did not luminesce well in these areas. However, the blue and green emissions were very strong near the grain boundaries. This behavior in emissions suggests that there are compositional or electrically-active defects present near or at the grain boundaries.

A panchromatic CL image (see Figure 7.6d) reveals a severe reduction in emission intensity from protuberant surface features and facets. Most grains appear to luminesce fairly well from the center regions. Enhanced emission intensity from grain boundary areas is also seen in the panchromatic CL image, confirming the monochromatic CL results. The power-dependent CL series (see Figure 7.7) shows even broader emissions for the $CuInSe_2$ sample (FWHM = 95 meV for the 160 pA spectrum). All peaks blue-shift 22-32 meV with increasing power, indicating DAP transitions as observed in the PL data in Chapter 5. These spectra also seem to have high and low energy exponential tails, especially at high powers.

Based on the CL spectral images collected and on the identification of defects in Chapter 5, it appears that the blue (0.984 eV) and green (0.954 eV) transitions are concentrated around inter-grain areas, while the red (0.855 eV) transition is concentrated within the grains. This means that the defect level associated with the blue and green transitions (likely V_{Cu}) are localized at the grain boundaries or inter-grain areas. This result is consistent with the work of Liao *et al.* [1], who showed that the surface (top 1-2 monolayers) of $CuInSe_2$ is Cu-deficient. Such a Cu-deficiency would be too small to detect via nano-EDS, but still significant to change the concentration of electrically active defects in the region.

The atomic composition of grains vs. grain boundaries was characterized by TEM. Specimens were prepared for these three films, as described in Chapter 3.4. Nano-EDS scans were then taken along various grain boundaries for each sample. However, no statistical difference was observed between grain boundaries vs. grain atomic composition for the films. This result agrees with that of Lei *et al.* [2] who also

observed no significant differences in atomic composition between grains and their boundaries via nano-EDS.

Cathodoluminescence spectral images were also acquired on films with x = 0.2 and x = 0.8, as seen in Figures 7.8b and 7.8d. These two films exhibited a similar behavior to the other alloyed film, x = 0.6. Different grains had varying spectral emissions and enhanced emission was obtained from inter-grain areas. From the imaging, it appears that the high energy emission is concentrated at the top of certain grains, while the lower energy emissions form a network or mesh around these grains. This is more evident in the film with the ordered defect compound (x = 0.2) and confirms the glancing incidence XRD experiments discussed in Chapter 4, where the ODC was found near the films surface.

In order to reduce topographical effects in the films, CL measurements were also acquired from polished samples. The surface of the films was "planarized" using an ion-beam polisher in order to obtain flat samples, as described in Chapter 3.8. Overall, CL spectra and images were very similar to the unpolished samples, but with much lower intensities due to the introduced damage at the surface of the films. The SEI of the planarized films x = 0, 0.2, and 1 can be seen in Figures 7.10-7.12, together with their respective CL spectral images. The $AgInSe_2$ film showed very uniform emissions, as it did before the polishing process. As x increased, more variation was observed in the emissions both spatially and spectrally as seen in films x = 0.2 and x = 1. These results were similar to those obtained before polishing, meaning that the conclusions reached in the previous sections are still valid.

7.3 Conclusions

Emissions from $AgInSe_2$ are more uniform both spatially and spectrally than Cu-containing samples. $AgInSe_2$ is also less affected by reduced emission from surface features, presumably due to less surface recombination. Cu-containing samples exhibit enhanced luminescence from grain boundaries or inter-grain areas and localized luminescent variations indicative of compositional or electrically-active defect fluctuations. This was more apparent from grain to grain in the $Cu_{0.6}Ag_{0.4}InSe_2$ sample which showed the most variation in emission from one grain to another. The $CuInSe_2$ sample showed the most variation in emission from grain to grain boundary, indicating possible chemical fluctuations at the grain boundaries. As the Cu content in the films increases, emissions get broader indicating more local chemical fluctuations.

The results presented here have implications for device operation. First, the relatively uniform luminescence from the $AgInSe_2$ sample suggests that this material may produce more uniform cell performances, because reduced fluctuations in chemical composition and band structure from one location to another would result in more efficient energy collection. Variations in band structure would shunt the device locally, leading to low current high voltage grains with large energy gaps being shunted by adjacent high current low energy gap grains. At the same time, reduced surface recombination in air-exposed samples could result in less air-sensitivity during manufacture of $AgInSe_2$ based devices and in less dependence on a particular method for forming the current collecting heterojunction. On the other hand, the lack of variation in luminescence between grains and grain boundaries in AIS suggests that the grain

boundaries may be more active as recombination centers than in the case of CIS. This would degrade the device performance.

7.4 References

[1] D. Liao and A. Rockett, "Cu depletion at the CuInSe 2 surface," *Applied Physics Letters*, vol. 82, no. 17, pp. 2829-2831, 2003.

[2] C. Lei, C. M. Li, a. Rockett, and I. M. Robertson, "Grain boundary compositions in Cu(InGa)Se[sub 2]," *Journal of Applied Physics*, vol. 101, no. 2, p. 024909, 2007.

7.5 Figures

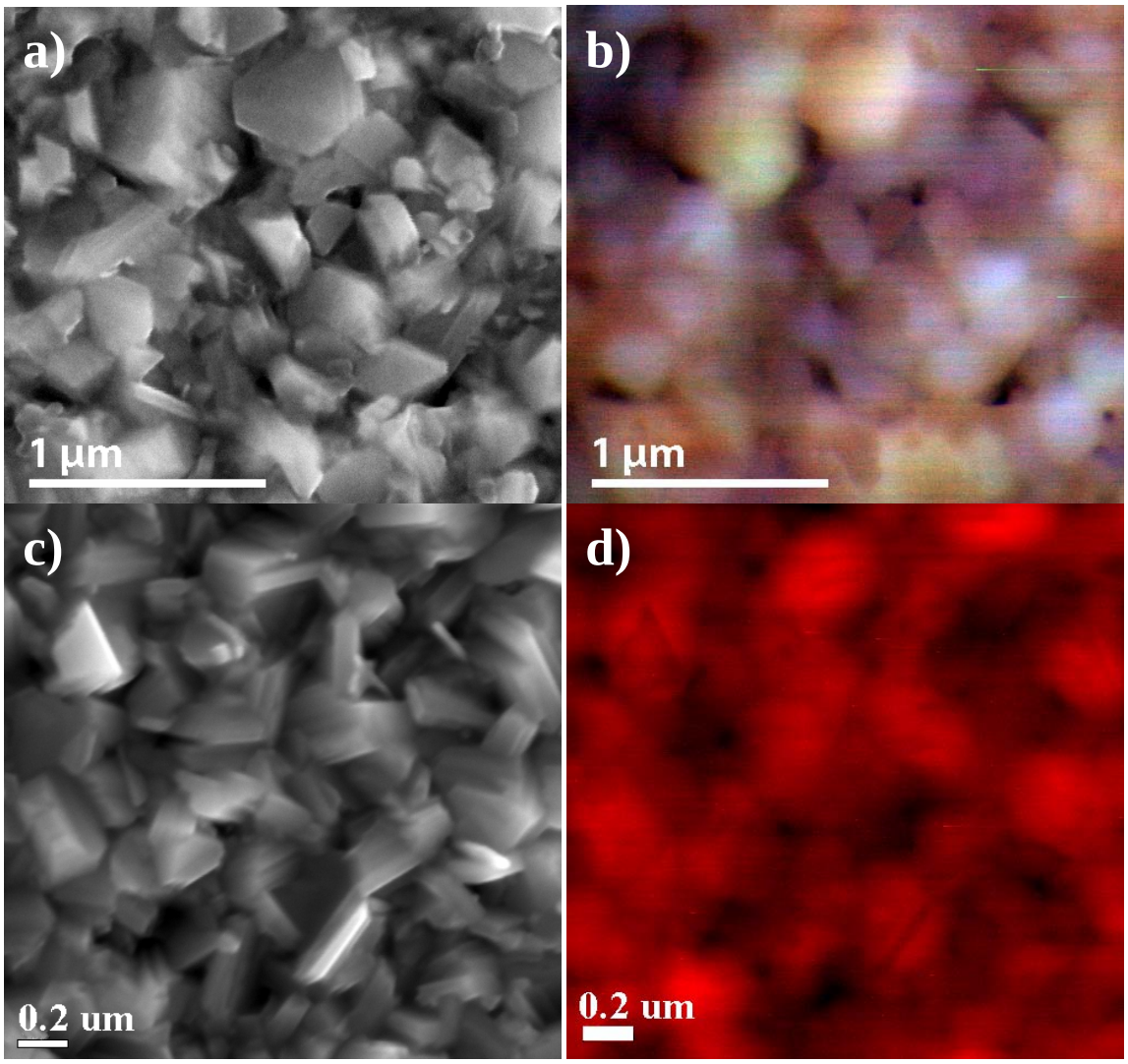

Figure 7.1. Cathodoluminescence images of $AgInSe_2$ film. a) SEI of the area where monochromatic CL images were acquired and overlaid to construct the CL map. b) Monochromatic CL overlay map with 1.228 eV emission colorized blue, 1.216 eV emission colorized green, and 1.619 eV emission colorized red. c) SEI of area where d) panchromatic CL image was acquired.

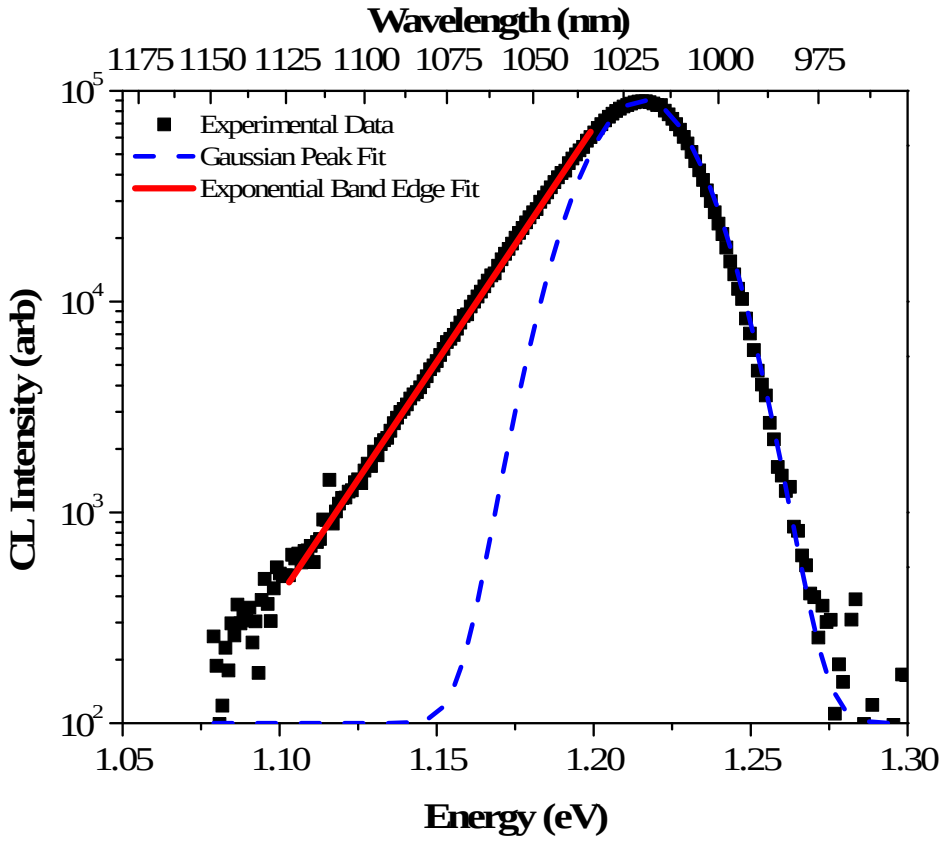

Figure 7.2. $AgInSe_2$ CL spectrum at 10K with the appropriate fit. A single Gaussian peak together with an exponentially decaying tail was needed for a best fit.

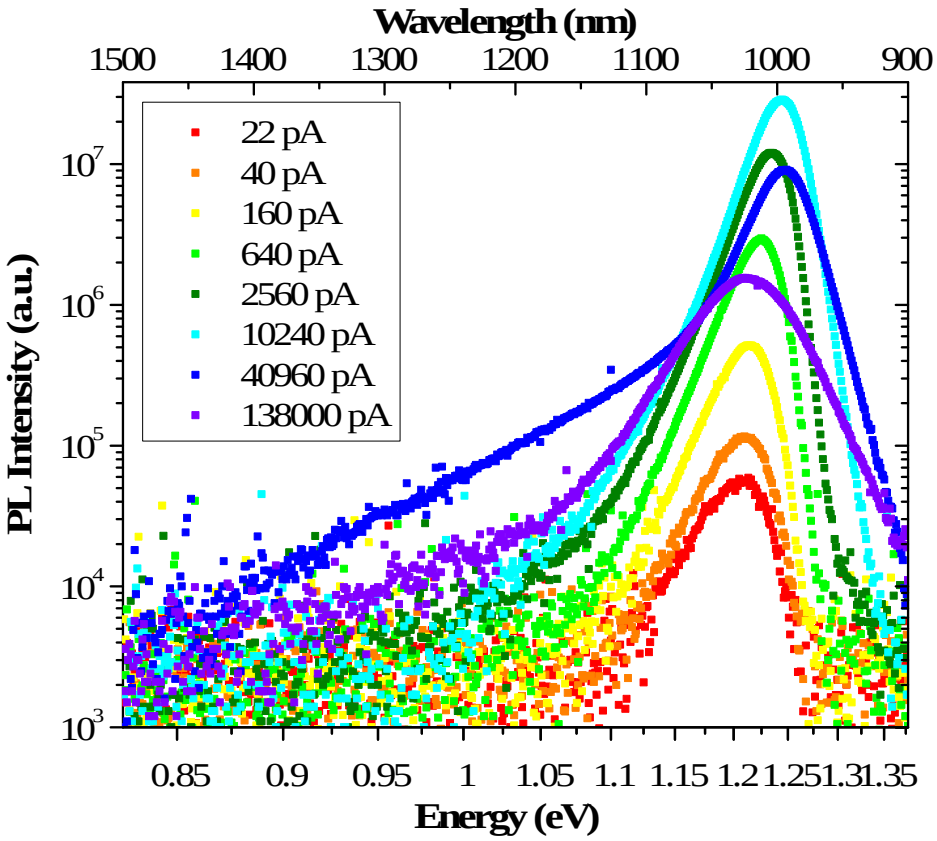

Figure 7.3. Power-dependent CL spectra of $AgInSe_2$ at 10K. The main peak blueshifted with increasing excitation power, consistent with a DAP transition and in agreement with the results from PL presented in Chapter 5.

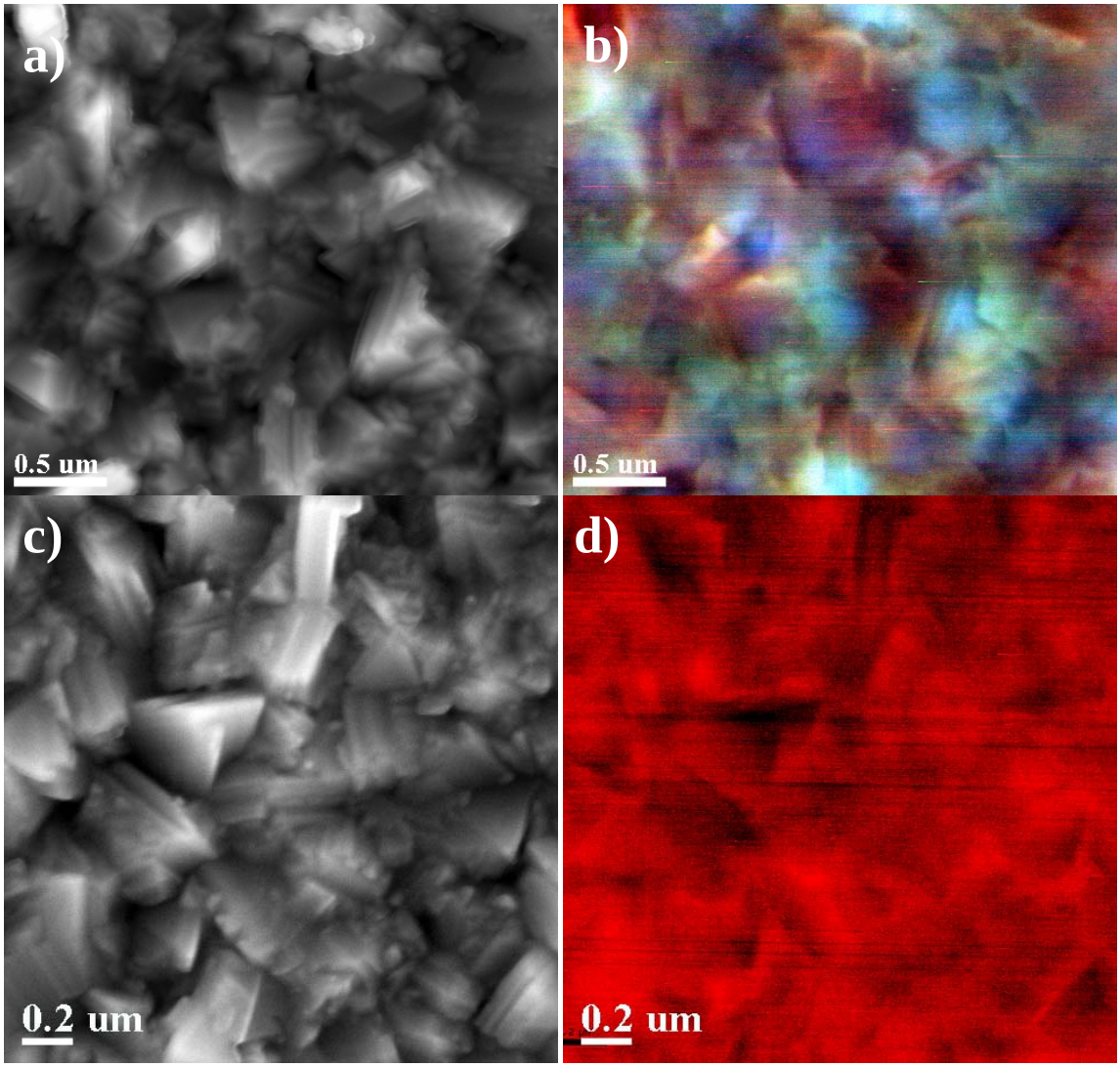

Figure 7.4. Cathodoluminescence images of $Cu_{0.6}Ag_{0.4}InSe_2$ film. a) SEI of the area where monochromatic CL images were acquired and overlaid to construct the CL map. b) Monochromatic CL overlay map with 1.033 eV emission colorized blue, 1.008 eV emission colorized green, and 0.969 eV emission colorized red. c) SEI of area where d) panchromatic CL image was acquired.

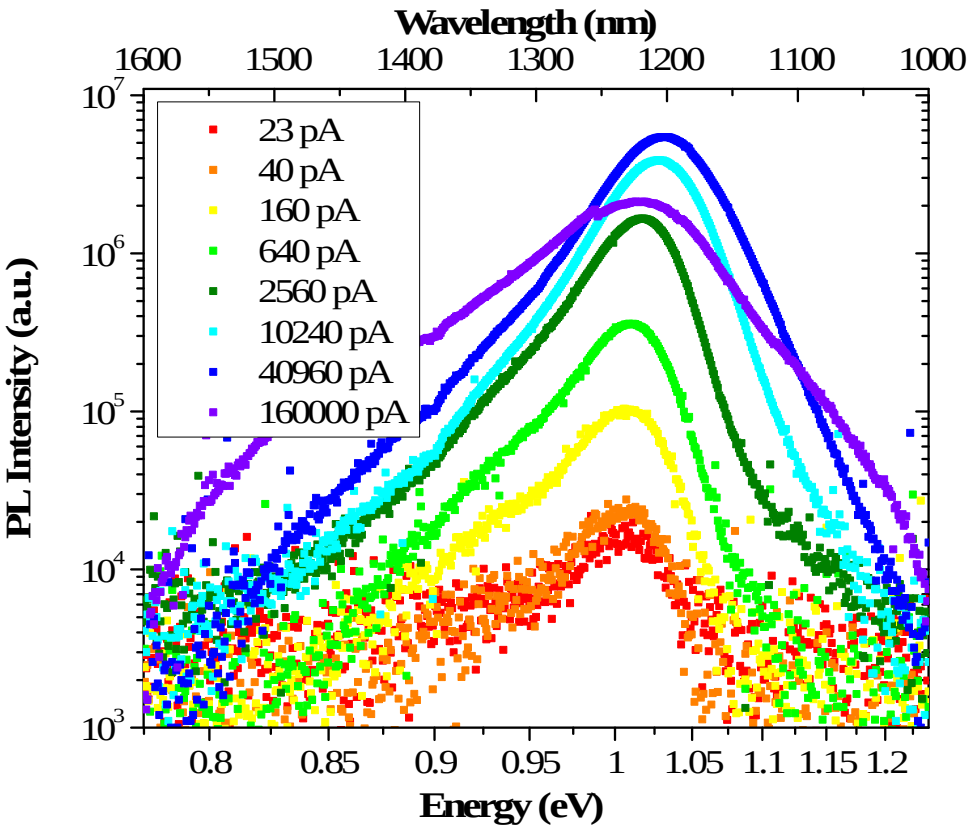

Figure 7.5. Power dependent CL spectra of $Cu_{0.6}Ag_{0.4}InSe_2$ thin film at 10K. The main peak in this film also blueshifted with increasing excitation power, indicating a DAP as confirmed earlier via PL.

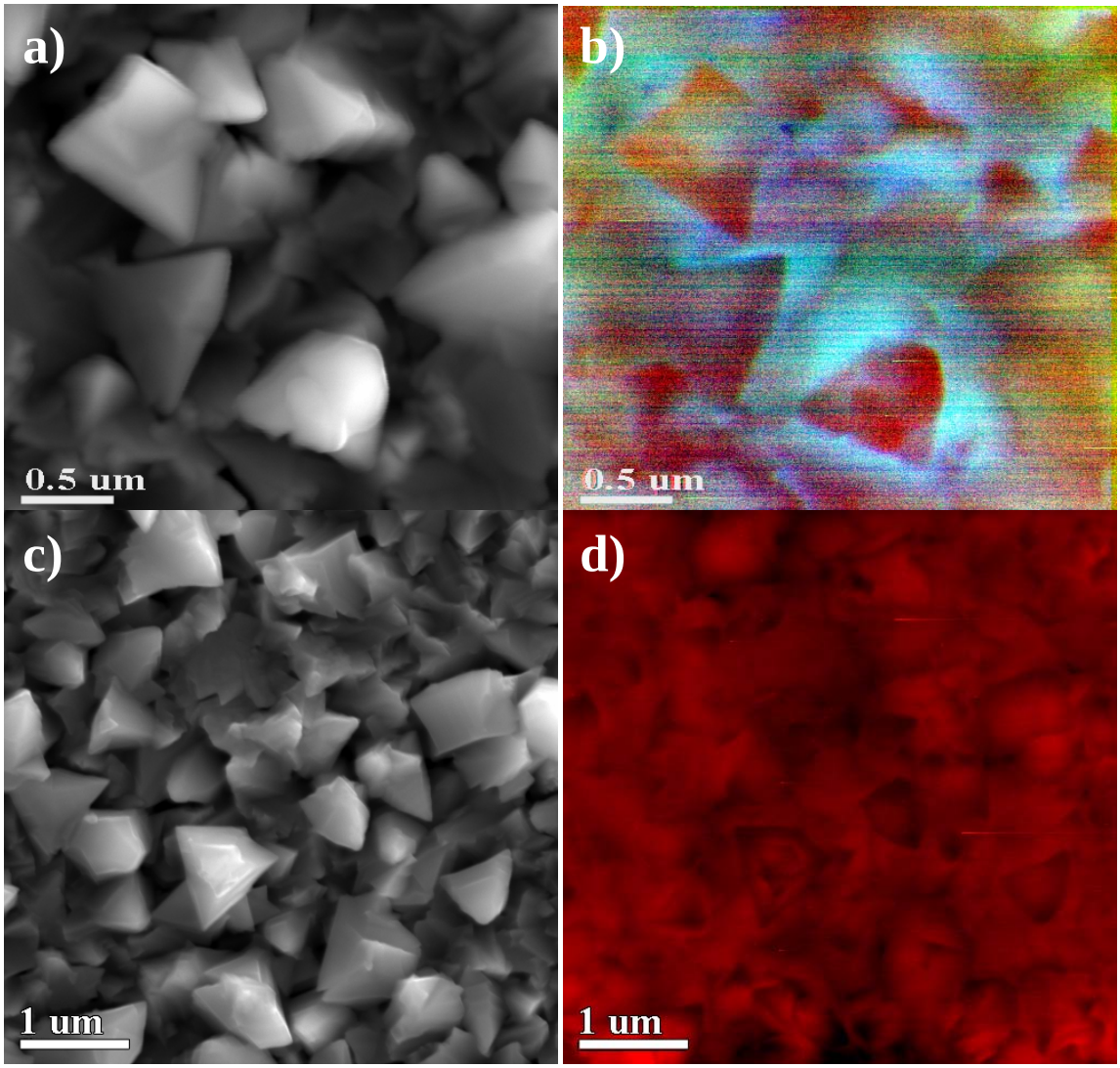

Figure 7.6. Cathodoluminescence images of $CuInSe_2$ film. a) SEI of the area where monochromatic CL images were acquired and overlaid to construct the CL map. b) Monochromatic CL overlay map with 0.984 eV emission colorized blue, 0.954 eV emission colorized green, and 0.855 eV emission colorized red. c) SEI of area where d) panchromatic CL image was acquired.

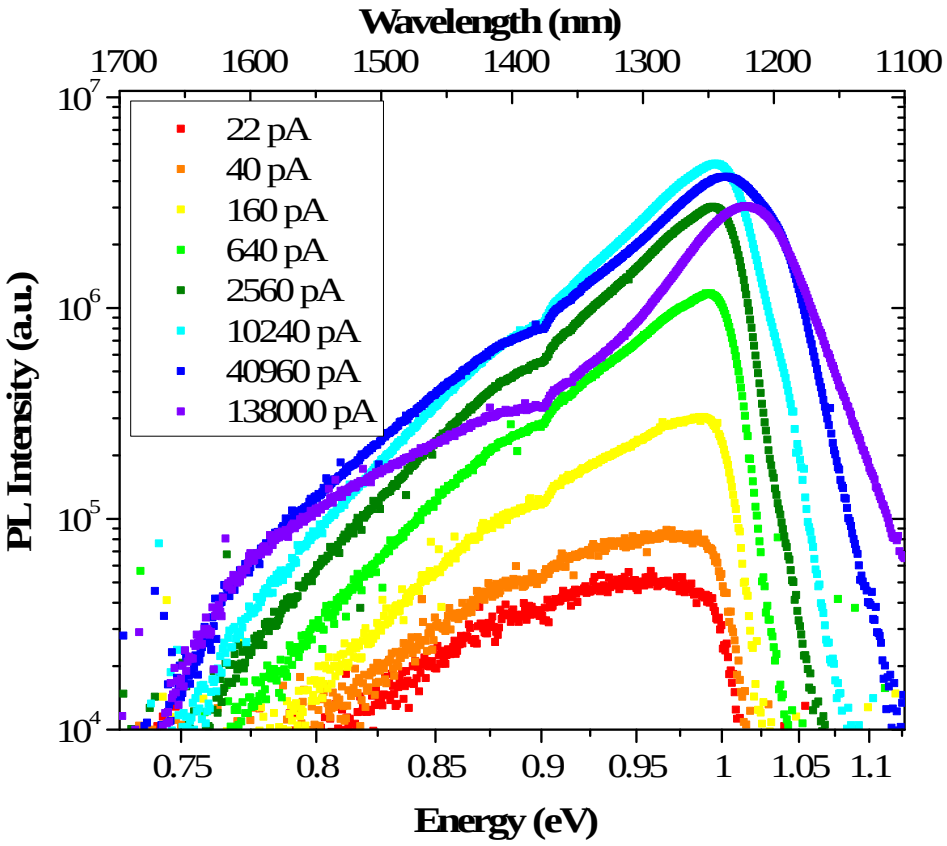

Figure 7.7. Power dependent CL spectra of $CuInSe_2$ thin film at 10K. The main peak in this film also blueshifted with increasing excitation power, indicating a DAP as confirmed in Chapter 5 via PL.

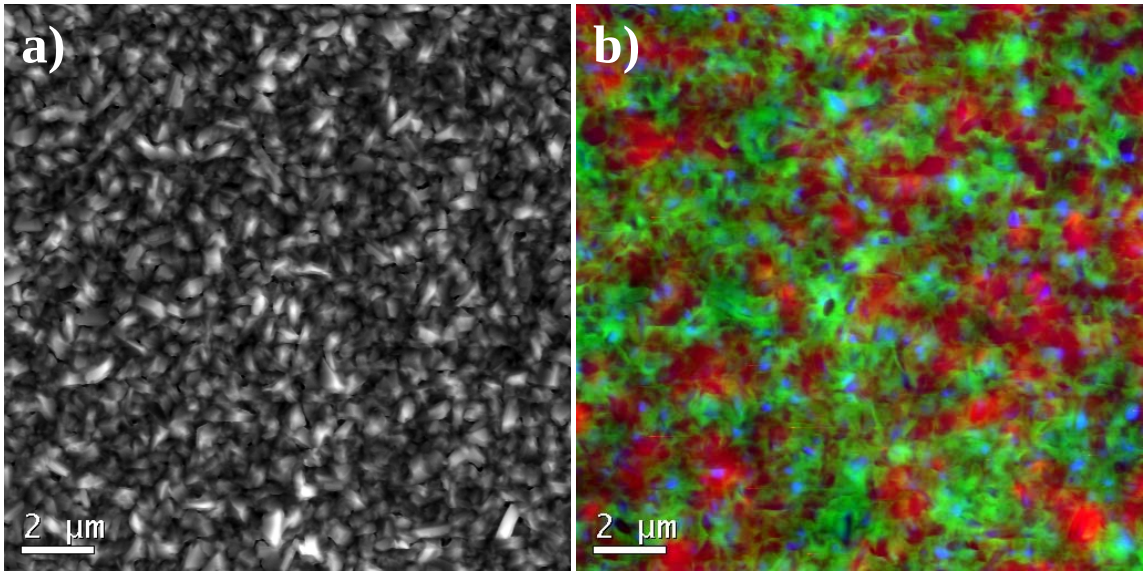

Figure 7.8. a) SEI of the area where monochromatic CL images of film x = 0.2 were acquired and overlaid to construct the CL map. b) Monochromatic CL overlay map of x = 0.2 with 1.181 eV emission colorized blue, 1.121 eV emission colorized green, and 1.033 eV emission colorized red. The higher energy emissions (blue) are localized near the surface, making it likely that this contribution is due to the ODC observed in Chapter 4.

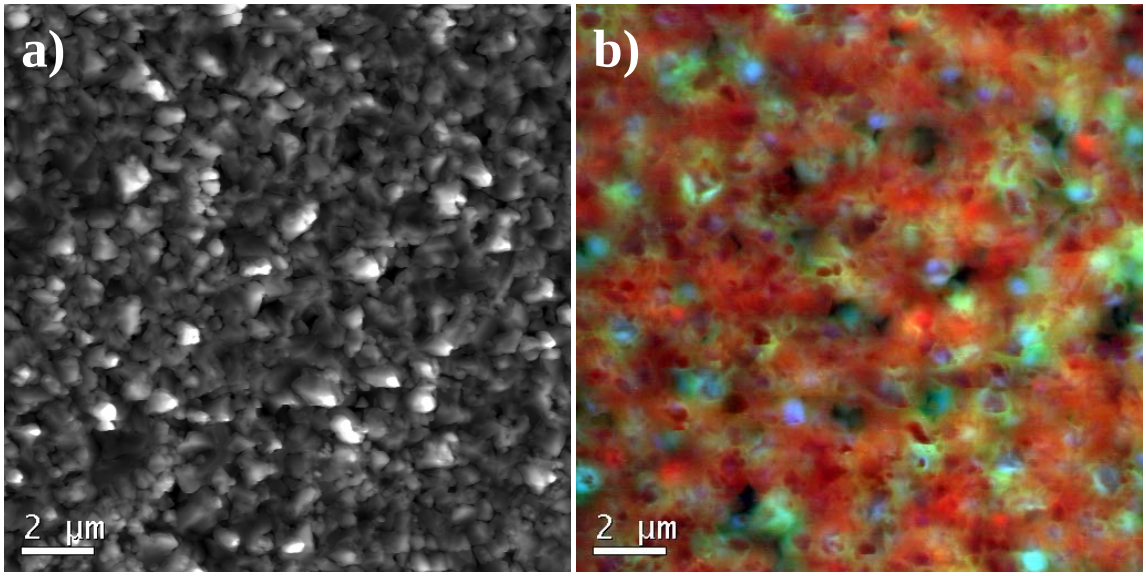

Figure 7.9. a) SEI of the area where monochromatic CL images of film x = 0.8 were acquired and overlaid to construct the CL map. b) Monochromatic CL overlay map of x = 0.8 with 1.055 eV emission colorized blue, 1.012 eV emission colorized green, and 0.936 eV emission colorized red.

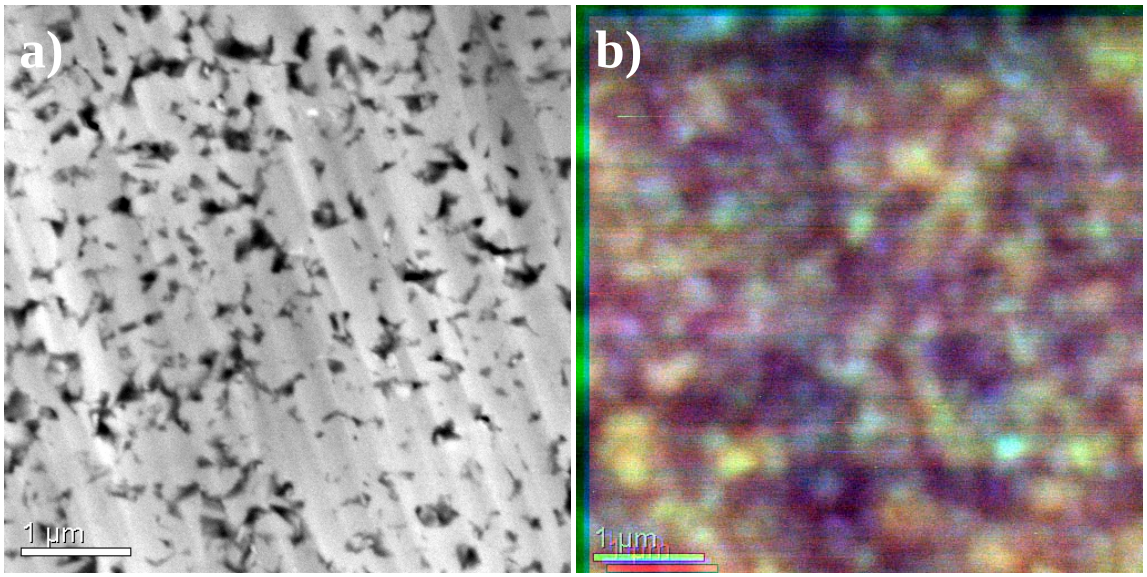

Figure 7.10. a) SEI of the area where monochromatic CL images of film x = 0.0 were acquired and overlaid to construct the CL map. b) Monochromatic CL overlay map of x = 0.0 with the 1.272 eV emission colorized blue, the 1.240 eV emission colorized green, and the 1.210 eV emission colorized red.

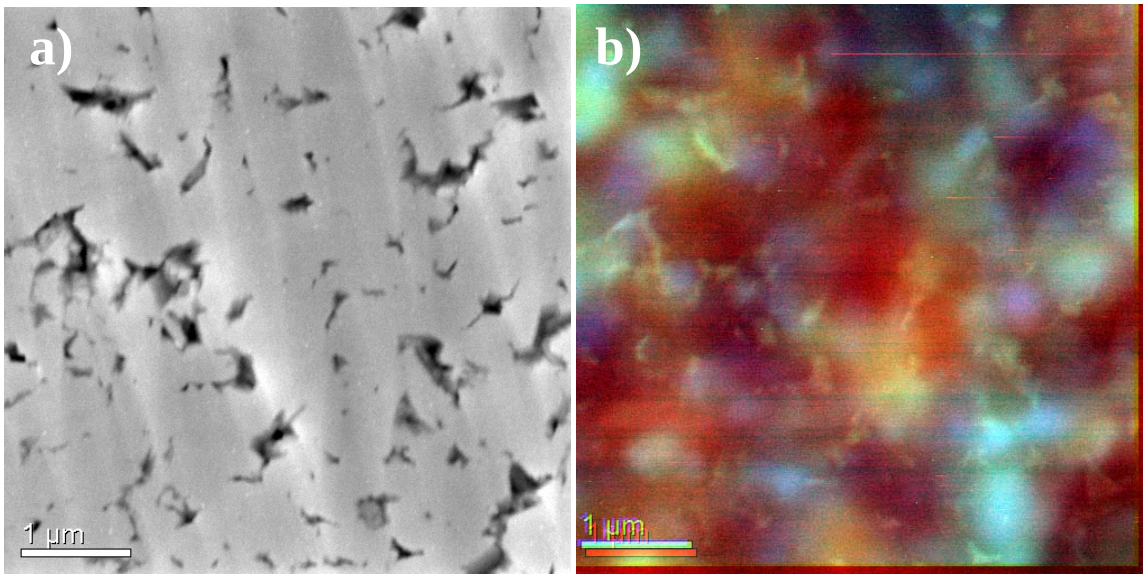

Figure 7.11. a) SEI of the area where monochromatic CL images of film x = 0.2 were acquired and overlaid to construct the CL map. b) Monochromatic CL overlay map of x = 0.2 with the 1.153 eV emission colorized blue, the 1.127 eV emission colorized green, and the 1.078 eV emission colorized red.

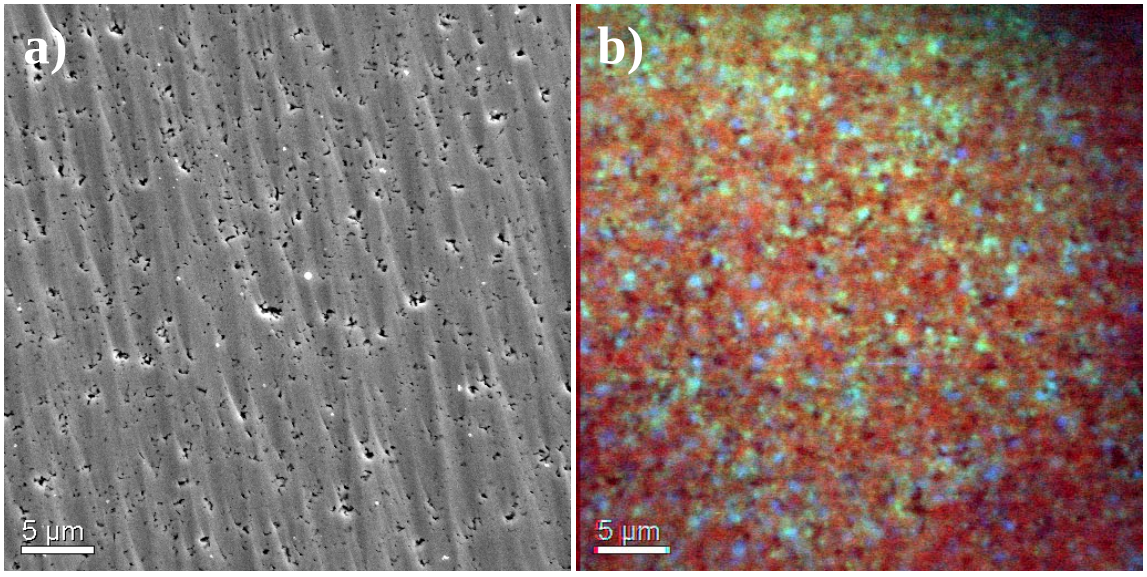

Figure 7.12. a) SEI of the area where monochromatic CL images of film $x = 1$ were acquired and overlaid to construct the CL map. b) Monochromatic CL overlay map of $x = 1$ with the 1.012 eV emission colorized blue, the 0.992 eV emission colorized green, and the 0.916 eV emission colorized red.

CHAPTER 8

$CuInSe_2$/CdS HETEROJUNCTION STABILITY

The stability of the CdS/$CuInSe_2$ (CIS) heterojunction is critical to understanding the projected lifetime of CIS devices and the effect of processing conditions on the nanoscale chemistry of the heterojunction. This chapter reports the results of annealing heterojunctions between CdS deposited by chemical bath deposition and single crystal and polycrystalline CIS films between 200 and 500°C for 10 to 150 minutes. No atomic movement was observed by secondary ion mass spectrometry at temperatures of 300°C and below. At 400°C even for the shortest time studied Cu and In were found throughout the region initially consisting of CdS only and Cd was found to have moved into the CIS. In the polycrystal, annealing at 500°C resulted in movement of Cd throughout the CIS layer. No time dependence was observed in the 400 and 500°C anneals indicating that a reaction had occurred forming a compound that was in thermodynamic equilibrium with the remaining CIS. Diffusion turns on rapidly between 300 and 400°C, indicating a high activation energy for atomic movement (~2.4 eV). The onset of diffusion is consistent with the onset of Cu diffusion in CIS.

8.1 Introduction

Increasing concerns about global energy resources coupled with significant reductions in the cost of photovoltaics are driving renewed interest in this topic [1]. The very high performance of copper chalcopyrite-based devices makes them particularly attractive candidates for detailed study [2, 3]. One of the issues that arises is the nature of the heterojunction in the devices and in particular those from which the best devices are

produced: CdS/$CuInSe_2$ (CIS) heterojunctions and similar junctions with the Ga-containing alloy Cu(In,Ga)Se_2. Various groups have studied this interface and have found evidence of reactions and surface doping. The atomic-scale structure of CdS/CIS interfaces has been examined and Cd has been found to dope the surface of $CuInSe_2$ [4, 5]. However, no significant penetration of the chalcopyrite material by Cd has been demonstrated in nanoprobe transmission electron microscopy studies [6, 7]. Reactions at the heterojunction have been demonstrated by various groups on polycrystalline layers. Primarily this has related to polycrystalline thin films suitable for devices [8-11]. Some of these studies involved only partial electrolyte treatment of the sample surface [12]. Studies of heterojunctions with single crystals have also been reported [13]. Kazmerski suggested that a device based on a single crystal epitaxial layer was limited by diffusion at the heterojunction [14]. Finally, the diffusion coefficient for Cd in CIS was studied by Rutherford backscattering examination of a metallic Cd layer on a CIS polycrystal and fitting of the results with an error function [15]. None of these studies except the latter have examined time dependent reactions as a function of temperature. Time and temperature dependence are critical to the ultimate stability of the heterojunction, particularly if it becomes necessary to heat the junction when forming a second junction, as may be necessary in some tandem device structures. It also has implications for ultimate lifetime and reliability of photovoltaic modules based on CIS.

To further address the issue of how CdS interacts with $CuInSe_2$, we have examined the reactions/diffusion of species across CdS/$CuInSe_2$ heterojunctions. In the current study a single crystal epitaxial layer of CIS grown on a GaAs substrate was used to avoid rapid diffusion along grain boundaries and to minimize surface topography

effects that make depth profiling difficult [12]. A polycrystalline CIS layer was also used for better comparison with previous results.

8.2 Experimental

A single crystal epitaxial layer of $CuInSe_2$ was grown by a hybrid sputtering and evaporation method on a (100)-oriented GaAs substrate. The deposition process has been described in detail elsewhere [16]. For consistency in the measurements a single epitaxial layer with a very smooth surface was chosen for this study. That sample was grown at 730°C for 50 minutes at a growth rate of ~1 μm/hour. The film composition as measured by energy dispersive spectroscopy was found to be 19.4% Cu, 24.1% In, 2.8% Ga, and 53.6% Se. For comparison a polycrystalline layer also grown on (100) GaAs at 720°C for 50 min was also studied. The composition of that sample was 21.5% Cu, 24.7% In, 2.2% Ga and 51.6% Se. Both the single crystal and the polycrystalline layers were ~0.75 μm thick. The samples were coated with ~25 nm of CdS by chemical bath deposition using a recipe described in Reference [17]. Following CdS deposition the samples were overcoated with SiO_2 to prevent loss of constituents during annealing. The SiO_2 was deposited by sputter deposition for the epitaxial layer and by evaporation for the polycrystalline sample.

The samples were cleaved into small pieces such that both the CIS and the CdS would be as similar as possible. Each piece was annealed face-up on a quartz boat in flowing N_2 in a tube furnace. Annealing temperatures were 200, 300, 400, and 500°C for 10, 30, 60, 90, 120, and 150 minutes. Times were from insertion to removal from the furnace so there was some heat up time in each anneal that is included in the above times.

This is not expected to have significantly affected the results reported here as temperature makes more difference than time at that temperature.

Following annealing the samples were analyzed by secondary ion mass spectrometry (SIMS) in a Cameca IMS 5f instrument using Cs^+ primary ions incident on the sample at an energy of 5.5 keV and detecting positive secondary ions ejected from the sample surface. An electron gun was used to neutralize the surface of the sample when sputtering due to the insulating characteristics of SiO_2. The depth of each profile was determined by measurement of the crater in which the analysis took place by microprofilometry using a Sloan Dektak-3 instrument.

8.3 Results

Typical composition depth profiles for the epitaxial and polycrystalline samples as deposited are shown in Figure 8.1. The SiO_2 layer is very thin and only appears in the first few data points near the surface of each sample. In this region the other signals are changing rapidly due to the large chemical change in the matrix and the onset of sputtering. Therefore the data in the region of the SiO_2 should not be considered reliable.

The CdS layer is visible where the Cd and S show a strong rise, while the CIS layer shows Cu and Se. (In is not plotted to simplify the graphs but follows the trend in the Cu signal.) The rise in the Cu signal near the heterojunction is due to an ion yield and sputtering rate change passing from the Se to the S matrix. A similar bump occurs in the In signal for the same reason. The bump in the Cu and In intensities does not correctly reflect the real Cu and In contents. The roughness of the sample surface in the case of the polycrystal reduces the effect of this yield change so the bump is not as obvious. Note

that the S, Cd, and Cu signals are all dropping together in this sample below the heterojunction, reflecting the penetration of Cd and S into the polycrystalline material [6]. The drop in the Cu signal with the drop in S is the same effect as the bump in Cu in the single crystal sample profile but spread out over the range over which the S signal dies away. The Cu signal eventually settles down to a constant level approximately 0.4 μm into the film. In both samples there is a region clear of significant Cu, In, and Se further defining the CdS layer.

When the samples were annealed the Cu, In, and Cd were found to move while the S and Se stayed in the same place. The In movement was similar to that of Cu so the remainder of this work focuses on the Cu but the In profiles were the same. Evidence for the lack of movement of S and Se can be seen by plotting the S and Se depth profiles as a function of annealing temperature and time. The normalized S and Se profiles for the epitaxial film as a function of annealing conditions are shown in Figure 8.2. Note that no significant movement of either species is observed even for annealing at 500°C for 90 minutes. The 500°C 150 minute anneal also produced no movement of the two elements. Thus the chalcogen profile at the heterojunction is highly stable. This also provides a good marker for the location of the original heterojunction.

To characterize the movement of Cu and Cd we need to deal with the ion yield change at the heterojunction. Several attempts were made to compensate for this change based on the S to Se ratio measured but no satisfactory result was obtained. We therefore use the depth profiles obtained for the as-deposited films (Figure 8.1) as a reference and compare these to the annealed sample profiles to determine if movement occurred. There was no change in the profiles within the noise in the data for the 200 and 300°C annealed

samples for any annealing time. Annealing at 400°C and 500°C produced significant movement in both the single crystal and polycrystalline samples. Figure 3 shows the depth profiles from the epitaxial single crystal sample annealed at 200°C for 90 minutes and the sample annealed at 500°C for the same time. The profiles show movement of Cu and In from near the heterojunction in the CIS into the CdS and Cd movement in the opposite direction when annealed at 500°C but not at 200°C.

The movement of Cd, In, and Cu was found to be time independent for most of the annealing conditions studied. For temperatures of 300°C or below, no movement of any element was found above uncertainty in the data. The epitaxial sample behaved somewhat differently from the polycrystalline sample under higher temperature anneals. At 400°C for times longer than 10 minutes, Cu and In were found to diffuse completely through the CdS leaving a Cu-deficient layer near the surface of the CIS for both samples. In the 10 minute anneal this diffusion process was not complete for the epitaxial layer and further movement was found for longer anneals. The data is not sufficiently clear to extract a reliable diffusivity and only this single data point (400°C, 10 minutes) showed any time dependence. Cd was found to move into the Cu/In deficient region of the CIS, replacing the lost Cu/In which had moved into the CdS layer. In the polycrystalline sample, outdiffusion of Cu/In was observed at 400°C for 10 minutes or longer, which did not change with time. At 500°C more extensive outdiffusion of Cu and In were observed, again without time dependence.

Plots of composition profiles for the polycrystalline sample are given in Figure 8.4. Significant diffusion of Cd was not observed at 400°C in the polycrystalline sample. At 500°C the Cd was found to have diffused rapidly into the bulk of the CIS layer and

was distributed uniformly throughout the depth of the layer. The behavior of In matches that of Cu. The differences in behavior in the polycrystal relative to the single crystal are probably mostly associated with grain boundary diffusion coupled with the roughness of the surface, which has the effect of averaging the signal observed by SIMS over various depths.

The absence of further atomic movement at 400 and 500°C for increasing anneal times indicates that the resulting Cu and Cd distributions (Figure 8.3b) are in equilibrium for that temperature. The interpretation is that the observed distribution should represent a specific stable $(CuIn)_xCd_{1-x}Se$ phase. X-ray diffraction analysis of the annealed samples showed evidence of a new $Cu_{0.75}Cd_{0.5}In_{0.75}Se_2$ phase for the sample annealed at 500°C for 90 min. The unannealed sample showed only the $CuInSe_2$ and GaAs phases (the CdS peaks overlap with the CIS peaks so they cannot be distinguished separately). The XRD spectra are shown in Figure 8.5. Energy dispersive x-ray spectroscopy (EDS) measurements were also performed on the annealed film. The composition after annealing was 16.8% Cu, 19.5% In, 2.2% Ga, 36.7% Se, 11.3% Cd, and 13.4% S. Assuming 80% of the Cd is now in the original $CuInSe_2$ layer (which is reasonable based on the Cd depth profile), that a respective amount of Cu and In are now in the original CdS layer and normalizing these compositions, a compound with $Cu_{0.65}Cd_{0.49}In_{0.79}Ga_{0.12}(S+Se)_{1.95}$ is obtained. These values obtained from EDS are in close agreement with the $Cu_{0.75}Cd_{0.5}In_{0.75}Se_2$ phase observed by x-ray diffraction.

8.4 Discussion

Many authors have referred to "diffusion" of Cd in CIS. From the current work we can estimate a diffusivity range for Cu in CdS containing sufficient cation vacancies (as it replaces moving Cu or In). At 300°C for 150 minutes Cu or In would have had to have moved less than ~10% of the thickness of the CdS (~2.5 nm) to be undetectable by SIMS. At 400°C to have moved completely through the CdS the diffusion distance would have had to have been significantly more than 25 nm in 10 minutes. Taking the diffusion distance, x, as $x = (Dt)^{1/2}$ where D is the diffusivity and t is the time, and solving for D, $D = x^2/t$, the maximum diffusivity at 300°C would have to be less than $1x10^{-17}$ cm^2/sec. The minimum diffusivity at 400°C would have to be greater than $1.5x10^{-14}$ cm^2/sec. To obtain this difference in diffusivity over 100°C would imply an activation energy for diffusion of Cu and In in CdS of greater than 2.4 eV. This magnitude of activation energy is common in diffusion of impurities in typical semiconductors by a substitutional mechanism. Because Cd diffusion turns on in nearly the same temperature range in both samples, the diffusion activation energy for Cd in CIS would have to be approximately the same in single and polycrystalline materials.

The estimated values for diffusivities are much smaller and for diffusion activation energy much larger than the previous reported diffusivity for Cd in CIS [15]. If the prior work were correct we should have seen Cd diffusion into the CIS even at 200°C when annealed for 150 minutes with a detectable variation in observable diffusion of Cd into the CIS at 200°C for the various anneal times. We conclude from our results that diffusion is much slower than reported by Kumar. This is not necessarily

inconsistent with the prior work as that experiment was very different. In the current work we diffused Cd from CdS into single crystal and polycrystalline CIS and measured the results by SIMS. In the earlier work the Cd was metallic, which would result in a strong reaction with the chalcopyrite CIS resulting in a large number of Se vacancies in the material and a very different point defect density. Furthermore the Rutherford backscattering analysis has a variety of complications involved in the data interpretation. The 0.47 eV activation energy for diffusion in the earlier work is also more consistent with an interstitial rather than a substitutional diffusion mechanism. Therefore we consider our results distinct from the prior work.

In the current work we find that the diffusion of Cd is coupled to the diffusion of Cu and In. All of the chalcogen compounds have a very strong tendency to valence compensate. Counterdiffusion of Cu and In and Cd would tend to result in a net exchange of one In and one Cu for two Cd atoms. This is precisely what we observe in the XRD data showing the final compound to be $Cu_{0.75}Cd_{0.5}In_{0.75}Se_2$. Our observation that the diffusion of Cd, Cu and In resulting in the formation of a $(CuIn)_xCd_{1-x}Se$ compound is consistent with the previous work by Heske *et.al* who found compound formation by photoelectron spectroscopy but did not investigate the time or temperature dependence of the reaction [8].

Based on the annealing conditions studied here I conclude that no true diffusion [i.e $x = (Dt)^{1/2}$ driven by a concentration gradient] of any significance of Cd, Cu or In can occur under conditions of chemical bath deposition (maximum 75°C) or under conditions where air annealing of the heterojunction is performed by some groups (200°C). Any long-range transport of these atoms begins at much higher temperatures, around 400°C,

and may result in the rapid formation of $Cu_{0.75}Cd_{0.5}In_{0.75}Se_2$ rather than extended transport of atoms into the bulk of the CIS. It is possible that a few atomic layers of atomic exchange may occur at 200°C but if that is the case it is not detectable by any of the methods employed here.

8.5 Conclusions

I conclude that CdS/CIS interfaces are chemically stable at temperatures below ~400°C, although short range transport of atoms over distances too small (monolayers) to measure by the techniques used here may be responsible for degradation of devices observed when annealed above 200°C. The S and Se profiles across the heterojunction are highly stable even at 500°C for 150 minutes. However, above 400°C, Cu and In begin to diffuse out into the CdS layer. To valence compensate for the loss of these elements from the CIS, Cd moves in to the vacated locations but does not diffuse effectively in the bulk of the CIS. However, Cd can diffuse relatively rapidly along grain boundaries in the polycrystalline material. The diffusion results in formation of a stable phase, $Cu_{0.75}Cd_{0.5}In_{0.75}Se_2$.

8.6 References

[1] R. Gillette, in First Solar quarterly report, First Solar, Phoenix AX, 2010.

[2] ZSW, in press release, 2010.

[3] I. Repins, M. A. Contreras, B. Egaas, C. DeHart, J. Scharf, C. L. Perkins, B. To, and R. Noufi, Progress in Photovoltaics: Research and Applications 16 (2008) 235.

[4] Y. L. Soo, S. Huang, Y. H. Kao, S. K. Deb, K. Ramanathan, and T. Takizawa, Journal of Applied Physics 86 (1999) 6052.

[5] D. X. Liao and A. Rockett, Journal of Applied Physics 93 (2003) 9380.

[6] C. Lei, M. Duch, I. M. Robertson, and A. Rockett, Journal of Applied Physics 108 (2010) 114908.

[7] T. Nakada, Vol. 361-362, Elsevier, Switzerland, 2000, p. 346.

[8] C. Heske, D. Eich, R. Fink, E. Umbach, B. T. Van, C. Bostedt, L. J. Terminello, S. Kakar, M. M. Grush, T. A. Callcott, F. J. Himpsel, D. L. Ederer, R. C. C. Perera, W. Riedl, and F. Karg, Applied Physics Letters 74 (1999) 1451.

[9] H. Wiesner, J. Keane, K. Ramanathan, M. Contreras, and R. Noufi, United States, 1998, p. 9p.

[10] B. M. Basol and V. K. Kapur, in 10th Photovoltaic Advanced Research and Development Project Review Meeting, 23-25 Oct. 1990, Vol. 30, Switzerland, 1991, p. 143.

[11] P. Hailin, X. Chong, D. T. Schoen, K. McLlwrath, Z. Xiao Feng, and C. Yi, Nano Letters 7 (2007) 3734.

[12] S. E. Asher, K. Ramanathan, D. W. Niles, H. Wiesner, and H. Moutinho, in NCPV Photovoltaics Program Review. 15th Conference, 9-11 Sept. 1998, AIP, USA, 1999, p. 126.

[13] F. A. Abou-Elfotouh, L. L. Kazmerski, T. J. Coutts, R. J. Matson, S. E. Asher, A. J. Nelson, and A. B. Swartzlander-Franz, in 35th National Symposium of the American Vacuum Society, 2-7 Oct. 1988, Vol. 7, USA, 1989, p. 837.

[14] L. L. Kazmerski, United States, 1976, p. 58p.

[15] A. P. Kumar and K. V. Reddy, Semiconductor Science and Technology 12 (1997) 966.

[16] A. Rockett, T. C. Lommasson, L. C. Yang, H. Talieh, P. Campos, and J. A. Thornton, in Conference Record of the Twentieth IEEE Photovoltaic Specialists

Conference - 1988 (Cat. No.88CH2527-0), 26-30 Sept. 1988, IEEE, Las Vegas, NV, USA, 1988, p. 1505.

[17] M. A. Contreras, M. J. Romero, B. To, F. Hasoon, R. Noufi, S. Ward, and K. Ramanathan, Thin Solid Films 403-404 (2002) 204.

8.7 Figures

(a)

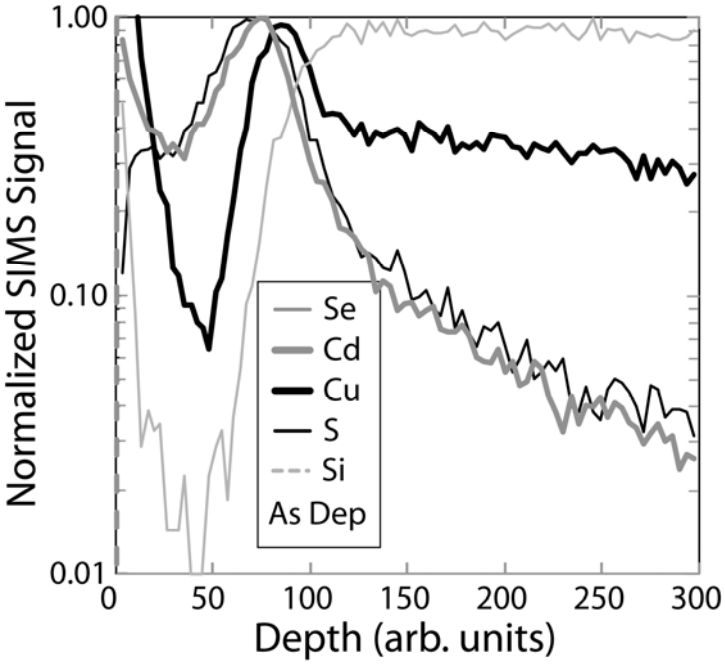

(b)

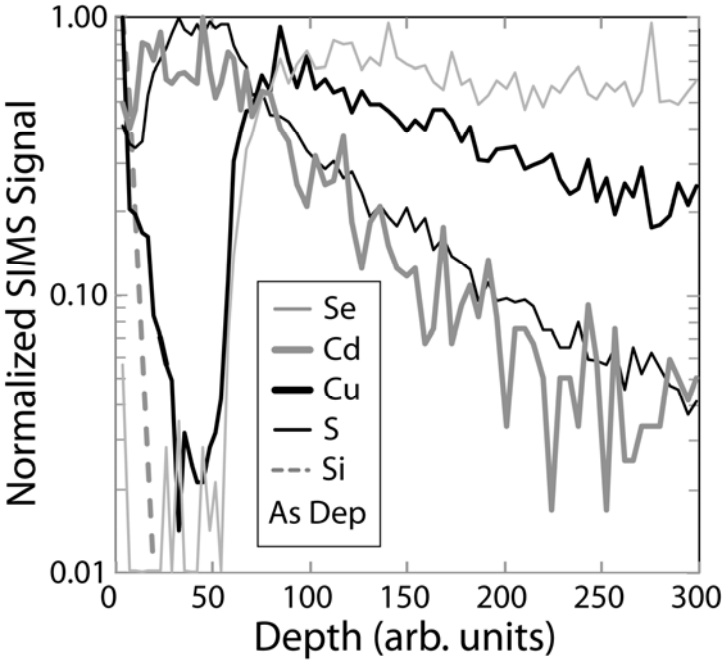

Figure 8.1: Composition depth profiles near the sample surface for (a) the epitaxial and (b) the polycrystalline sample with CdS and SiO_2 coating as deposited.

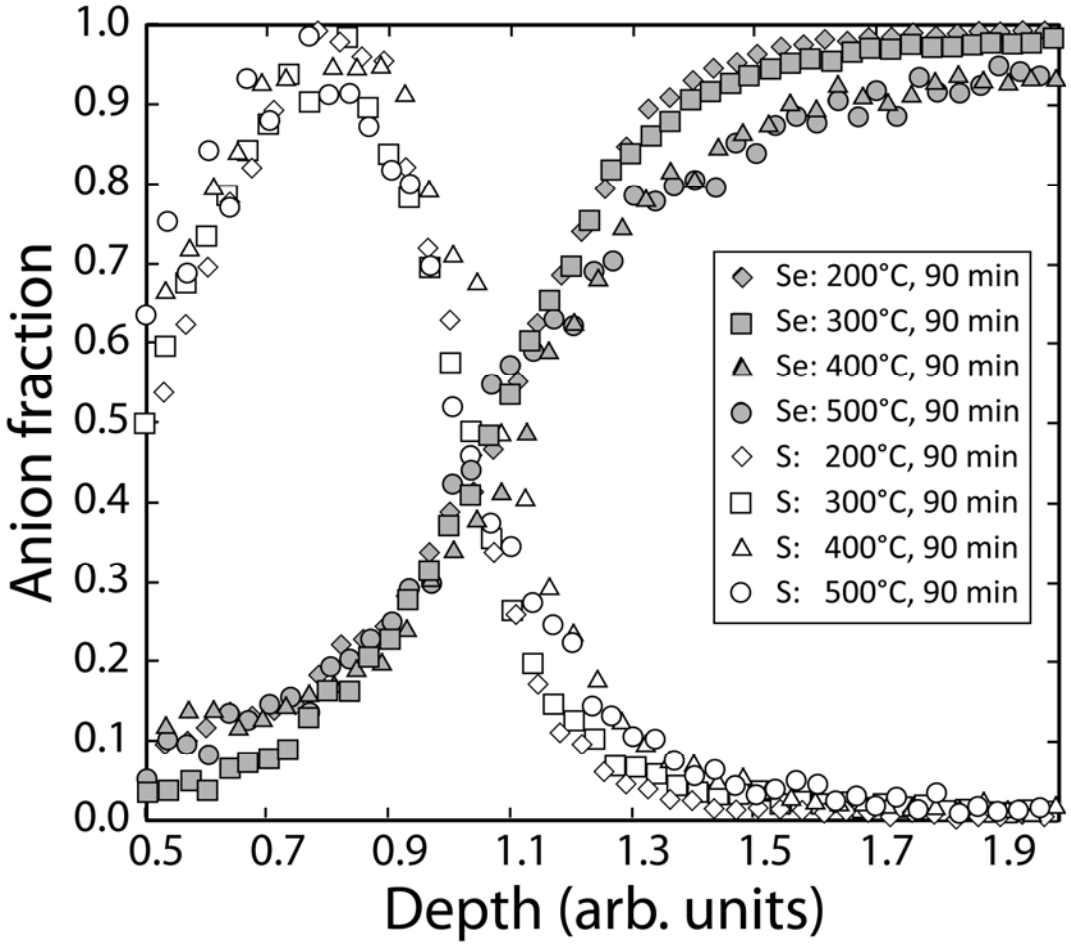

Figure 8.2: Shows the S and Se signals across the heterojunction after annealing at four temperatures for 90 minutes each. Further annealing produced no additional movement of atoms. The polycrystalline sample showed similar behavior.

(a)

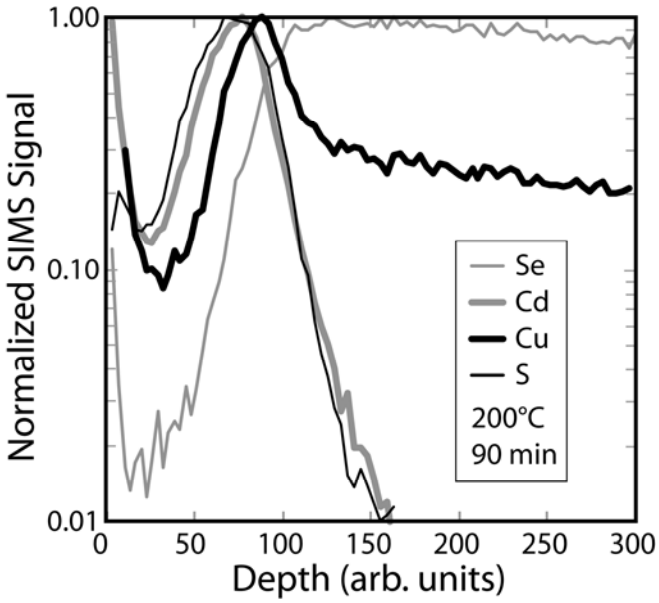

(b)

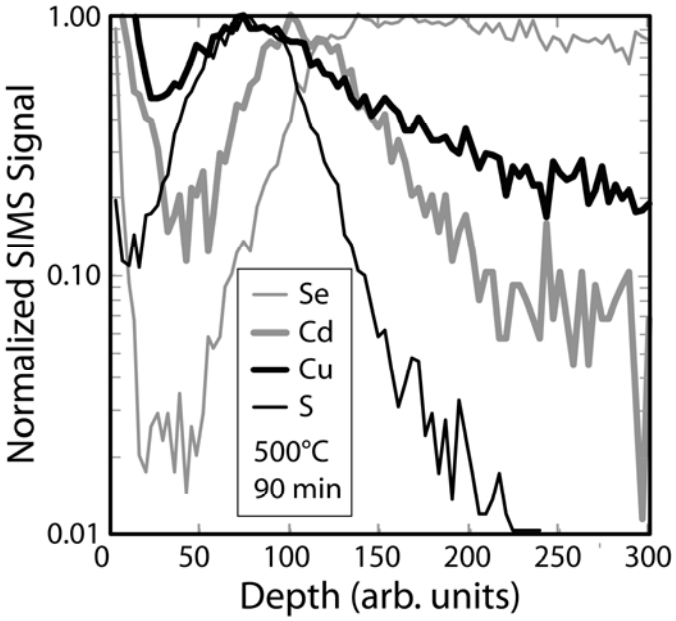

Figure 8.3: Shows the composition depth profiles of the epitaxial film annealed (a) at 200°C for 90 minutes and (b) at 500°C for 90 minutes. The Se and S profiles are unchanged. The peak in the Cu signal has moved outward and Cd has moved inward during annealing at 500°C. No significant difference was observed between the sample heated to 200°C for 90 minutes and the as-deposited profile.

(a)

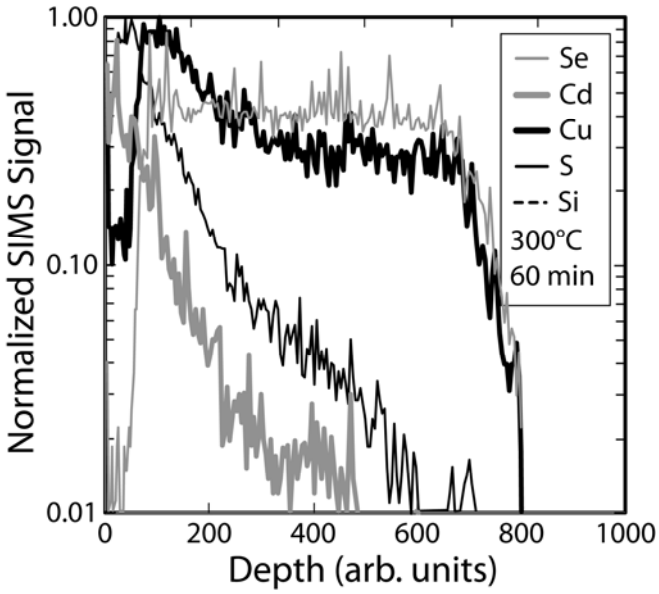

(b)

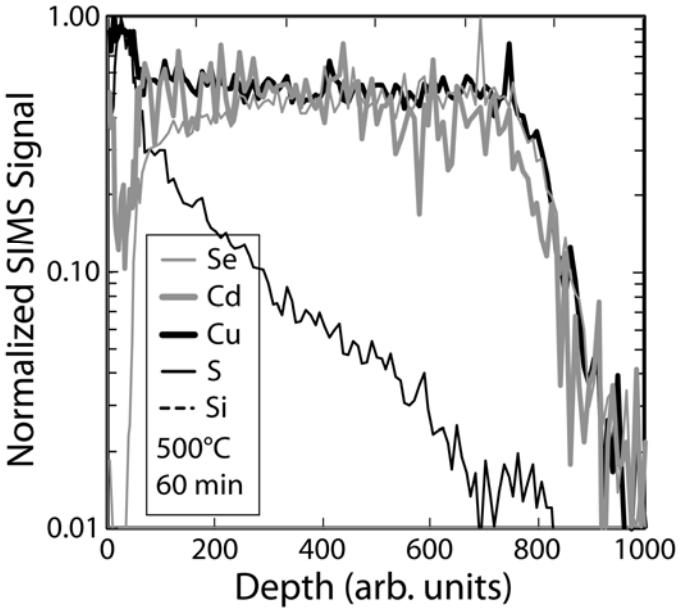

Figure 8.4: Shows the composition depth profile for the polycrystalline sample annealed at (a) 300°C for 60 minutes and (b) 500°C for 60 minutes. The profile in (a) is the same, to within noise in the data, to the profile shown in Figure 8.1b. Note the diffusion of Cd through the entire CIS layer in the higher temperature anneal while no movement of S or Se is observed.

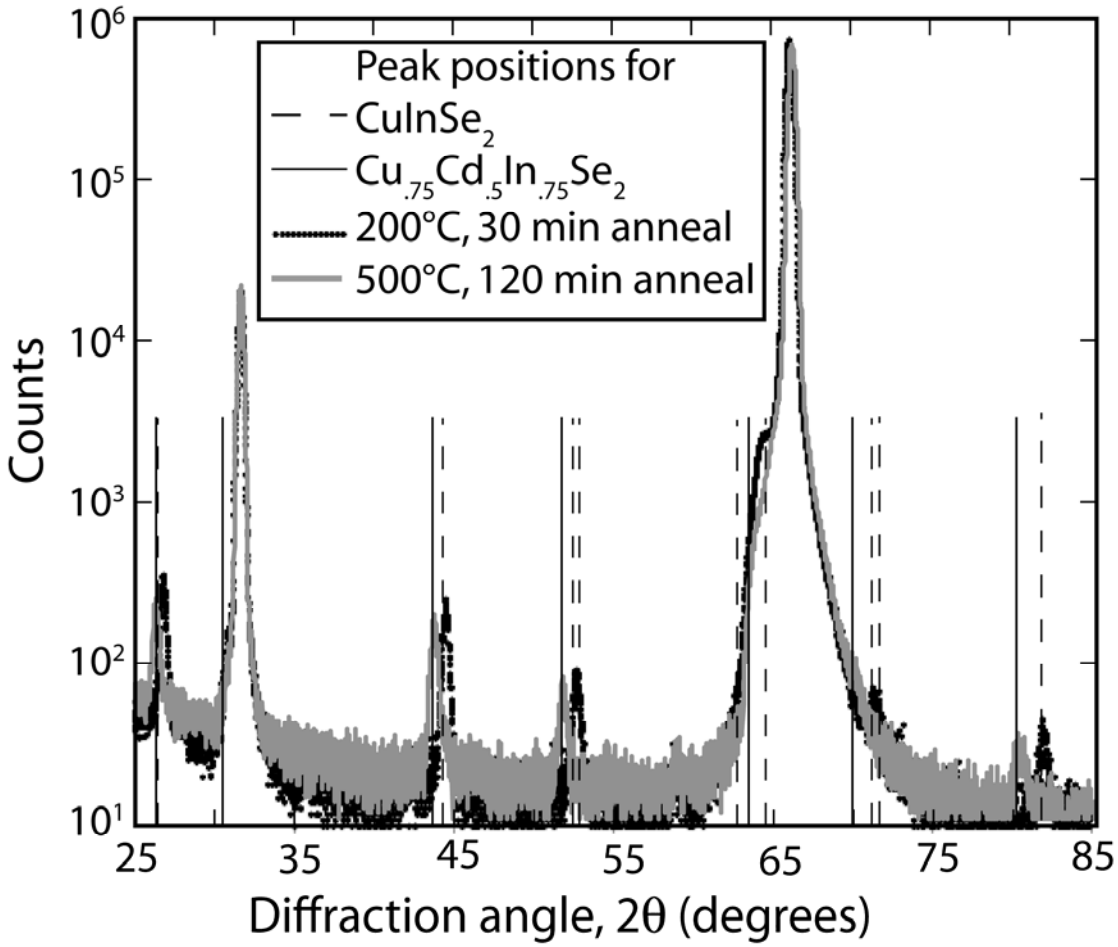

Figure 8.5: X-ray diffraction data for two films, after a 200°C 30 minute anneal and after a 500°C, 120 minute anneal. The peak positions for the major diffraction peaks for chalcopyrite $CuInSe_2$ and $Cu_{.75}Cd_{.5}In_{.75}Se_2$ are marked. The major peaks at ~27 and 66 degrees are due to the GaAs substrate. The other peaks fit very well with those of $CuInSe_2$ for the 200°C, 30 minute annealed sample and with $Cu_{0.75}Cd_{0.5}In_{0.75}Se_2$ for the high temperature annealed sample.

CHAPTER 9

CONCLUSIONS

9.1 Conclusions and Outlook

The main purpose of this dissertation was to study and advance the understanding of a thin film material system with the potential to yield high-efficiency solar cells. In this work, I have conducted a detailed characterization of the structural and optoelectronic properties of $Cu_xAg_{1-x}InSe_2$ alloy thin films. Polycrystalline thin films at composition intervals of $x = 0.2$ and deposited on various substrates were studied. I showed that films with compositions of $x \leq 0.2$ tend to show an ordered defect compound (ODC) towards the surface of the films. The presence of this ODC was found to have an effect on the radiative defects in the films, with film $x = 0.2$ exhibiting much broader peaks than its other Ag-dominant films.

All films showed (112) preferred orientation with the exception of films deposited on bare glass with $x \geq 0.8$, which showed a (220)/(204) preferred orientation. Films deposited on Mo-coated glass exhibited increasing grain sizes for increasing values of the (112)/[(220)/(204)] peak ratios. No beneficial effects to grain size were observed from the presence of Na in films with $x \leq 0.6$. However, for $x \geq 0.8$, films with Na showed a doubling of grain size relative to those without Na. This implies that Na does not provide the same effects in $AgInSe_2$ as it does in $CuInSe_2$.

One of the important questions answered by this research was the identification and behavior of defect levels in the alloy as a function of composition. I proposed a band diagram schematic of the defect levels in the films, which could serve as a blueprint for improvements of the films properties through defect engineering. The intrinsic shallow

defects I have identified determine the doping in these films, and hence the carrier concentrations, conductivities, and mobilities. Donor-acceptor pair transitions were observed in the films as well as free-to-bound transitions. Films with $x \geq 0.6$ exhibited only DAP transitions. However, as Ag was added, FB transitions were observed in the samples, indicating more ordering in the films. Two donor levels (20-30 meV and 60 meV) and three acceptor levels (20-35 meV, 70-110 meV, and 170-190 meV) were identified in the films. Specific defect levels did not change position relative to their respective band edges as the alloy was changed, suggesting that the defect states are derived from the Bloch states of the solid (hydrogenic) rather than being highly localized on defects. Very Ag-dominant films ($x \leq 0.4$) showed the sharpest luminescence peaks, suggesting improved crystalline quality; however they also exhibited two exponential tails, one of which extended deep into the forbidden gap (~ 0.74 eV). A continuum of defects this deep into the gap could promote recombination and limit solar cell efficiency.

The films exhibited lifetimes comparable or higher than $CuInSe_2$ for compositions up to $x \geq 0.2$, which also indicates an increase in material quality. Longer lifetimes could lead to better carrier collection and higher efficiencies in solar cells. The emissions were studied as a function of sample composition and relative position to grain boundaries. The $AgInSe_2$ sample showed more uniform luminescence both spatially and spectrally than Cu-containing samples. $AgInSe_2$ was also less affected by reduced emission from surface features, presumably due to less surface recombination. Cu-containing samples exhibited enhanced luminescence from grain boundaries or inter-grain areas, indicative of compositional or electrically-active defect fluctuations. The relatively uniform luminescence from the $AgInSe_2$ sample suggests that this material may produce more

uniform cell performances, because reduced fluctuations in chemical composition and band structure from one location to another would result in more efficient energy collection.

Finally, the stability of the $CuInSe_2$/CdS heterojunction was studied via thermal annealing experiments. Results showed that the heterojunction was stable for temperatures under 400 °C. Past this point, significant diffusion of Cu, Cd, and In was observed. However, no time dependence was observed in the 400 and 500°C anneals indicating that a reaction had occurred forming a compound that was in thermodynamic equilibrium with the remaining CIS. This compound was identified via x-ray diffraction as $Cu_{0.75}Cd_{0.5}In_{0.75}Se_2$. These results suggest that lower deposition temperatures are needed for deposition of any potential top junctions that are used in combination with the $CuInSe_2$/CdS heterojunction.

In summary, I have shown the effects of alloying Ag with $CuInSe_2$. I showed that adding Ag appears to improve the structural quality of the films. This was seen by a reduction in the FWHM of the PL peaks, a reduction in the number of optical transitions, and the appearance of free-to-bound transitions for Ag-dominant films. An increase in the minority carrier lifetime of films with the addition of Ag also supports this conclusion. Furthermore, AIS films showed less spatial and spectral variations than Cu-containing films in CL measurements, indicating less heterogeneity in the material. Cu-dominant films appear to be dominated by the shallow acceptor V_{Cu}, as seen by the p-type conductivity obtained via Hall effect measurements. Ag-dominant films showed n-type conductivity indicating that the dominant defects are now the shallow donors, likely In_{Ag} antisite defect.

These results suggest that the $Cu_xAg_{1-x}InSe_2$ alloy is a suitable candidate for higher bandgap solar cells. However, various issues must still be resolved in order to make the entire compositional alloy space usable for solar cells. These are listed below:

1. Obtain p-type conducting $AgInSe_2$ films. Film conductivity changes from p-type to n-type as we go from $CuInSe_2$ to $AgInSe_2$. This change occurs at values between $0.2 < x < 0.4$. p-type films are typically preferred because of the n-type heterojunction partner, CdS.
2. Elimination of the observed ordered defect compound in films with $x \leq 0.2$. This additional phase has different structural and optical properties from $AgInSe_2$ and could potentially limit device performance.
3. Elimination of the continuum of defects that extends deep into the band gap. This could lead to an increase in recombination thereby reducing the amount of carriers collected and the efficiency of solar cells.

9.2 Future Research

Therefore, based on these unresolved issues, I recommend the following topics as subjects for future study of this alloy:

1. Detailed surface studies of the $AgInSe_2$ alloy in order to study the effects of the observed ordered defect compound.
2. Systematic study and characterization of a $AgInSe_2$/CdS heterojunction in order to understand better the interaction between the two layers.
3. Growth of epitaxial layers of $Cu_xAg_{1-x}InSe_2$ in order to study growth phenomena in a more controlled way.

4. Growth of polycrystalline $Cu_xAg_{1-x}InSe_2$ thin films on Mo-coated borosilicate glass in order to study the effects of Na vs. no Na on Mo-coated substrates.
5. Fabrication of devices consisting of $Cu_xAg_{1-x}InSe_2$ layers in order to relate optoelectronic defects to device performance.
6. Detailed electrical characterization that includes identification of deep defects in the films via capacitance methods.

APPENDIX A

SUPPLEMENTAL FIGURES

A.1 Scanning Electron Microscopy Images

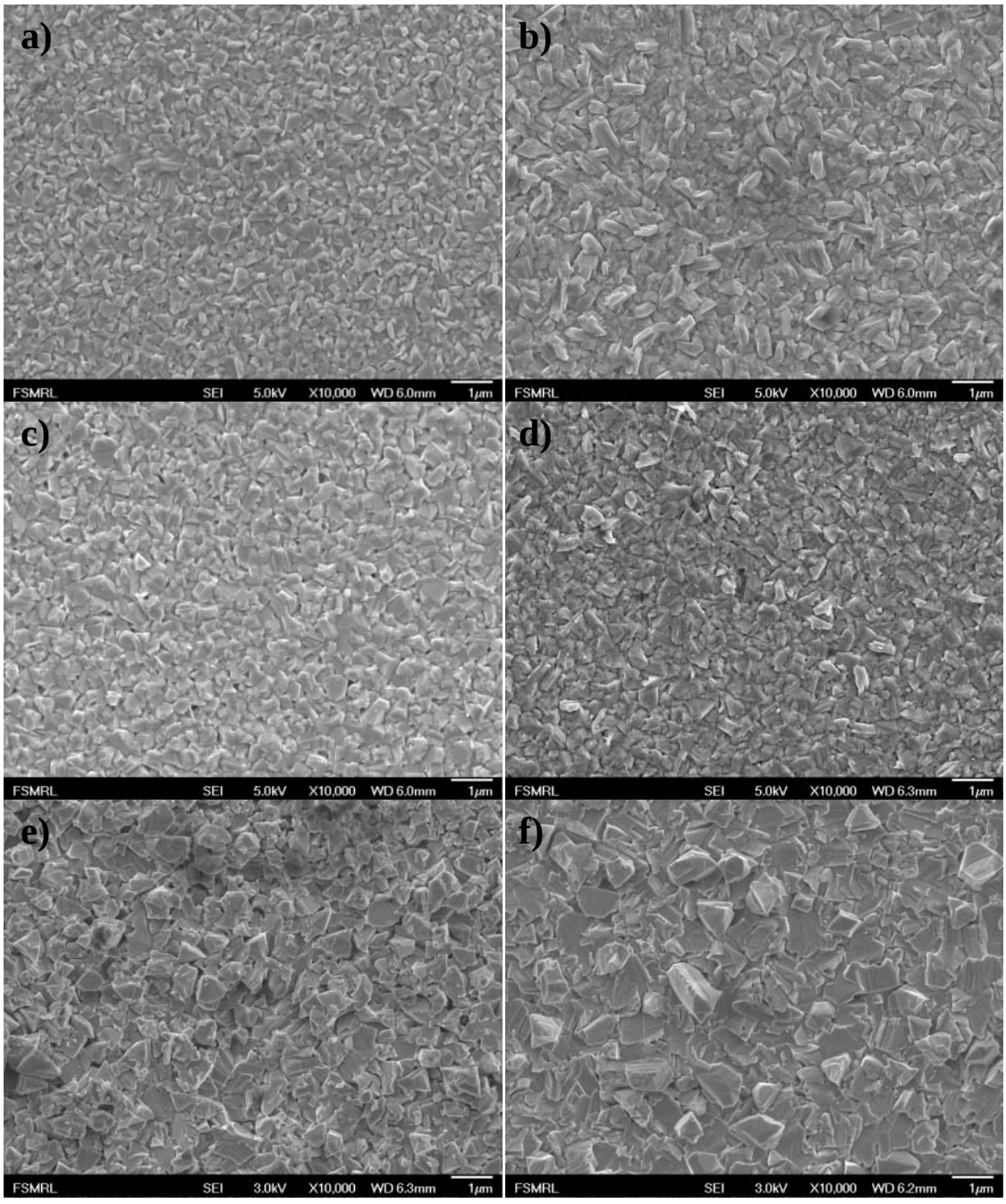

Figure A.1. SEM images of $Cu_xAg_{1-x}InSe_2$ thin films on bare soda-lime glass substrates. a) $x = 0$, b) $x = 0.2$, c) $x = 0.4$, d) $x = 0.6$, e) $x = 0.8$, and f) $x = 1$.

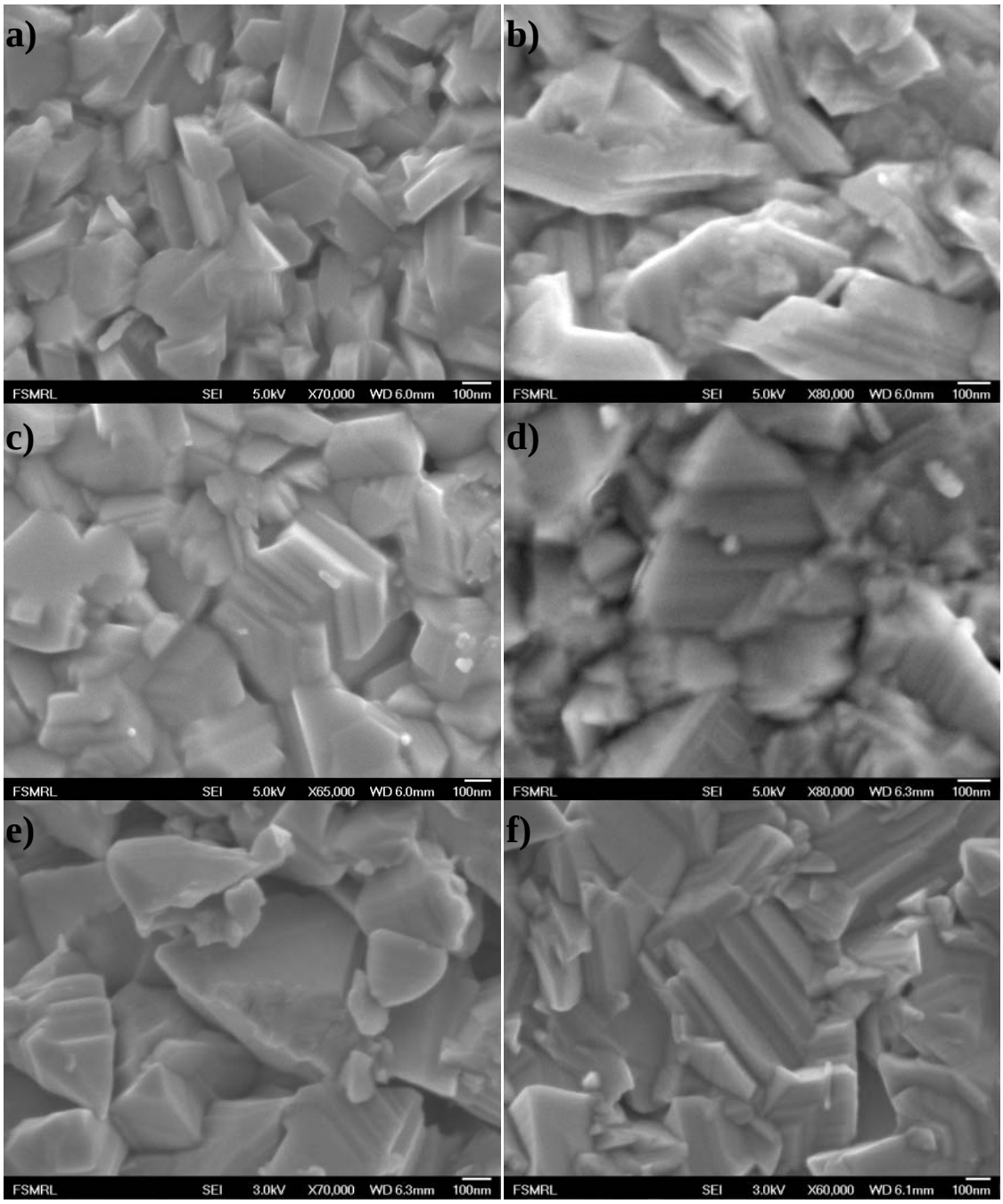

Figure A.2. High magnification SEM images of $Cu_xAg_{1-x}InSe_2$ thin films on bare soda-lime glass substrates. a) $x = 0$, b) $x = 0.2$, c) $x = 0.4$, d) $x = 0.6$, e) $x = 0.8$, and f) $x = 1$.

A.2 Photoluminescence Spectra

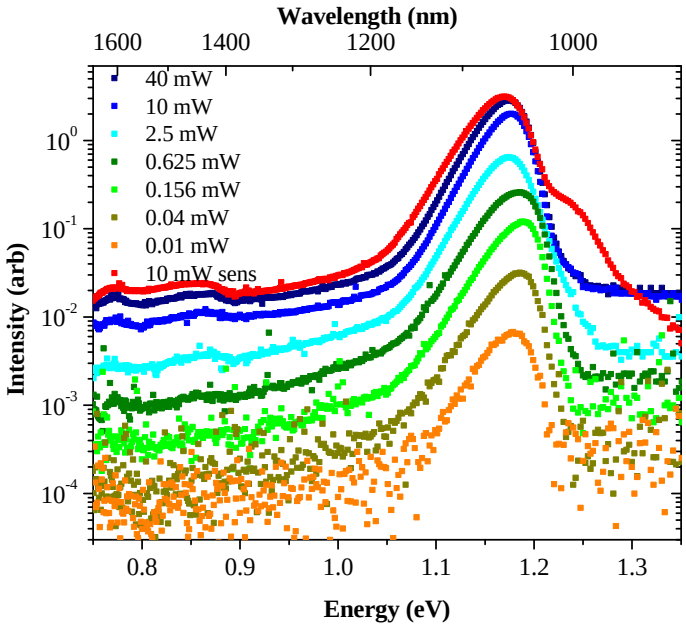

Figure A.3. Power-dependent photoluminescence spectra for film $x = 0$ taken at 10 K.

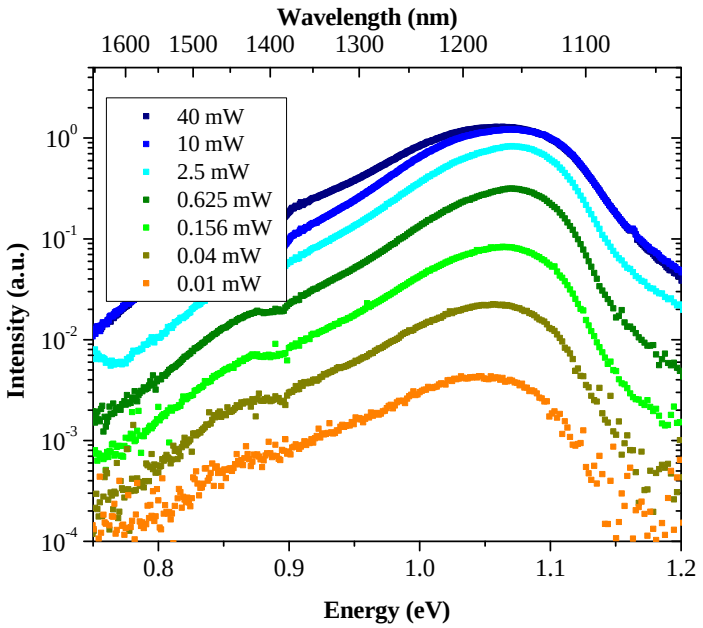

Figure A.4. Power-dependent photoluminescence spectra for film $x = 0.2$ taken at 10 K.

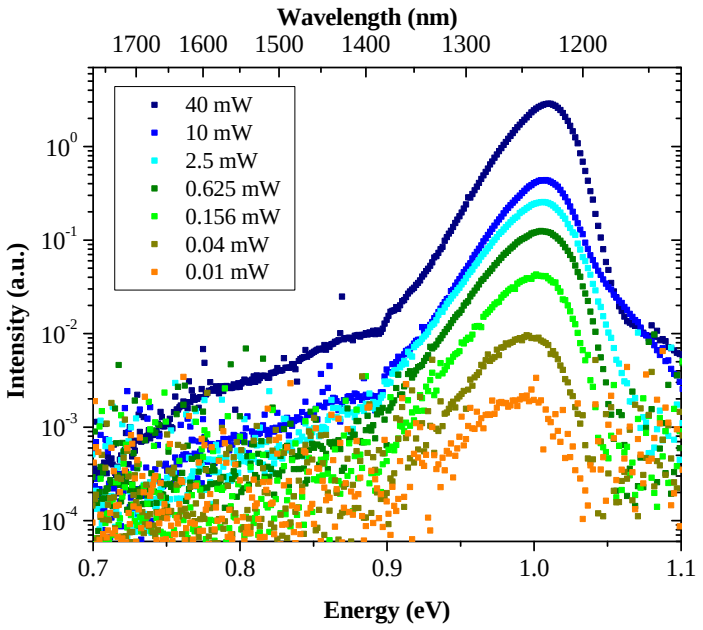

Figure A.5. Power-dependent photoluminescence spectra for film x = 0.4 taken at 10 K.

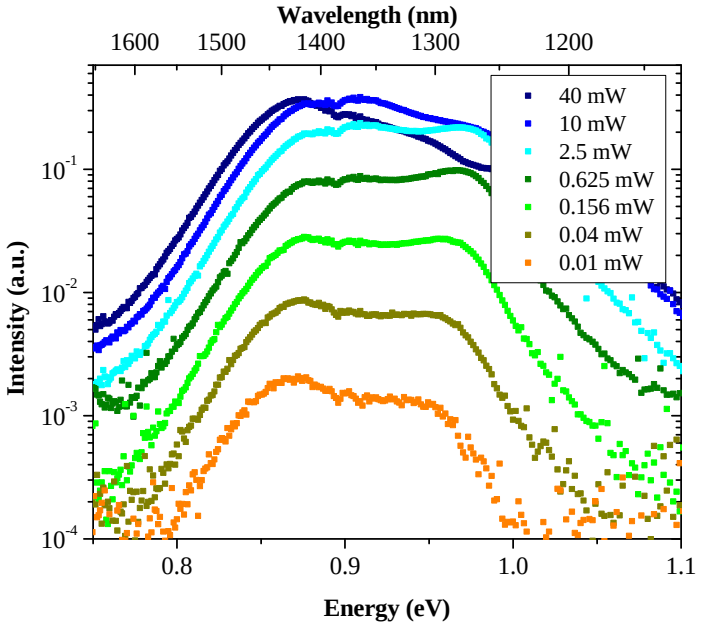

Figure A.6. Power-dependent photoluminescence spectra for film x = 0.6 taken at 10 K.

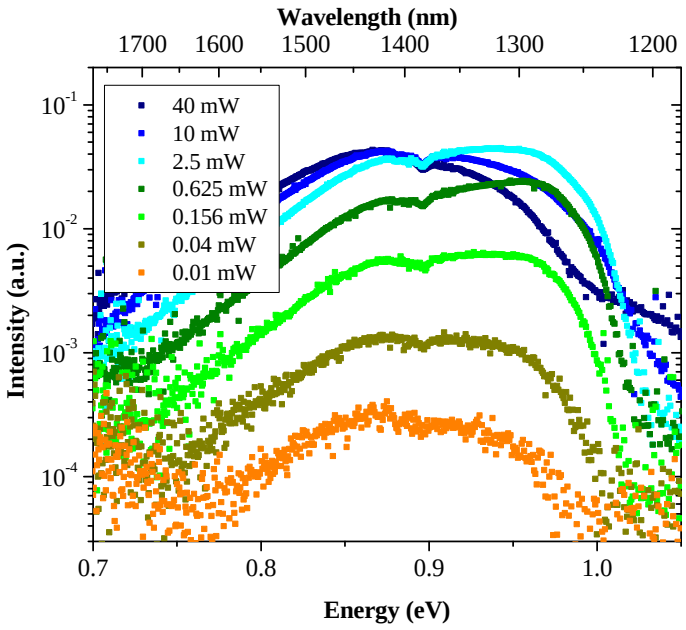

Figure A.7. Power-dependent photoluminescence spectra for film x = 0.8 taken at 10 K.

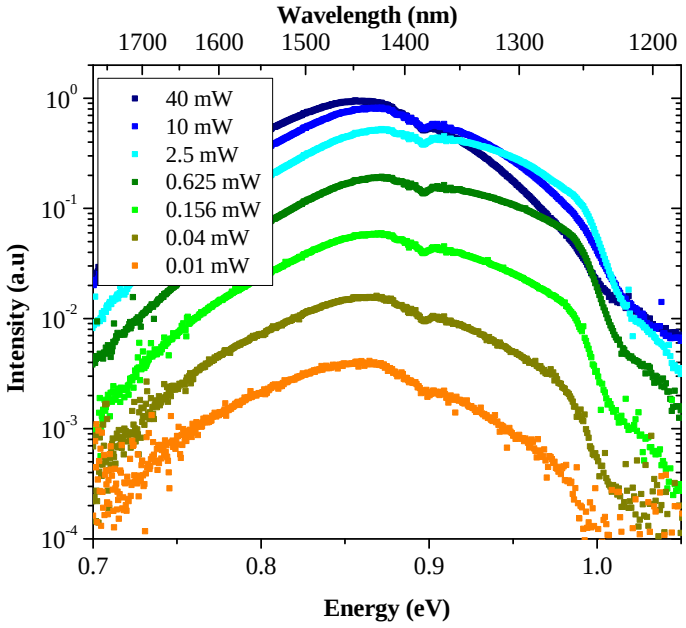

Figure A.8. Power-dependent photoluminescence spectra for film x = 1 taken at 10 K.

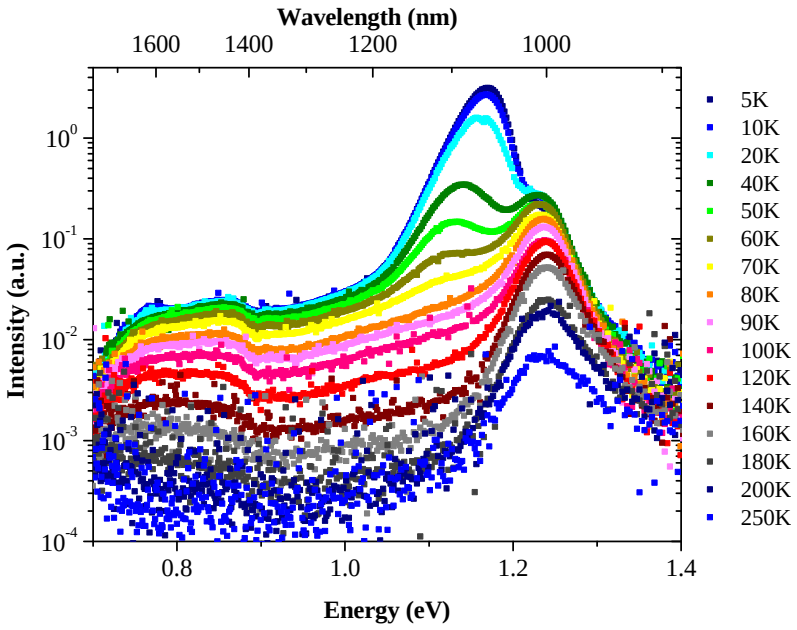

Figure A.9. Temperature-dependent photoluminescence spectra for film x = 0 taken at 10 mW.

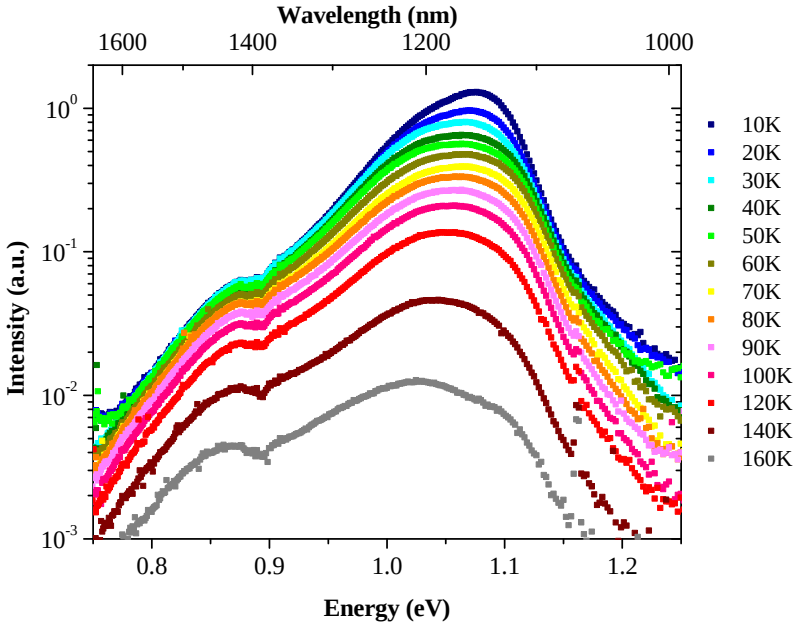

Figure A.10. Temperature-dependent photoluminescence spectra for film x = 0.2 taken at 10 mW.

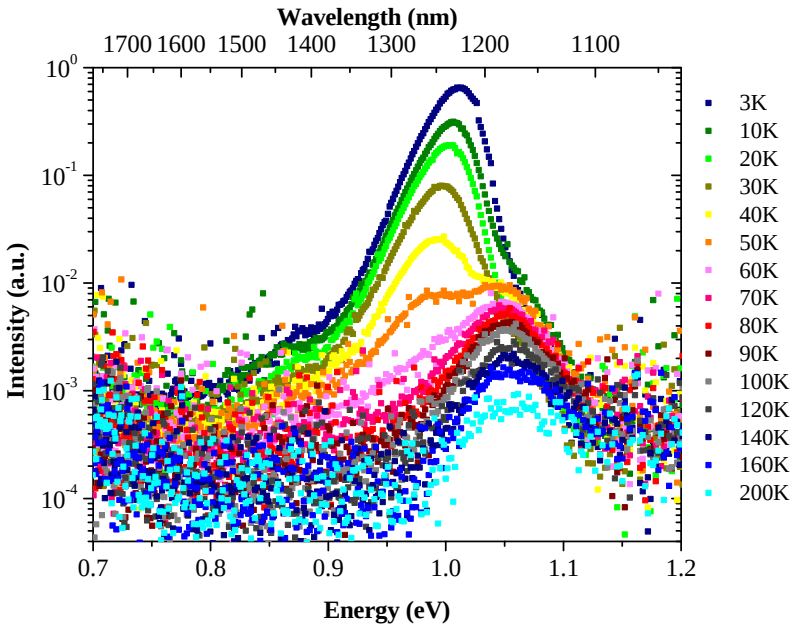

Figure A.11. Temperature-dependent photoluminescence spectra for film x = 0.4 taken at 10 mW.

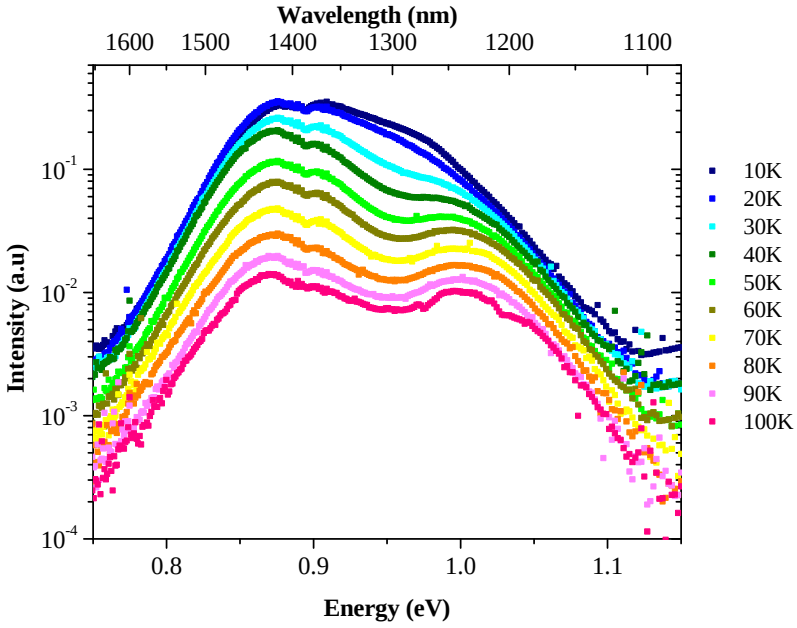

Figure A.12. Temperature-dependent photoluminescence spectra for film x = 0.6 taken at 10 mW.

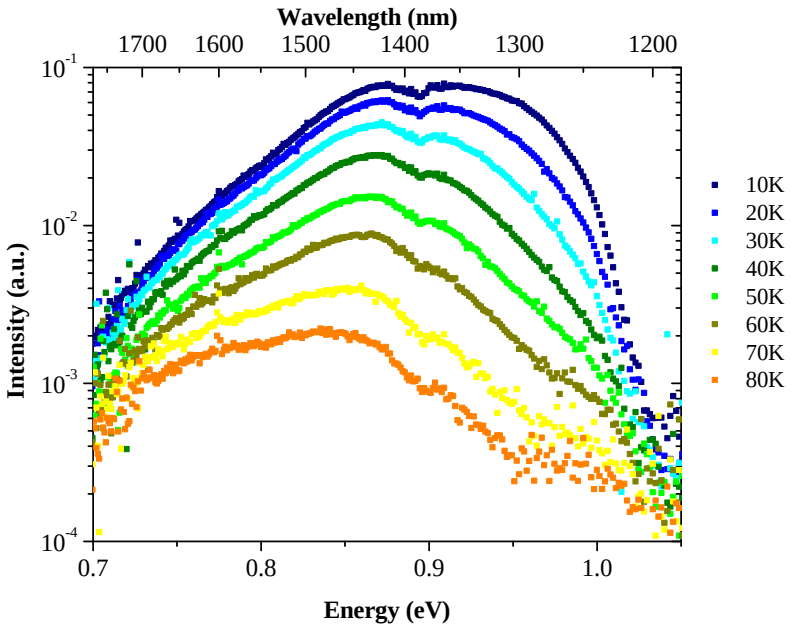

Figure A.13. Temperature-dependent photoluminescence spectra for film x = 0.8 taken at 10 mW.

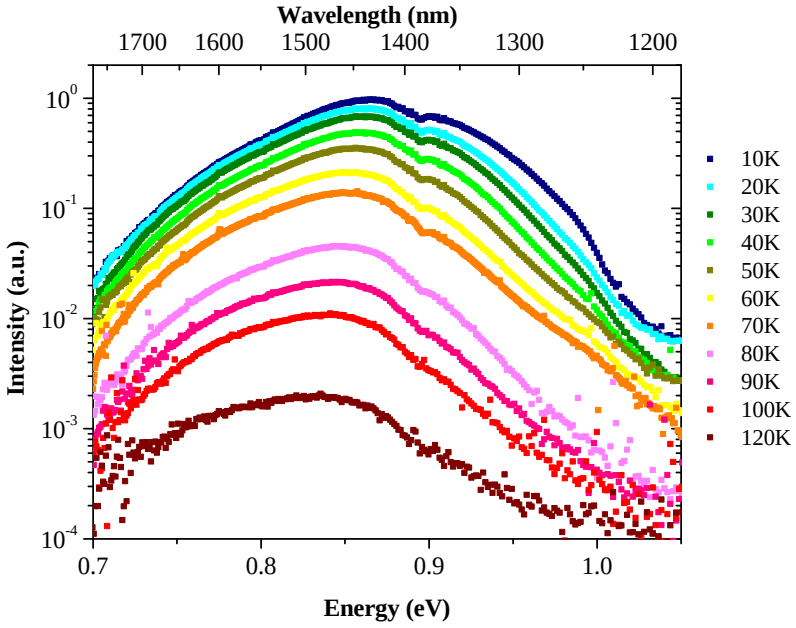

Figure A.14. Temperature-dependent photoluminescence spectra for film x = 1 taken at 10 mW.

A.3 Cathodoluminescence Spectra

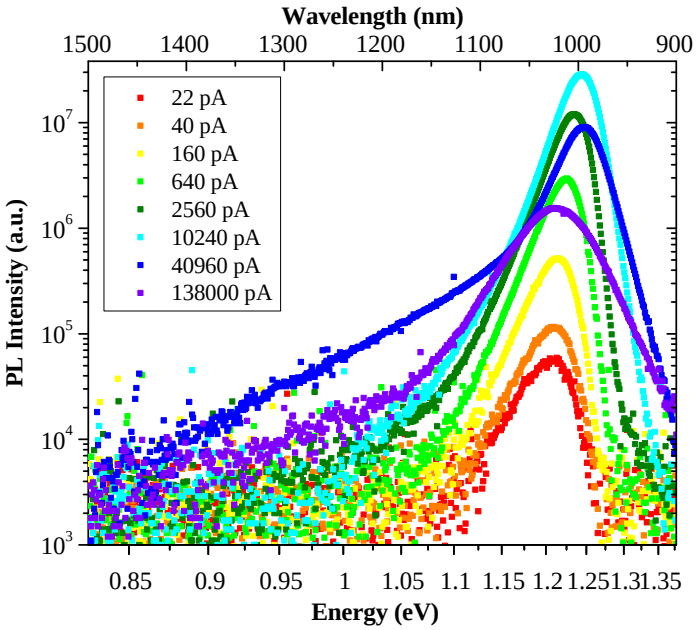

Figure A.15. Power-dependent cathodoluminescence spectra for film x = 0 taken at 10 K.

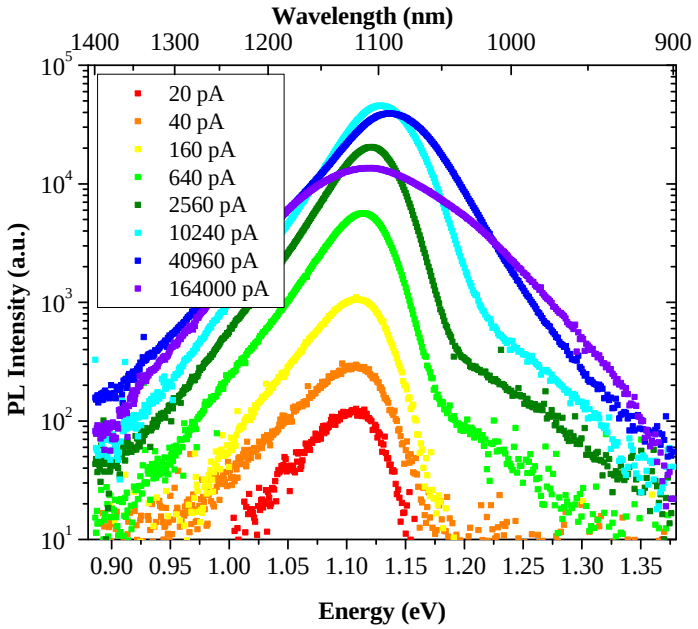

Figure A.16. Power-dependent cathodoluminescence spectra for film x = 0.2 taken at 10 K.

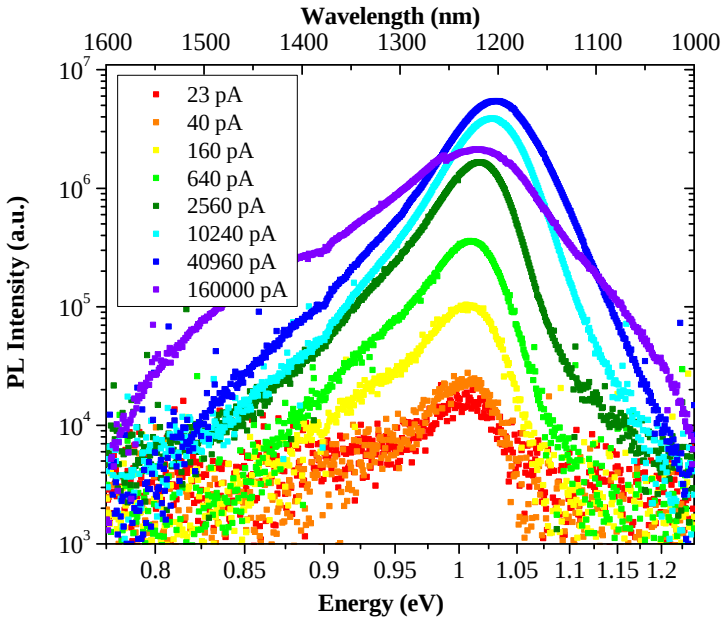

Figure A.17. Power-dependent cathodoluminescence spectra for film x = 0.6 taken at 10 K.

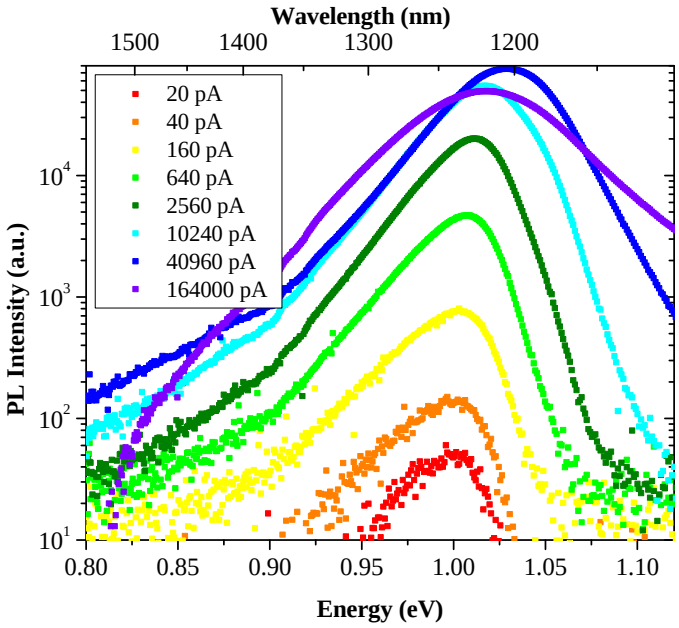

Figure A.18. Power-dependent cathodoluminescence spectra for film x = 0.8 taken at 10 K.

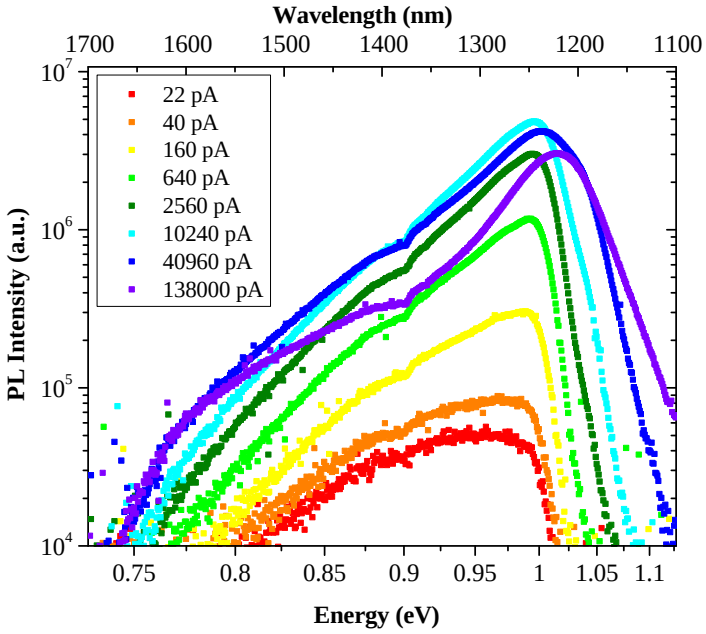

Figure A.19. Power-dependent cathodoluminescence spectra for film $x = 1$ taken at 10 K.